The Effect of Strain Ageing on Plastic Deformation in High Strength Steel

By

Evan Drew

McMaster University

(Hamilton)

August 2017

Abstract

The influence of strain ageing on the mechanical properties, plasticity and fracture of quenched and tempered martensitic 300M steel is investigated. Tensile testing with variable strain rate identified the presence of negative strain rate sensitivity at room temperature. The existence of dynamic strain ageing at room temperature was also confirmed for strain rates between 0.00133-0266 s^{-1} using digital image correlation (DIC). Strain ageing resulted in significant strengthening at room temperature, which masks the presence of dynamic strain ageing upon re-loading. Fracture analysis conducted using scanning electron microscopy (SEM) revealed only minor differences in the failure mechanisms and fracture morphology caused by deformation and ageing. A model by Brown and Embury is used to link inclusion size and distribution to failure strain, and the failure mechanism of 300M was determined to be the formation of micro-voids on transition carbides and inclusion particles. Models for dislocation evolution and locking based on fundamental theories were also produced and successfully used to model the transient strengthening of 300M following ageing at room temperature using differential dislocation evolution equations.

Preface

The bulk of the work presented in this thesis was performed at the Materials Science and Engineering department of McMaster University and the McMaster Automotive Resource Center (MARC). Sample preparation, material heat treatment, and characterization were performed predominantly in the MSE labs, while mechanical testing was accomplished at MARC with the assistance of Dr. Mike Bruhis.

Scanning electron microscopy was performed at the Canadian Center for Electron Microscopy at McMaster University by the author, including fracture analysis, electron dispersive spectroscopy, and inclusion analysis. Electron backscatter diffraction was performed by technician Chris Butcher while the author was present. Subsequent data analysis was performed solely by the author.

All transmission electron microscopy results shown in this work were carried out by Dr. X Wang of McMaster University prior to this work, and the results were interpreted at a later date by the author.

Table of Contents

List of Tables

List of Figures

Acknowledgements

"If I have seen further, it is by standing on the shoulders of giants"

-Sir Isaac Newton

The author gratefully acknowledges the guidance and support of his advisor Dr. H. Zurob, without whom this work would not have been possible.

Additional thanks are due to Dr. J. D. Embury, Dr. O. Bouaziz, and Dr. Y. Brechet for many stimulating discussions and valuable input.

Other individuals deserving of thanks are Dr. M. Bruhis for his assistance with mechanical testing, and Chris Butcher of the CCEM for performing the electron backscatter diffraction.

Thanks are also owed to Dr. R. Panza-Giosa of United Technologies Aerospace Canada for providing the material used in this work.

Chapter 1 - Introduction

Martensitic steels have been the subject of intensive study over the years, due to their incredible properties, including low cost and an exceptionally high strength-to-weight ratio, among others. These properties make martensitic steels ideal for applications that require very high strength, such as aircraft landing gear and structural members in automotive applications.

In spite of the significant body of work performed on martensite, there are still a number of open questions regarding the structure and properties of martensitic steels, and how they are influenced by deformation. This work revisits the work done on martensite using modern tools in an effort to more clearly define the mechanical properties such as strain rate sensitivity at room temperature. A primary goal of this work is also to determine how the mechanical properties and plastic behaviour are influenced by strain ageing. Once these effects are determined, this work aims to describe them in terms of fundamental solute-dislocation interactions and dislocation evolution behaviour.

The material used for this study was 300M steel, a silicon modified variant of AISI 4340 which was supplied by United Technologies Aerospace Canada. The as-received condition of the material was that of tempered martensite, and this was left unchanged in the bulk of the following work.

The first section of this work contains a survey of the wide body of existing literature on ferrous martensite, including its microstructure, properties, and response to plastic deformation. Following the literature survey, a description of the experimental methodology is included, followed by characterization studies of 300M in its as-received condition. A study on the plastic deformation and ageing of martensite is then presented, followed by discussion and interpretation of the experimental results. A series of models based on fundamental aspects of dislocation behaviour are developed, and the effect of strain ageing on the mechanical behaviour and fracture are summarized. Finally, the notable aspects of this work are summarized.

Chapter 2 - Literature Review

The following is a brief survey of the vast body of work which has been performed on ferrous martensite. The focus of this section is on describing the structure and properties of martensite in both the tempered and un-tempered condition. The mechanisms responsible for the deformation and fracture behaviour of martensite are also examined.

2.1 Structure of Ferrous Martensite

2.1.1 Characteristics of As-quenched Martensite

Ferrous martensite is a metastable phase which forms in iron-carbon systems when the material is rapidly cooled from the face centered cubic austensite (γ) phase. Martensite forms upon quenching below the M_s temperature, a composition and stress dependent parameter [1]. The martensitic transformation occurs via a diffusionless displacive transformation resulting in a body-centered-tetragonal crystal structure. The transformation does not proceed to completion however, as some of the parent austenite phase remains after the martensitic transformation has occurred. Due to the diffusionless nature of the transformation, both the retained austensite and martensite phases are identical in composition [2]. The resulting microstructure of martensite is complex and varied on multiple length scales, but can generally be categorized as either lath or plate martensite.

Lath martensite is a hierarchical structure consisting of features on different length scales, namely prior austenite grains, packets, blocks, and laths [3] [4]. The finest unit of this structure is the lath, which has a width of 0.1-0.2μm. Laths are oriented nearly parallel to one another, having a misorientation of less than 3° [3]. Laths are contained within blocks, which have an average misorientation angle of approximately 7° [4]. Morito *et* al also observed that blocks were divided by sub-blocks, which exhibit a misorientation of about 10.5° [3]. Multiple blocks with one of six possible orientations then make up a packet, which is the largest sub-division of a prior austenite grain [3]. A schematic representation of the structure of lath martensite is shown in Figure 1.

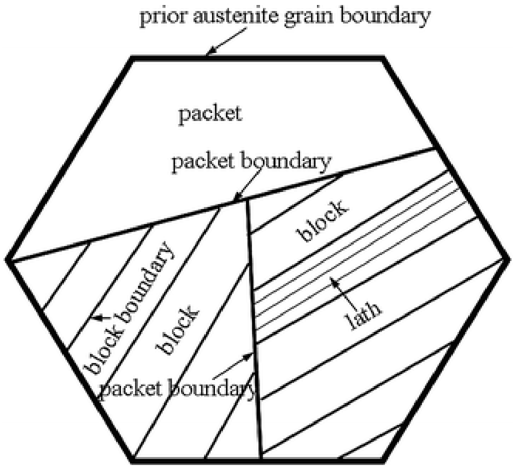

Figure 1: Representation of the structure of lath martensite taken from Du *et al* **[5]**

The structure of plate martensite differs in that it consists of relatively thicker "plates" which are not similar in orientation [6]. The type of martensite which forms in a material is strongly dependent on composition. Both types occur in iron-carbon systems, with lath martensite forming in dilute solutions, while plate martensite dominates at high carbon concentrations. Images of lath and plate martensite taken from Marder and Krauss [6] are shown below in Figure 2.

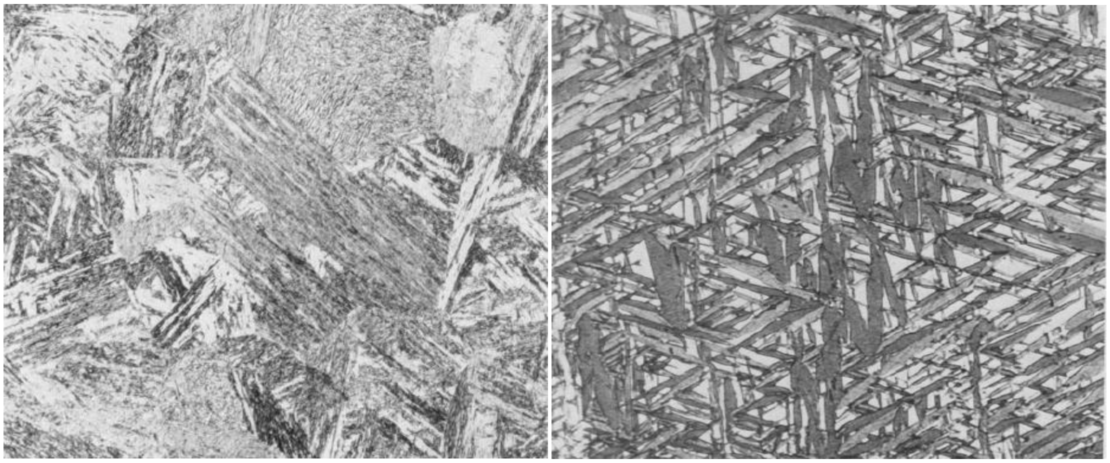

Figure 2: Optical microscope images of lath martensite in 0.2%C steel (left) and plate martensite in an Fe 13.9% Mn alloy (right) taken from Marder and Krauss at 205x magnification and 1000x magnification, respectively

2.1.1.1 Redistribution of Carbon during Quenching of Martensite

The redistribution of carbon atoms during the quenching of martensite was observed as early as 1920's. Rawdon and Epstein noted that significant carbon segregation occurred upon quenching to form martensite [7]. This redistribution occurs in steels with M_s temperatures above room temperature and is known as "auto-tempering". The elastic stress fields of defects such as dislocations and grain boundaries offer favorable interstitial sites for carbon atoms, providing a driving force for the redistribution of carbon during both quenching and subsequent tempering [8] [9]. Morsdorf *et al* determined the expected diffusion distance for carbon atoms which redistribute themselves during quenching as a function of the transformation temperature (M_s) and the cooling rate [10]. They found that the strong auto-tempering occurring in martensite can reduce the matrix carbon content to ~0.15 at% C in certain regions.

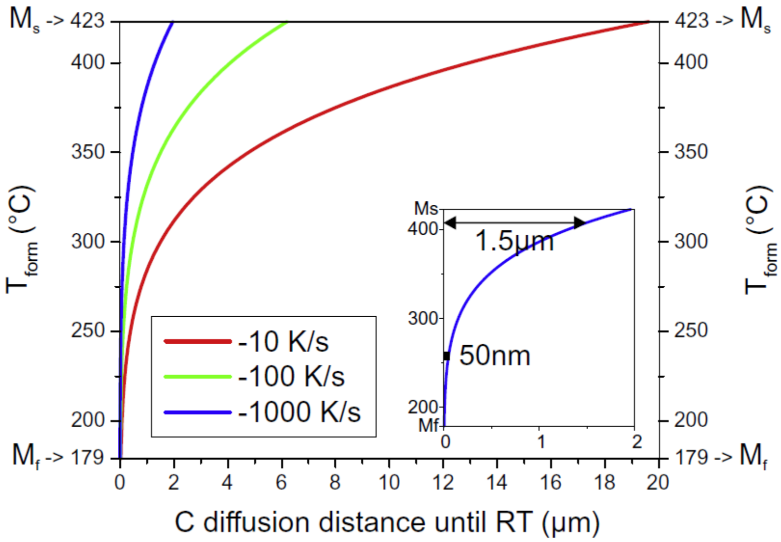

Figure 3: Diffusion distances of C in low carbon martensite for varied cooling rates below M_s **[10]**

Speich studied the redistribution of carbon using electrical resistivity and internal friction measurements, and found strong evidence for segregation to lattice defects [9]. Speich calculated that in steels with carbon contents less than 0.2 wt%, almost 90% of the carbon segregates to lattice defects during the quenching process, whereas for steels with greater than 0.2% C, the defects become saturated and carbons atoms remain in the bulk [9] [11].

Calculations performed by Kalish and Roberts provide a theoretical framework for the measurements obtained by Speich, demonstrating that 85% of interstitial carbon will be segregated to dislocations at equilibrium in steels containing ≤0.2 wt% C [12]. The percentage of interstitial carbon segregated to dislocations decreased to 66% for a 0.8 wt% C martensite whose substructure contained 35% twins [12]. It should be noted however that Kalish and Roberts only considered segregation of carbon to dislocations, and excluded other defects. Their conclusion that the majority of carbon atoms are redistributed to dislocations was correct however, and has since been confirmed by imaging atom probe (IAP) and field ion microscopy (FIM) studies conducted by Chiang *et al* [13].

While the bulk of carbon atoms segregate to dislocations during and after quenching, carbon redistribution to other defects has also been identified. Allain *et al* detected carbon segregation to nanotwins [14], and Hutchinson *et al* discovered segregation to planar defects having a length scale consistent with the lath width in their microstructure [15].

2.1.1.2 Dislocation Populations and Structure

Lath and plate martensites have different structures as well as dislocation populations. The dislocation behaviour of both lath and plate martensite in Fe-Ni-Mn alloys was investigated by Wayman and various co-authors using transmission electron microscopy [16] [17] [18]. Wakasa and Wayman determined that the dislocation densities of lath and untwinned plate martensite were about 4.8 x $10^{14}/m^2$ and 7.2 x $10^{13}/m^2$, respectively, and that screw dislocations made up the bulk of the population [17]. Morito *et al* noted slightly higher dislocation densities in Fe-C alloys, finding a maximum average dislocation density of 3.21 x $10^{15}/m^2$ in as-quenched lath martensite [19]. A recent study by Berecz *et al* [20] reported a dislocation density of 3 x $10^{15}/m^2$ in ferrous lath martensite, supporting the results of Morito and colleagues.

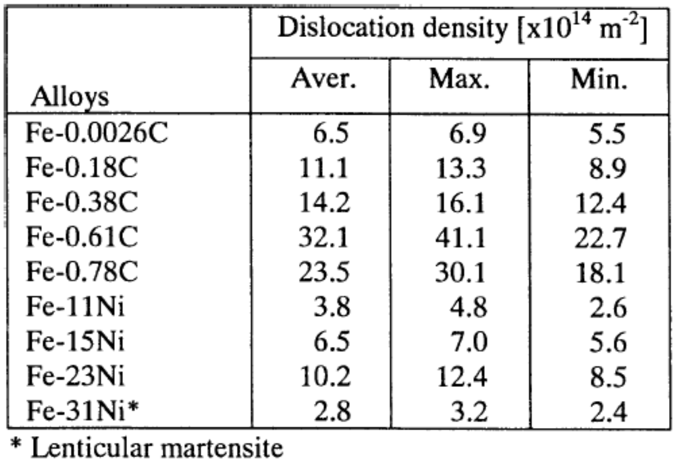

Alloys	Dislocation density [x10^{14} m^{-2}]		
	Aver.	Max.	Min.
Fe-0.0026C	6.5	6.9	5.5
Fe-0.18C	11.1	13.3	8.9
Fe-0.38C	14.2	16.1	12.4
Fe-0.61C	32.1	41.1	22.7
Fe-0.78C	23.5	30.1	18.1
Fe-11Ni	3.8	4.8	2.6
Fe-15Ni	6.5	7.0	5.6
Fe-23Ni	10.2	12.4	8.5
Fe-31Ni*	2.8	3.2	2.4

* Lenticular martensite

Table 1: Observed dislocation densities in Fe-C and Fe-Ni lath martensites as calculated by Morito *et al*

Morito and colleagues attributed the higher dislocation density in lath martensite to the plastic accommodation of transformation strain in the martensite, and also noted a slight concurrent increase in dislocation density with increasing solute content [19].

2.1.2 Tempering of Ferrous Martensite

This work distinguishes between the terms *ageing* and *tempering* using the classical terminology which describes ageing as any process occurring below 100°C and tempering as processes which take place above 100°C. This arbitrary distinction separates the region dominated by the diffusion of carbon, which occurs at and below 100°C from the region in which the formation of carbides takes place.

Ageing and tempering are known to significantly influence the microstructure and properties of as-quenched ferrous martensite. Winchell and Cohen first examined the ageing process in as-quenched martensite, and discovered increases in hardness and electrical resistivity after ageing between -60°C and 100°C [21]. Efforts to understand the exact nature of the changes in structure have not been conclusive, but have positively confirmed that a notable fraction of carbon segregates during low temperature ageing [22]. Nagakura *et al* identified the formation of carbon atom clusters, followed by the development of a modulated structure with enriched regions containing up to 10-16 at% carbon [23]. Studies conducted using differential scanning calorimetry [24] and Mössbauer spectroscopy [25] imply that carbon diffusion is the controlling process for the formation of such a modulated structure. This conclusion was reached by comparing the measured activation energy of the aforementioned processes to the activation energy for carbon diffusion in ferrite [23] [25].

Atom probe studies of as-quenched and tempered martensite conducted by Badinier [22], Danoix [26], and others illustrate the segregation of carbon which takes place as martensite is tempered.

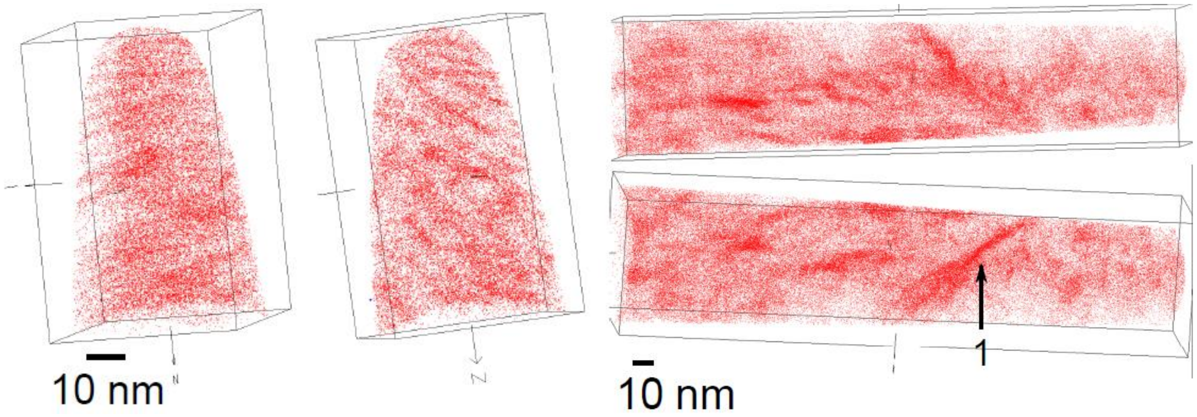

Figure 4: 3D atom probe images of as-quenched martensite (left) and martensite tempered at 120°C for 8 hours (right) taken from Badinier **[22]**

2.1.2.1 Stages of Tempering

As mentioned previously, the segregation of carbon occurs in martensite as it is aged and tempered. A number of additional transformations occur during the tempering process as shown below.

The first process that occurs during the tempering of ferrous martensite is the precipitation of transition carbides. The exact nature of these carbides has been a matter of some debate, and their structure has not yet been positively identified. Jack [27] described what he called ε-carbide, with a stoichiometry of $Fe_{2.4}C$ and a hexagonal close-packed structure, while Hirotsu and Nagakura [28] identified an orthorhombic structure with a stoichiometry of Fe_2C that they named η-carbide. More recent work using 3D atom probe analysis, however, casts some doubt on these stoichiometries due to a continuous increase in local carbon concentration after ageing at room temperature for up to 1000hrs [29]. As such, the composition and structure of these transition carbides is still unknown.

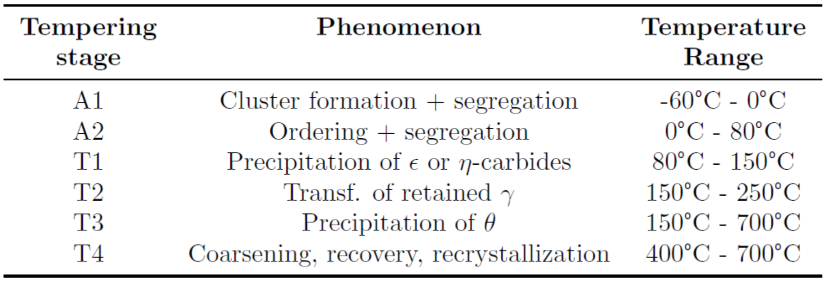

Tempering stage	Phenomenon	Temperature Range
A1	Cluster formation + segregation	-60°C - 0°C
A2	Ordering + segregation	0°C - 80°C
T1	Precipitation of ϵ or η-carbides	80°C - 150°C
T2	Transf. of retained γ	150°C - 250°C
T3	Precipitation of θ	150°C - 700°C
T4	Coarsening, recovery, recrystallization	400°C - 700°C

Table 2: Ageing and tempering processes occurring in ferrous martensites originally published by Leslie and Sober **[30]** and taken from Badinier **[22]**

The second process occurring during the tempering of martensite is the decomposition of the retained austensite phase. As noted earlier, the martensitic transformation only rarely proceeds to completion, leaving some of the parent austenite in the microstructure. Tempering the as-quenched microstructure at a composition-dependent elevated temperature then causes the austenite to decompose into ferrite and cementite phases [31].

After the decomposition of retained austenite, the final precipitation step occurs, wherein the small transition carbides become orthorhombic cementite (Fe_3C). Cementite initially forms as a rod-shaped precipitate in martensite, but tends to spheroidize as the tempering temperature increases [32].

2.1.2.2 Heat Treatment and Tempering of AISI 4340 and 300M Steels

High strength steels have been the subject of intensive study in the field of materials science due to their useful combination of properties. Two such steels are AISI 4340 and 300M, a silicon-modified variant of the former steel. Both steels have been investigated thoroughly in order to maximize their considerable strength and to quantify the so called "temper embrittlement" associated with them in certain tempering ranges.

The effect of austenitizing temperature on 4340 steel was investigated by Lai *et al*, and it was determined that austenitizing at temperatures above 870°C resulted in the formation of relatively thick interlath films of retained austenite when compared to lower austenitizing temperatures [33]. These austenite films did not affect the yield strength but increased the fracture toughness in the as-quenched condition. Toughness testing performed by Datta, however, determined that under blunt notch testing conditions, the toughness of the lower austenitizing temperature was superior due to the influence of prior austenite grain size [34]. Datta also identified the formation of transition ε-carbides as being responsible for a significant increase in toughness [34]. As mentioned above, transition carbide formation occurs in the early stages of tempering [35] at temperatures up to approximately 200°C in 4340 steels [36] [37]. At temperatures exceeding this value, interlath austenite decomposes into cementite and ferrite, which is one of the processes responsible for tempered martensite embrittlement. The effect of tempering on precipitate formation and retained austenite fraction was also investigated by Balestrino and Cavallini using Mössbauer spectroscopy [37]. They determined that tempering 4340 for 2 hours at 200°C resulted in a retained austenite content of 5%, while increasing the temperature to 300°C eliminated all retained austenite and resulted in the precipitation of cementite.

The composition of 300M steel is almost identical to that of AISI 4340, with the exception of much higher silicon content. This additional silicon has a significant effect on the retained austenite content of the material, as noted by Vajda *et al* [38]. Their study of 4340 steel with 1-1.5 wt% Si revealed that the amount of retained austenite in the quenched material increased significantly with increasing silicon content, particularly as the cooling rate decreased [38]. The authors also noted an initial rapid increase in hardenability which decreased as additional silicon was added. Both the increased hardenability and retained austenite fraction were noted by Shih *et al*, who studied 4340 and 4325 steel containing 1.5% silicon by weight [39]. In addition to the above effects, silicon also significantly increases the temperature at which transition carbides dissolve and cementite precipitates develop to 425°C [40]. This phenomenon is commonly attributed to the low solubility of silicon in cementite, which requires the silicon to be rejected before cementite can precipitate. Horn and Ritchie also studied the effect of tempering on the retained austenite fraction in 300M after quenching from an austenitizing temperature of 870°C as shown below [40]. It should be noted however that the steel examined by Horn and Ritchie contained only 1.3 wt% silicon.

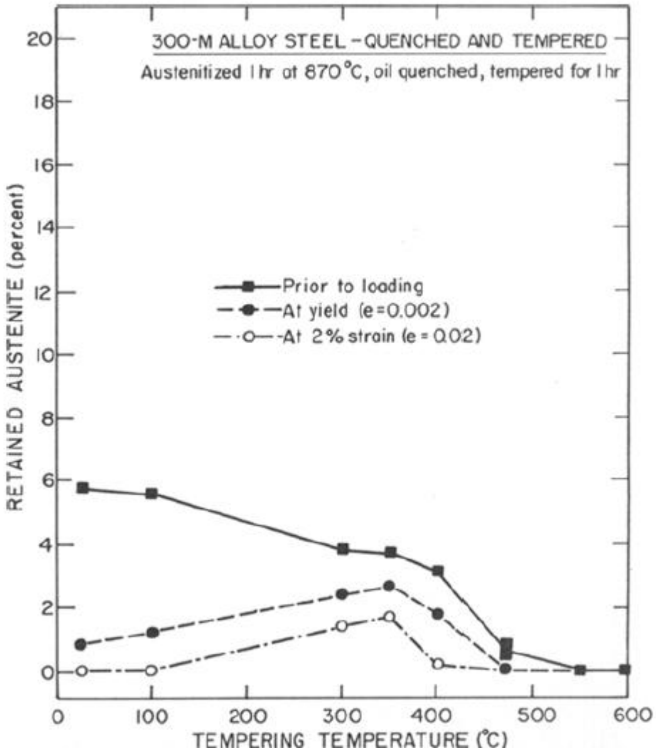

Figure 5: Retained austenite fraction in 300M steel after tempering and deforming taken from Horn and Ritchie **[40]**

In 300M steels, the presence of ε-carbide was detected when tempering between 200-425°C by Youngblood and Raghavan [41]. This result has recently been supported by the work of Liu *et al*, who also noted that the ε-carbide was transformed to cementite upon tempering above 350°C [42]. Padmanabhan and Wood investigated the austenitizing and tempering cycles of 300M, highlighted the significance of the structure of martensite and determined that cyclic heat treating increased the strength of 300M by refining the lath width and prior austensite grain size [43]. The authors also discovered that including an intermediate heat treatment (holding at 650°C for one hour) after quenching and before tempering improved strength as well as ductility and fracture toughness [43]. The improved properties were said to be due to the refinement of the prior austensite grain size and substructure [43].

2.1.2.3 Temper Embrittlement of Martensite

While tempering is commonly performed in order to increase the ductility of martensitic steels, not all tempering treatments are beneficial to the mechanical properties of martensite. As such, tempering treatments must be selected with care. Temper martensite embrittlement (TME) is a well established phenomenon that occurs in ferrous martensite, and results in a decrease in fracture toughness in previously ductile tempered martensitic steel. A number of studies were performed on AISI 4340 and 300M steels in order to determine the mechanisms responsible for the embrittling behaviour. Krauss [44] illustrated the dependence of embrittlement on both tempering temperature and carbon content, shown below in Figure 6.

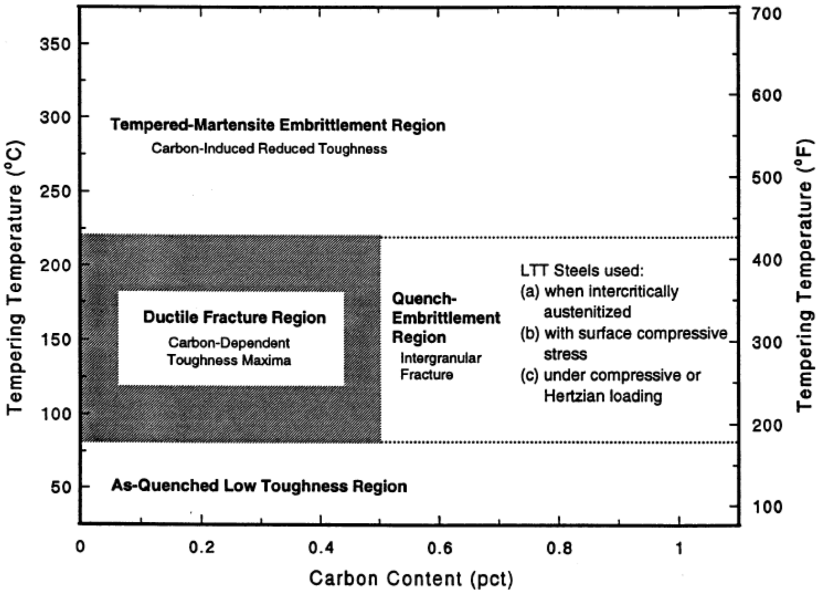

Figure 6: Fracture mechanism diagram for martensitic steels, dependent on wt% C and tempering temperature as proposed by Krauss **[44]**

An investigation by Horn and Ritchie observed that the decrease in fracture toughness was due to the replacement of ε-carbide with interlath cementite and the mechanical instability of interlath retained austenite [40]. Horn and Ritchie also examined the effect of silicon on 4340 and found that while silicon promoted the segregation of impurities to grain boundaries, it also increased the temperature required to initiate embrittlement due to the low solubility of silicon in cementite.

Krauss and Materkowski later concluded that the mechanism of brittle failure associated with the mechanism responsible for embrittlement was the simultaneous formation of grain boundary carbides and impurity segregation [36]. McMahon and Banyopadhyay [45] agreed with the mechanism proposed by Krauss and Materkowski, but concluded that the transformation of retained austenite was not a significant cause of TME as proposed by Horn and Ritchie, but merely an accompanying process after a more rigorous investigation.

2.2 Mechanical Properties of Martensite

Martensite is a complex phase with a number of properties that made it ideal for a large number of engineering applications [46]. High strength and hardness in particular are desirable properties, which are due to a number of microstructural and compositional features.

2.2.1 Strengthening Mechanisms

As mentioned above, martensite is known for its very high strength, particularly in the as-quenched state. Leslie and Sober [30] examined ferritic and martensitic steels of varying composition and determined the relative contributions to their respective strengths as shown below.

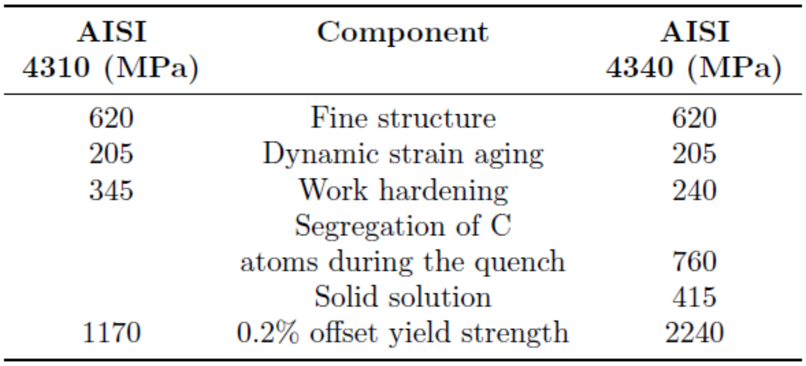

AISI 4310 (MPa)	Component	AISI 4340 (MPa)
620	Fine structure	620
205	Dynamic strain aging	205
345	Work hardening	240
	Segregation of C atoms during the quench	760
	Solid solution	415
1170	0.2% offset yield strength	2240

Table 3: Strengthening mechanisms for 0.1wt%C AISI 4310 and 0.4wt% AISI 4340 as-quenched lath martensites as originally recorded by Leslie and Sober and recently published by Badinier

Notably, Leslie and Sober determined that the fine structure was the dominant strength factor for low carbon martensites (C< 0.15 wt%), while in medium and high carbon martensites (C> 0.3wt%) the rearrangement of carbon and dislocations was the dominant factor [30].

2.2.1.1 Structure and Substructure Strengthening

As mentioned above, the microstructure of martensite is varied and complex. This complex structure is responsible for many of the observed properties of martensite, on both the macro and micro scales. The structure of a material contributes significantly to its strength, and Christian suggested a Hall-Petch effect due to lath boundaries for martensite [47]. He also noted that the martensite lath size is dependent on both the amount of carbon and the prior austenite grain size in a material [47].

Although it is difficult to isolate the contribution of microstructure to the strength of martensite, several authors have managed to assess its influence by creating carbon free martensite. Vyhnal and Radcliffe used heat treating and hydrostatic pressure to produce a lath martensite free of carbon and determined that if the material was subsequently annealed under atmospheric pressure, it became softer [48]. While no explanation for this behaviour was given, Kang *et al* recently confirmed that the refined lath structure due to high-pressure treatment was responsible for the higher hardness [49]. Kang *et al* [49] measured a hardness of 218 HV, compared to the value of approximately 200 HV measured by Vynhal and Radcliffe [48]. If these hardness values are examined using the equivalent 0.2% offset stress calibration curve developed by Speich and Warlimont [50], values of 500MPa and 430MPa are obtained [51]. These measurements show good agreement with the data of both Chilton and Kelly [52] and Speich and Warlimont [50] if their respective values are extrapolated to zero carbon, as shown in Figure 7.

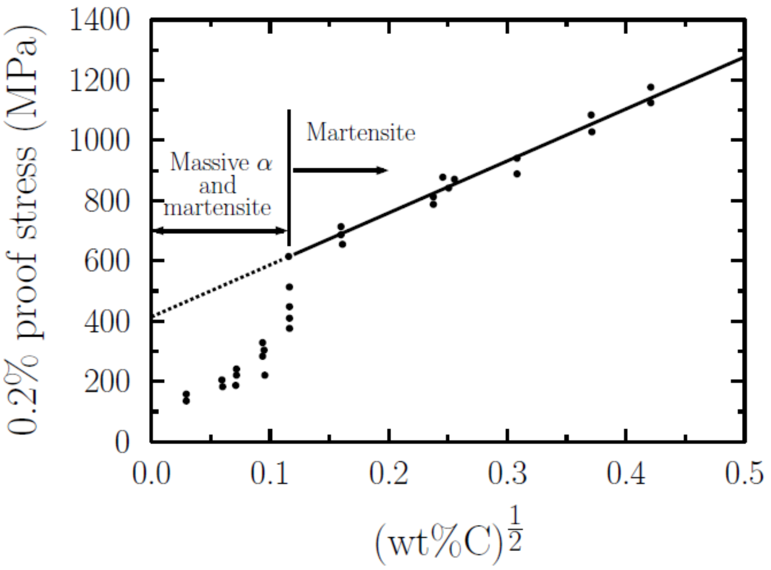

Figure 7: 0.2% offset yield stress data for as-quenched low carbon lath martensites. Data originally published by Speich and Warlimont **[50]** and recently reproduced by Badinier *et al* **[51]**

Leslie and Sober utilized a different method to create a lath structure, as they shock-loaded an interstitial free steel and found its hardness to be 230 HV [30]. While this value is very similar to the hardness measurements of Vynhal and Radcliffe [48] and Kang *et al* [49], the 0.2% offset yield stress reported by Leslie and Sober was comparatively higher (670MPa) [30]. This result is not entirely unexpected, as Leslie and Sober noted that the higher dislocation density and potentially larger population of twins caused by shock loading would result in an upper limit for the strength of carbon free martensite.

The above results suggest that the fine structure contribution to the 0.2% offset strength of lath martensite is in the range of 500-600 MPa. The work by Chilton and Kelly, however, suggests that the structure of martensite has a negligible contribution to the strength if the carbon content across various microstructures remains the same [52]. This conclusion is reinforced by more recent work done by Shibata *et al*, which concluded that only block boundaries were effective at opposing dislocation motion, while lath boundaries were not [53]. Work by Zhu *et al* reaches an opposing conclusion however, as the authors determined that lath boundaries and dislocation cell boundaries are equally effective dislocation barriers [54].

As such, while a relative measurement of the structural contribution to strength can seemingly be made, the mechanisms which govern this contribution are still not fully understood.

2.2.1.2 Dynamic Strain Aging

Dynamic strain aging, also known as the Portevin-Le Chatelier effect, jerky flow, or serrated flow is a phenomenon that occurs in steels and involves solute-dislocation interactions as described by Cottrell [55] [56]. In this regard, dynamic strain aging (DSA) is similar to static strain aging, which is responsible for Luders instabilities [57]. Both DSA and Luders instabilities are due to propagating deformation bands, but only DSA instabilities are repetitive [57].

The importance of dynamic effects with respect to the flow stress was highlighted by Leslie and Sober, who observed a transition from negative strain rate sensitivity at room temperature to a positive sensitivity above a certain critical strain rate [30]. The contribution of dynamic ageing observed by Leslie and Sober offers a significant contribution (205MPa) to the strength of as-quenched martensite as shown in Table 3. Indeed, Tanaka and Spretnak concluded that the flow stress increment (total stress minus the yield stress) in AISI 4340 steels was dominated by contributions from dispersion hardening and dynamic aging, with the latter being linearly proportional to the amount of carbon in solution [58].

Dynamic strain aging is associated with negative strain rate sensitivity [59], and is strongly dependent on temperature and the strain rate. Mulford and Kocks illustrated the strain-rate and temperature dependence of serrated flow by testing Inconel 600 at different strain rates and temperatures, and this dependence is shown in Figure 8 [56]. In their work, they observed dynamic strain ageing at temperatures greater than 100°C.

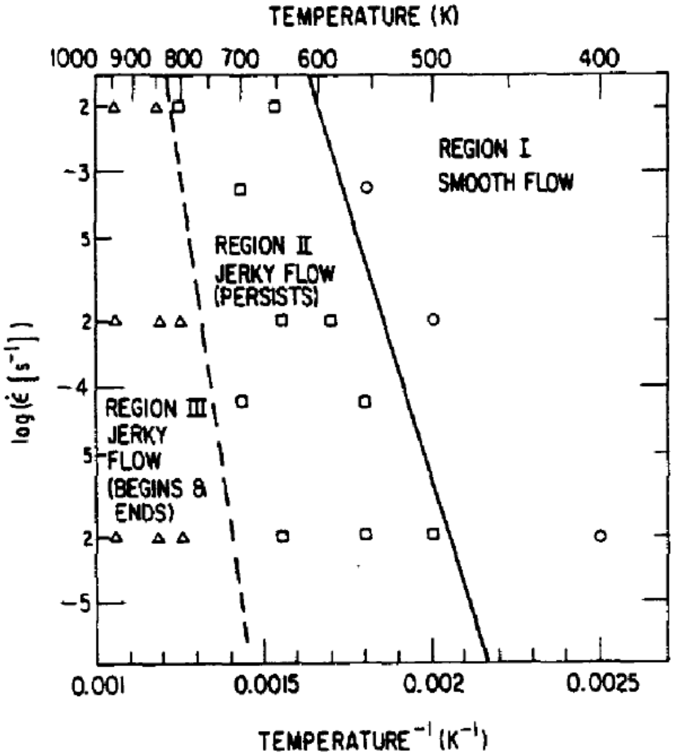

Figure 8: Temperature and strain rate dependence diagram for FCC Inconel 600 taken from Mulford and Kocks

The results of Mulford and Kocks are in good agreement with those of Owen and Roberts, who determined that serrated flow was dependent on the strain rate and testing temperature, and that the activation energy for the process was similar to that of carbon diffusion in ferrite [60] [61]. Both sets of authors demonstrated that increasing the testing temperature promotes serrated flow if the strain rate is held constant. The influence of carbon on dynamic strain aging was observed by Allain *et al*, who reported that dynamic aging was present at room temperature in virgin 0.4 wt% C plate martensite, and that the effect vanished after room temperature aging [14].

Mimura and Aoki determined that the flow stress in martensite was sensitive to the strain rate due to solute atoms and the Snoek effect [62]. Mimura and Aoki also observed that there was a region of strain rate where the stress was insensitive to strain rate, and that the effect disappeared if the martensite was aged between 100-250°C [62].

Owen and Roberts distinguished between two types of unstable flow in iron-carbon alloys: jerky flow, which occurs as a result of the Snoek interaction, and serrated flow, said to be the result of Cottrell drag of carbon and nitrogen atoms [60]. They also concluded that only serrated flow occurs in martensitic structures and that the serrated yielding or flow starts and ends at higher temperatures and strain rates in martensite than those required for ferrite at an identical carbon concentration [60]. These different conclusions were drawn based on the fact that Owen and Roberts consider a significant internal friction peak observed in martensite to be due to Cottrell drag.

Rodriquez [63] and others identified and described several distinct types of serrated flow based on observations during tensile testing, shown below in Figure 9. Each type is not necessarily mutually exclusive, since certain types of serrations were observed to interact with one another. The presence of serrations is due to the formation of localized bands of plastic flow that propagate throughout the material. Indeed, the specific type of serrated flow can often be identified using the propagation behaviour of the deformation bands. It is somewhat unclear, however, if changes in the deformation bands are due to the evolution of certain band types, the interaction of multiple types, or both.

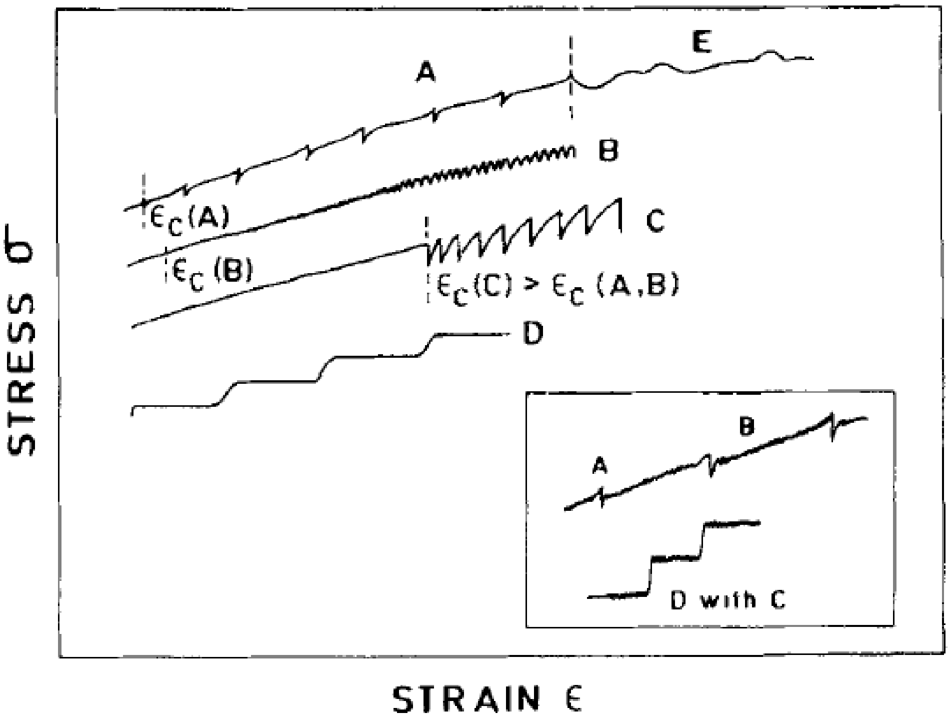

Figure 9: Types of serrated flow occurring in low carbon steels during tensile testing **[63]**

2.2.1.3 Solid Solution Strengthening

Alloying elements are frequently added to steels in order to modify both thermal and mechanical properties. Elements such as silicon, nickel, and manganese exist in solid solution and provide an increase in strength proportional to the amount of solute present in solution due to lattice strains restricting the motion of dislocations [64]. The bulk of studies done on solid solution strengthening in martensitic steels focus on carbon due to its strong effect on the strength and properties of martensite. Krauss proposed the following relationship which demonstrates that the yield strength is proportional to the square root of the carbon content in the material [46].

$$\sigma_{0.2}(MPa) = 413 + 1.72 * 10^3 (wt\%C)^{0.5} \qquad [1]$$

In addition to carbon, silicon and manganese have also been shown to notably increase the hardness of martensite. Shih *et al* found that martensite could be hardened by up to 140 MPa through the addition of 1.5 wt% Si [39]. Krauss also determined that the addition of 4-6 wt% Mn could harden steels by 200 MPa, but the strengthening came at the cost of decreasing the dislocation density [46]. The effect of nickel as a solid solution strengthener is less certain, with conflicting reports about its contribution [65] [66]. Additionally, it has been claimed that nickel reduces dislocation pinning, while silicon, chromium, and molybdenum inhibit cross-slip [67].

2.2.1.4 Precipitation Strengthening

An alloy undergoes precipitation strengthening if tempering or heat treatment in a given range produces increases in mechanical properties such as hardness or yield strength.

This topic has been reviewed by a number of authors and is generally well understood in most systems [68]. The transition carbides in tempered martensite, however, have not been studied in detail, and it is unknown whether or not the precipitates are shearable due to a lack of detailed study [51].

Malik and Lund endeavored to explain the evolution of the 0.2% offset stress in a 0.42 wt% C steel by examining the precipitation of cementite and the dislocation densities after tempering at various temperatures [69]. The authors used a modified Orowan equation to measure the contribution of carbides to strengthening and x-ray diffraction to track the dislocation density in the material. Using these methods, Malik and Lund determined that the 0.2% offset stress was directly linked to the carbide spacing and dislocation density. They also concluded that the evolution of the 0.2% offset stress could be explained by the above factors without including a structural contribution.

2.2.1.5 Carbon Segregation to Defects

The segregation of carbon atoms to dislocations was first examined and modeled by Cottrell and Bilby [70]. They demonstrated that a substitutional atom in solid solution could relieve hydrostatic stress based on its interaction energy relationship with a positive edge dislocation by building on initial work by Cottrell [55]. Cottrell and Bilby described the segregation of a carbon atom to a positive edge dislocation as shown in Equation 2 for short time ageing.

$$f = 3(\frac{\pi}{2})^{1/2}\rho(\frac{ADt}{kT})^{2/3} \qquad [2]$$

In their segregation equation, Cottrell and Bilby used f to denote the fraction of interstitial atoms segregated, ρ for the edge dislocation density, D to represent the diffusion coefficient of carbon, t to indicate time, T for temperature, k for the Boltzmann constant, and A for a parameter which describes the interaction energy between an interstitial atom and a dislocation. While Cottrell and Bilby only considered interactions with edge dislocations, Cochardt *et al* expanded their locking theory to include effects from screw dislocations and impurity atoms [71].

Experimental work supports the theory of carbon segregation to dislocations proposed by Cottrell and Bilby. Speich observed significant segregation to defects following both quenching and tempering [11], and more recent atom probe measurements support these conclusions [72] [73]. Wilde *et al* determined that essentially all carbon atoms were present in Cottrell atmospheres in iron samples containing between 0.45-0.85 at% C, and that the maximum carbon concentration at an atmosphere was approximately 8 at% [73].

Olson and Cohen suggest, however, that carbon clustering is more important than carbon segregation until late in the aging process, even though both effects can occur simultaneously [74]. A diagram for the formation of carbon clusters was created by Sherman *et al* using resistivity measurements and can be seen in Figure 10.

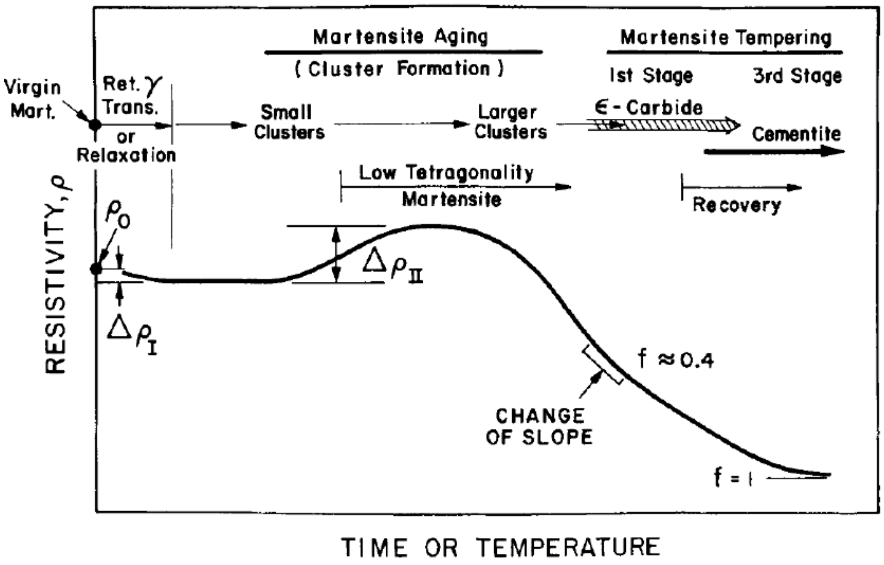

Figure 10: Resistivity curve taken from Sherman *et al* which interprets the changes occurring during the tempering of as-quenched martensite **[75]**

Experiments performed by Cheng *et al* support the conclusion of Olson and Cohen, as they determined that 0.21 at% C was segregated to defects by observing the decrease in unit cell volume for high carbon martensites [76]. Cheng and others also observed that aging at room temperature for 2 years led to coarsening of the carbon clusters, which aggregated with iron [76]. While both phenomena appear to occur concurrently, Olson and Cohen noted that the mechanisms governing the interaction (if any) between clustering and segregation are not well understood [74].

2.2.2 Effect of Alloying Elements on the Structure and Properties of 300M

2.2.2.1 Effect of Alloying Elements on Structure and Properties

Magee and Davies and Sherman *et al* examined various lath, plate, and mixed structures in iron-nickel-carbon martensites and determined that increasing the nickel and carbon contents of steel promoted the formation of plate martensite over a lath structure [77] [75]. The work of Sherman *et al* in particular highlights the importance of composition with respect to the structure of martensite, since the structure cannot be controlled by the quenching treatment alone.

Silicon is another major alloying element in 300M, and it has a number of influences on the mechanical properties of martensite, which have been studied by a number of authors [39] [38] [41] [78]. The effects of silicon on the properties of martensite are relatively well understood, in marked contrast to some other alloying elements. The addition of 1.5 wt% Si has been shown by several authors to increase both the yield strength, ultimate tensile strength, and the yield-to-tensile strength ratio without any loss of ductility [39] [38]. It should be noted, however, that these increases in strength are highly dependent on the tempering treatment, as certain tempering ranges yield worse mechanical properties than the case without silicon due in part to the TME phenomenon discussed above.

The addition of silicon does not have an adverse effect on the mechanical properties of martensite at room temperature. Vajda *et al* found that the ductility and toughness of samples with 1 wt% Si added silicon increased when deformed at 100°C, but samples with 1.5 wt% Si and samples tested at 20°C experienced no change in properties [38]. In some tests, the addition of 1.5 wt% Si was actually found to increase the fracture toughness and ductility [38].

Silicon may have an influence on dislocation behaviour, however, as Kim *et al* showed that silicon inhibits the recovery of martensite proportional to the silicon content of 0.5-0.6 wt% C steels [78]. The authors were not able to determine if the effect on recovery was due to silicon, or an indirect effect due to the solid solution hardening it provides. A similar result was reported by Wittig and Frommeyer, who determined that dislocation cross slip was reduced with increasing silicon content [79]. Neither set of authors explained whether this effect was unique to silicon, or simply a by-product of the solid solution strengthening. The effect of silicon on recovery could be explained if silicon indeed reduces cross-slip as mentioned above [67].

2.3 Plastic Deformation of Martensite

2.3.1 Mechanisms of Deformation in Martensite

Magee and Davies studied the deformation of martensite, and found that the mechanism governing the deformation was largely dependent on the structure [77]. They examined lath, plate, and mixed martensites by altering the Ni content of the alloy, and used optical microscopy to observe the deformation of each structure at room temperature. Magee and Davies determined that in low carbon plate martensites, the deformation was due to wavy dislocation slip, but above 0.4 wt% C deformation was entirely due to twinning [77]. They also found that in lath martensite containing less than ~0.6 wt% C, deformation occurred by dislocation slip, while mixed microstructures with more than 0.4 wt% C deformation occurred by wavy slip in the laths but twinning in the lenticular regions [77].

Swarr and Krauss also studied the deformation of martensite at room temperature and after tempering at 400°C for a very short time [80]. Using transmission electron microscopy, they studied the dislocation population, carbides, and lath structure of both tempered and as-quenched martensite [80]. In deformed as-quenched martensite, dislocations were arrayed in cells inside the martensite laths, while after tempering their distribution was much more uniform [80]. This corresponds to the strong dependence of flow stress on packet size observed in as-quenched martensite, which decreased with increasing deformation, and the absence of a packet-size dependence in the case of tempered martensite [80].

2.3.1.1 Yielding Behavior of Martensite

Muir *et al* studied the elastic limit of quenched and low-temperature-tempered steels and found that it was notably lower than the 0.2% offset stress in the material, though it increased proportionally with tempering temperature [81]. They ascertained that this was due to the relaxation of internal stresses brought about by the tempering process. Zaccone and Krauss had a different explanation for the behaviour however, stating that the low elastic limit found in low-alloyed martensitic steels was caused by the stress-induced transformation of retained austenite [82].

A lengthy elasto-plastic transition has been observed in tempered martensite by several authors, who attributed the behaviour to macroscopic residual stresses present in the microstructure after tempering [30] [81] [83]. The presence of residual stresses was observed by Snyder, who noted that the surfaces of large as-quenched martensitic samples were in a state of residual tension, while the core was in compression [84]. Snyder also determined that these residual stresses could be relaxed after tempering between 200°C and 500°C for a period of 1 hour [84]. Stress relaxation was also observed by Taylor *et al*, who found that low temperature tempering (150°C - 200°C) could relax the stresses they found in polished specimens [85].

Allain *et al* also studied the elasto-plastic transition in martensite, and they attribute this behaviour to significant heterogeneity in the microstructure, where microstructural elements yield at widely varying flow stresses [86] [51]. In practice, this theory has been very effective at describing the drawn-out elasto-plastic transition observed in martensite [51].

2.3.1.2 Work Hardening Rate

Several authors have investigated the work hardening of martensite, including Swarr and Krauss [80], and Saeglitz and Krauss [87]. The lengthy elasto-plastic transition observed during testing in this work was also prominent in the data of both authors, and is similar to the results obtained by Leslie and Sober on shock-loaded interstitial-free steel as mentioned previously [30]. Saeglitz and Krauss noted an increase in the work hardening rate (WHR) with increasing carbon content, which they attributed to a larger population of transition carbides in the higher carbon steels [87]. Additionally, the work hardening rate was observed to decrease as tempering temperature and time were increased [87]. The decrease in WHR with increased tempering was attributed to the coarsening of transition carbides, and the contribution due to dynamic strain aging was discussed due to carbon remaining in solid solution after aging at low temperatures [87]. Unfortunately, this potential contribution was not quantified or studied further.

2.3.1.3 Effects of Plastic Constraint

The influence of plastic constraint on the deformation and fracture of metals has been extensively studied in recent years. Roy and Narasimhan noted that the level of constraint can significantly alter ductile fracture processes [88], despite the fact that fracture toughness is frequently considered to be a material parameter. A plot of fracture toughness demonstrating the effect of constraint on fracture is shown below in Figure 11.

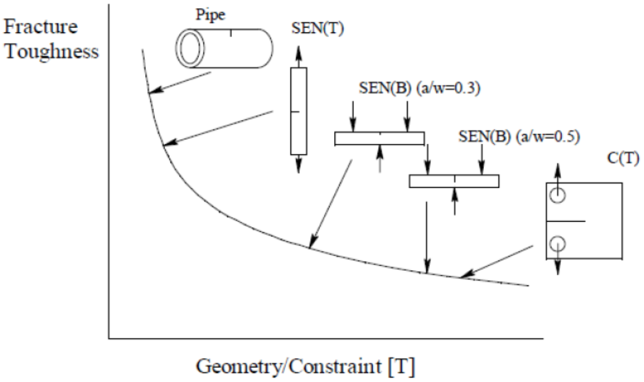

Figure 11: Plot of fracture toughness versus constraint taken from Nyhus *et al*

It is apparent that the geometry used to test a material influences the fracture toughness. Notably however this effect should not be large in ductile materials [89]. Additionally, compact tensile specimens are the most frequently used geometry for fracture testing due to their low cost, so estimates for toughness are frequently conservative [89].

2.3.1.4 Effects of Triaxiality and Hydrostatic Pressure

The effects of hydrostatic pressure on the plastic deformation and fracture of metals have been well-documented in literature. At elevated temperatures (~0.7T/T_m), pressure can also reduce the rate of diffusion by reducing the concentration of vacancies and increasing the required activation energy [90]. These effects are minimal at ambient temperature in most cases, and as such can be neglected. The fracture strain of ductile metals and alloys is more strongly affected by hydrostatic pressure, and increases linearly with pressure in most cases [90].

The influence of sample geometry and the subsequent state of stress have a significant impact on the mechanical properties of a material. For example, stress triaxiality is dependent on the stress state in a material and determines the assumptions that can be made about plastic flow based on the number of dimensions in which flow is unconstrained. The stress state in a material can be altered by varying sample geometry or the applied loading conditions. Triaxiality (η), or triaxial tension is defined as the hydrostatic stress divided by the equivalent stress and void growth models such as the one suggested by Rice and Tracey [91] have found that the rate of void growth is exponentially dependent on the triaxiality [92].

Triaxiality was initially investigated by Bridgeman, who considered the triaxiality which occurs during the necking of round samples [93]. Bai and Wierzbicki later performed tests on various aluminum alloy samples with varied geometries and developed expressions for the stress triaxiality parameter η for each [92]. Bao and Wierzbicki then expanded on this work by creating an equivalent failure strain versus stress triaxiality using various types of loading and sample geometry as shown in Figure 12 [94].

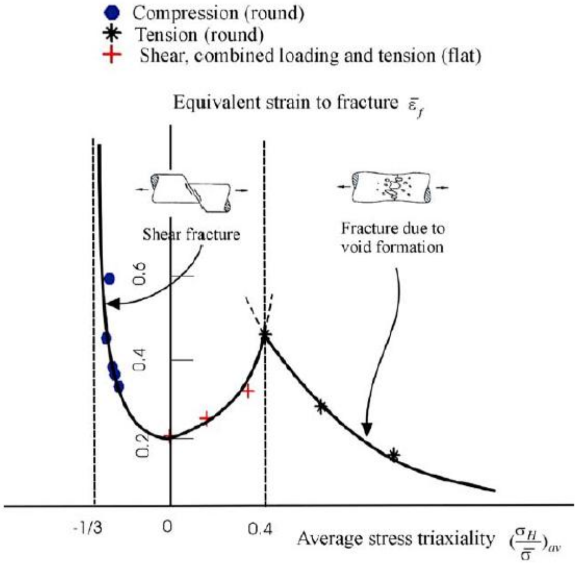

Figure 12: Equivalent failure strain versus average stress triaxiality diagram for aluminum 2024-T351 created by Bao and Wierzbicki

It should be noted that this diagram is unique to the specific aluminum alloy since the fracture locus is highly dependent on material properties, but a similar diagram can be created for other ductile materials using the same process as Bao and Wierzbicki. Increasing stress triaxiality can be seen to decrease the fracture strain in notched or necked samples due to plastic constraint, but increased triaxiality does not reduce ductility. Instead, low values of stress triaxiality have been shown to increase ductile fracture in aluminum alloys [94]. This work helps to highlight the importance of considering effects such as plastic constraint and the state of stress on the final failure of materials.

2.3.2 Effect of Plastic Deformation on Microstructure

2.3.2.1 Effect of Plastic Deformation on Precipitates

The effect of plastic deformation on carbides and precipitation in steel has been studied by numerous authors [95] [96] [97]. Wilson found that by plastically deforming and tempering as-quenched martensite, the precipitation of ε-carbide was inhibited and the first stage of tempering described above was bypassed [95]. Additionally, Wilson found that if martensite was tempered to precipitate ε-carbide and subsequently deformed, the transition carbides were dissolved [95]. This phenomenon was elegantly demonstrated by Cohen, who tempered and then indented martensite to find that all the carbides in a 0.45 wt% C were dissolved upon re-tempering [96]. Wilson and Cohen cited the strong interaction energy between a carbon atom and a dislocation as described by Cottrell as the reason for this behaviour. Kalish and Cohen further investigated the strain tempering of martensite, and found that ε-carbides were dissolved after deformation and re-tempering of tempered martensite [97].

2.3.2.2 Effect of Plastic Deformation on Retained Austenite

Plastic deformation has been shown by Horn and Ritchie to decompose retained austensite in aircraft quality 300-M steel [40]. They argued that the presence of mechanically unstable austenite was detrimental to the mechanical properties since the transformation product is untempered martensite. The mechanical stability of austenite was also investigated by Sastry *et al*, who found that the fraction of retained austenite in AISI 4340 was unstable and decreased with increasing deformation, regardless of the mode of loading or deformation [98].

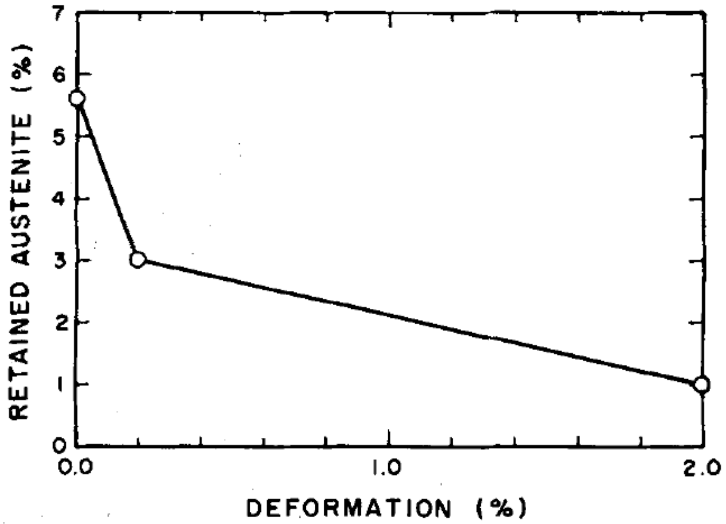

Figure 13: Retained austenite fraction in quenched and tempered AISI 4340 as a function of deformation, taken from Sastry *et al*

While it is agreed that the retained austenite in martensitic steels is mechanically unstable, the effects of retained austenite and its transformation product on mechanical properties are unclear as authors have reported both beneficial [33] and detrimental effects [40].

2.3.3 Strain Ageing of Martensite

Strain ageing is the process of deforming a material and holding under fixed conditions such as temperature and applied load. The strain ageing of martensitic steels has been investigated by numerous authors, with fairly consistent results. Many studies reported that strain ageing of low alloy steels such as AISI 4340 resulted in an increase in yield strength, tensile strength and yield to tensile ratio without a significant loss of ductility, as evidenced by only minor decreases in failure strain [99] [100] [67] [101] [102]. Stress-strain curves for strain-aged steels are shown in Figure 14 [103].

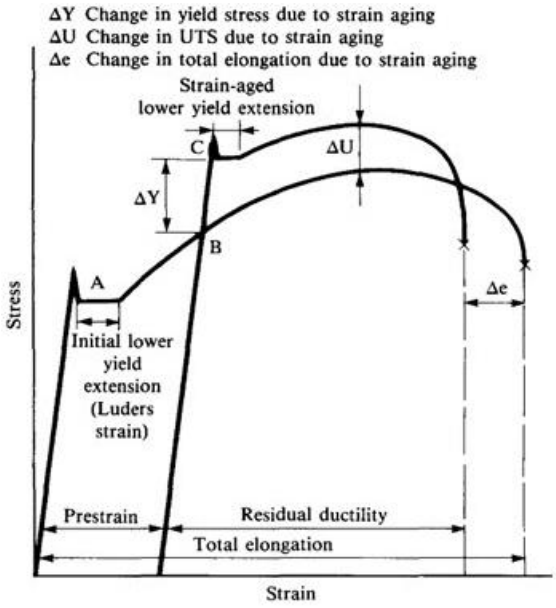

Figure 14: Stress strain curves for strain aged steel

2.3.3.1 Mechanism of Strain Ageing

In all studied cases, deformation followed by holding at room temperature or “strain ageing” was observed to increase the yield strength of the material upon re-loading in the same direction as the pre-strain. The mechanism(s) for this behaviour are a matter of some debate.

Two major mechanisms are responsible for the increase in yield stress which occurs in strain-aged steels the first being the stress induced ordering of solute atoms known as Snoek ordering, and the second being the formation of dislocation atmospheres described by Cottrell and Bilby [70]. Wilson and Russell postulated that the initial increase in yield strength which occurs after strain ageing was due to the local ordering of solute atoms, or so-called Snoek ordering [100]. This was due to the fact that the yield increase occurred too rapidly to be diffusion based, and also that the magnitude of the increase was proportional to the amount of carbon in solution [100]. Additionally, the rate of the initial increase was found to be proportional to the time required for a single atomic jump by a carbon atom [100]. Imanaka and Fujimoto agreed with the mechanisms proposed by Wilson and Russell, but argued that the initial increase in yield stress due to Snoek ordering was proportional to $t^{1/3}$, not $t^{2/3}$ as originally proposed [104]. It should be noted that the ageing experiments performed by Imanaka and Fujimoto were conducted while the material was under load, while Wilson and Russell conducted both loaded and unloaded ageing experiments [104]. Thus, it is possible that both sets of authors are correct, and that ageing under load is responsible for the differences in observed yield stress behaviour. This follows from the conclusion of Wilson and Russell that the increase in yield stress was larger if samples were held under load during ageing [100]. Wilson and Russell also attributed a portion of the rapid increase in yield strength for unloaded samples to be due to the rearrangement of dislocations upon unloading proposed by Haasen and Kelly [105].

The second contribution to the strengthening of steel following ageing is the Cottrell mechanism, namely the segregation of carbon to dislocations discussed in detail in section 2.2.1.5. This mechanism has a larger contribution to the increased yield strength than Snoek ordering, and is generally agreed to have a time dependence of $t^{2/3}$ [100] [104].

Some other authors disagree with the Cottrell mechanism as an explanation for the ageing behaviour however. Elliot *et al* argued that the Cottrell mechanism could not be responsible for the strengthening and absence of a yield point observed after ageing due to the fact that strengthening is not observed if the material is deformed in a direction opposite to the pre-strain direction [106]. Results from their strain reversal testing are shown below in Figure 15.

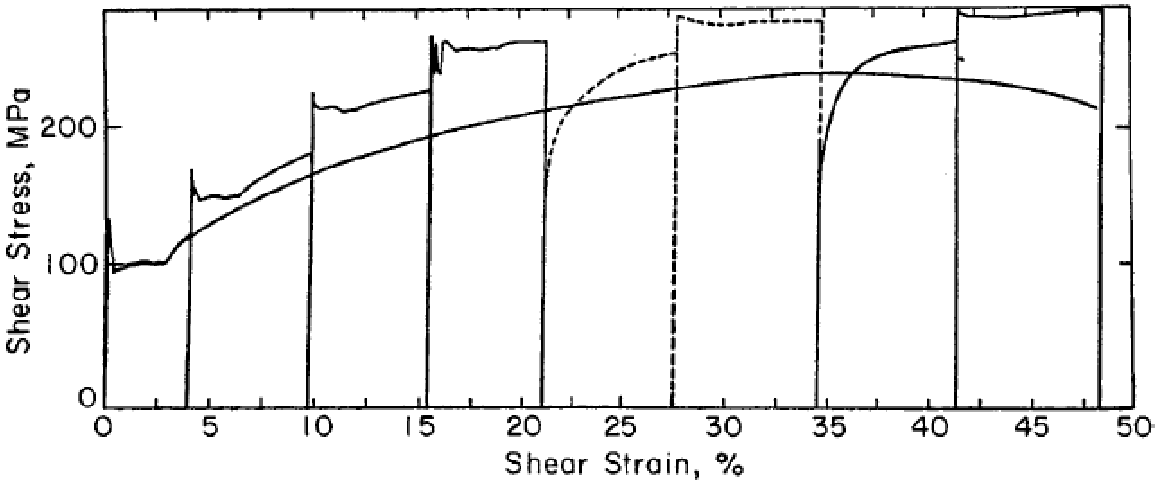

Figure 15: Strain-reversal torsion tests performed by Elliot *et al* that illustrate the differences in mechanical behaviour which are dependent on the direction of pre-strain and subsequent re-loading. Dotted lines represent cases where the direction of strain was opposite to the initial strain **[106]**

In order to explain the lack of an observed yield point during strain-reversal testing, Orowan [106] subscribed to the dislocation multiplication theory proposed by Johnston [107] instead of the dislocation locking model originally proposed by Cottrell and Bilby [70]. Johnston's theory that the yield stress of a material was not based on the state of pinning of dislocations was based on earlier work by Johnston and Gilman which demonstrated that the flow characteristics of LiF crystals were primarily dependent on the dislocation density and mobility in a crystal [108]. Following this work, Johnston demonstrated that a yield point could also be duplicated in the absence of dislocation pinning, and thus the upper yield stress of a material was not unambiguously linked to the stress required to pin dislocations [107].

2.3.4 Fracture of Martensite

The mechanisms governing the fracture of martensite have been rigorously examined in the literature, particularly the cases pertaining to the temper embrittlement phenomenon discussed above.

Studies performed by Krauss have demonstrated that martensite containing less that 0.5 wt% carbon is ductile at room temperature, and if the carbon content is increased the steel experiences intergranular fracture at the prior austenite boundaries [46] [109]. The effect of other alloying elements cannot be discounted, however, as Bandyopadhyay and McMahon demonstrated that silicon and manganese can act as embrittling agents as well as sulfur and phosphorus [45]. While steels with appropriately low carbon content are ductile at ambient temperature, Saeglitz and Krauss reported brittle fracture mechanisms in as-quenched AISI 4340, which they attributed to dynamic strain aging [87]. The authors observed a full restoration of ductile behaviour after tempering, however.

Krauss and Saeglitz [87] also identified the importance of transition carbides in determining the failure mode of 43xx steels. They concluded that tempered specimens almost exclusively failed by micro-void nucleation at precipitates and inclusions [87], a conclusion reached earlier by Zok [90].

2.4 Open Questions Regarding Martensite

While 300M and its parent steel 4340 have been subjected to fairly intense scientific study, the complex structure and properties of the material have thus far resisted complete understanding. The strain rate sensitivity of 300M at room temperature is not clear for example, as prior work has been unable to classify the strain rate sensitivity of its parent material, AISI 4340, at room temperature. Leslie and Sober were able to classify the strain rate sensitivity of steels containing 0.1-0.3 wt% C at room temperature, but were unable to identify a trend in 4340 which contains 0.4 wt% C.

The subject of static strain ageing has also been examined by numerous authors who have studied 4340 or 300M, and while most authors attribute the effects of strain ageing (increased yield strength, tensile strength and decreased ductility) to solute-dislocation interactions [110], little work has been done on modeling the effects of deformation and ageing. A number of aspects of strain ageing also merit further experimental study, including the effects of strain ageing on the strain rate sensitivity and Portevin-Le Chatelier behaviour, which are investigated in this work using digital image correlation (DIC). The influence of strain ageing on the fracture of martensite is also not fully understood. Each of these topics is addressed in this work using experimental observations and modeling, and an effort is made to explain observed behaviour.

Chapter 3 - Experimental Methodology

This section describes the techniques and methods used to prepare, test, and characterize the 300M steel used in this work. The specimen geometries used throughout this thesis are catalogued in section 3.1, and the tensile equipment and methods used to test them are described in section 3.2. Finally, section 3.3 contains information on the scanning electron microscopy and electron backscatter techniques used to characterize and examine failed samples and the as-received condition of 300M.

3.1 Sample Geometries

The specimen geometry used for the bulk of the experiments conducted in this work was that of a smooth round sample. The round sample geometry is shown in Figure 16a. Round notched specimens were also produced in order to determine the effects of the stress state. The notched geometry can also be seen below in Figure 16b.

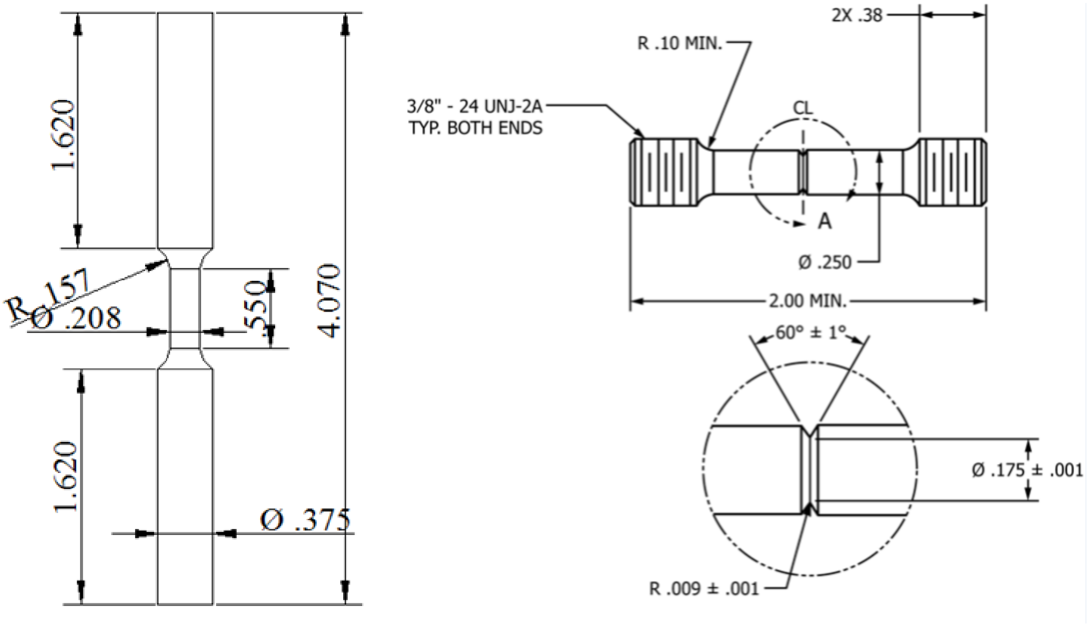

Figure 16a,b: (a) Round sample geometry with measurements denoted in inches (left) and (b) round notched geometry with measurements also displayed in inches (right)

Not all experiments could easily accommodate round geometries however, so flat samples were also produced as shown in Figure 17. The thickness of the samples was 1mm, with the exception of thicker samples produced to examine potential localized plasticity and dynamic effects. For these few samples, the thickness was increased to 3mm in order to aid observation via digital image correlation (DIC).

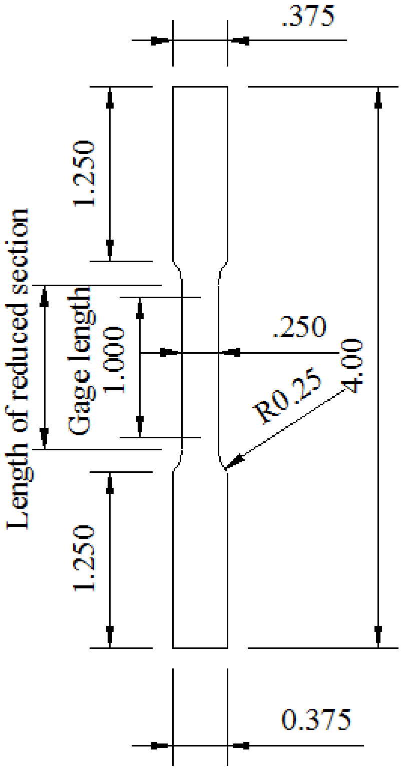

Figure 17: Flat tensile sample dimensions given in inches

3.2 Tensile Testing

The bulk of the mechanical tension testing performed in this work was performed on a 100kN Instron tensile frame with an accompanying extensometer. Samples were loaded to various levels of strain and then unloaded and held for differing amounts of time under varied applied loading conditions and temperatures to investigate aging effects. The deformation rate was also varied in certain cases to examine any potential effects of strain rate on the plastic behaviour of 300M. Since the as-received material was available in batches of 4 which corresponded to a unique heat, specimens were tested and compared within one batch wherever possible. One sample from each batch was also frequently used as a control, to identify any variability between batches.

Standard round specimens were held in the tensile frame with appropriately sized hydraulic v-grips, while flat grips were utilized for the flat specimen geometries. Due to the threaded nature of the notched specimens, specialized connectors were required in order to allow the tensile specimens to be tested using the hydraulic grips of the tensile frame used for the bulk of the mechanical testing in this work.

3.2.1 Tensile Testing with Digital Image Correlation

Digital image correlation (DIC) was also used in this work to track local deformation and plasticity in 300M. DIC uses digital images to measure surface displacement and build 2D or 3D strain maps during the deformation of materials [111]. In the case of 2-dimensional DIC, the displacement is detected directly on the surface of the specimen in question using differences in image contrast and intensity [111] [112]. In order to ensure optimal results, samples must be cleaned and coated with a random surface pattern. In this work, this pattern was created by coating the surface of each sample with white and black spray paint. While digital image correlation was used to track displacement, the load and position data for each test was acquired from the tensile frame. From this data, stress-strain curves were produced and plotted. Strain maps were calculated using Aramis optical measurement software.

3.3 Electron Microscopy

All of the electron microscopy processes and techniques presented in this work were performed at the Canadian Centre for Electron Microscopy (CCEM).

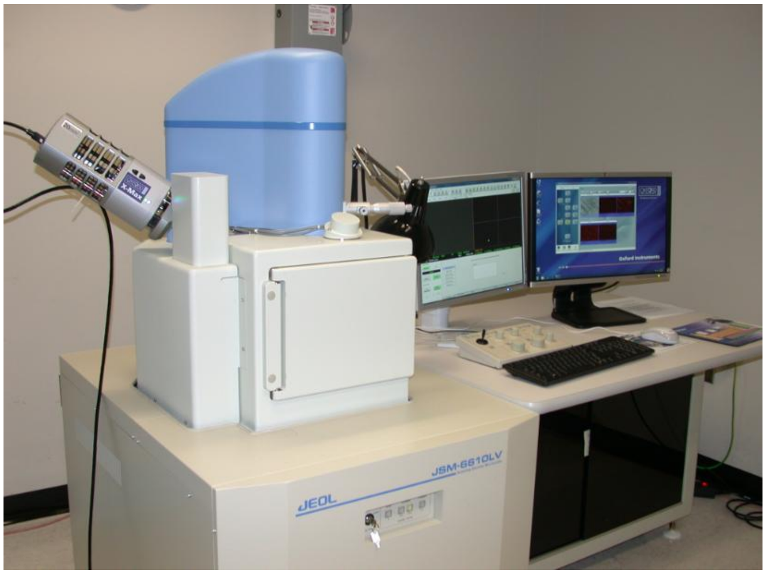

Figure 18: JEOL 6610 LV scanning electron microscope used for fracture analysis and inclusion population classification

3.3.1 Scanning Electron Microscopy (SEM)

Fracture and inclusion analysis was performed using a tungsten filament JEOL 6610LV SEM equipped with an Oxford Instruments electron dispersive spectroscopy (EDS) X-ray analysis system. The EDS system allows for quantitative elemental analysis and mapping of surface features. Electron backscatter analysis was performed on a JEOL 7000F field emission microscope equipped with an EBSD detector.

3.3.1.1 Sample Preparation for SEM

When preparing for SEM analysis, sample preparation is a critical step in ensuring good quality images and data. Fracture surfaces are delicate compared to bulk metal specimens, but require relatively few preparation steps compared to polished specimens required for EDS or EBSD. Unless sectioning is required, fracture surfaces need only be cleaned and mounted before they can be placed into an SEM stage.

Very little sample preparation work was required for the analysis of tensile specimen fracture surfaces due to the nature of the equipment used. The large specimen chamber and a specialized sample vise facilitated the examination of fractured tensile samples without the need for cutting or mounting. Fractured specimens were cleaned as required in order to avoid undesirable interactions with the electron beam and debris or other contaminants.

In order to prepare polished samples for EDS and EBSD, 300M was sectioned and cut to size using a combination of precision and bulk abrasive cutters and 52-Met ceramic wheels. After cutting, metal samples were hot mounted in bakelite. Samples for EDS analysis were polished to 1µm using diamond suspension. After polishing, samples were cleaned to eliminate impurities which can obscure the specimen surface, confuse X-ray analysis, and cause electron charging. Cleaning of metal samples was accomplished using ethanol in conjunction with an ultrasonic bath followed by drying using a compressed gas. After cleaning, samples were stored in a dessicator to mitigate oxidation.

Samples examined using INCA Feature also required some additional preparation before they could be placed into the SEM stage. After cleaning, each sample was painted with conductive nickel paste and dried in an oven at 50°C to minimize charging surface effects. Each sample was then affixed with adhesive copper and aluminum tape strips for EDS and brightness calibration respectively.

3.3.1.2 Inclusion Analysis

INCA Feature analysis was conducted in order to semi-quantitatively examine the inclusion populations in 300M samples. INCA Feature software allows for automated analysis of irregular features such as inclusions and defects in a sample based on brightness and contrast. The software also uses electron dispersive spectroscopy (EDS) to examine the chemistry of each detected feature. After all of the raw data is collected automatically, features can be sorted and filtered into various classifications determined by the user.

For this work, each Feature run was performed using an accelerating voltage of 15kV, 450x magnification, and a work distance of 10mm. Feature detection was calibrated using aluminum tape, and a detection threshold of 150 was used. In each case, the analysis area was a 2x5mm^2 area directly below the fracture surface.

3.3.2 Electron Backscatter Diffraction (EBSD)

Electron backscatter analysis was performed on a JEOL 7000F field emission microscope with a specimen stage well suited to EBSD at the CCEM. Operation of this equipment was performed by an expert technician, not the author.

3.3.2.1 Sample Preparation for EBSD

Sample preparation for EBSD analysis was more rigorous than that required for SEM. Samples were cut and hot mounted using the same process described above but were further polished to 0.1µm and etched using colloidal silica since a minimum of topography is ideal for diffraction, as the diffracted electrons only interact with the top few nanometers of a specimen.

3.3.2.2 EBSD Data Analysis

Electron back-scattered diffraction experiments were performed with the equipment described above, and the resulting data was analyzed using HKL channel 5 software. Noise reduction was performed on all scanned areas, and the prior austensite grain boundary maps were produced by selectively highlighting high angle grain boundaries.

Chapter 4 – Results

The following section describes the experimental results obtained in this work. The first portion describes the methods used to characterize the 300M used in this work, including chemical analysis, hardness testing, and microscopy. The second portion details the mechanical testing under monotonic and interrupted conditions used to investigate strain ageing. The ageing of tensile specimens was conducted under variable loading conditions.

4.1 Material Characterization

The 300M steel used for this work was obtained from a forged and heat-treated bar from an industrial supplier, and as such the as-received condition was examined using a variety of mechanical and chemical testing methods. The composition of the steel is given below in Table 4.

Element	Minimum Content by Weight (±0.005)	Maximum Content by Weight (±0.005)
Carbon	0.40	0.45
Manganese	0.60	0.90
Silicon	1.45	1.80
Phosphorous	-	0.010
Sulfur	-	0.010
Chromium	0.70	0.95
Nickel	1.65	2.00
Molybdenum	0.30	0.50
Vanadium	0.05	0.10
Copper	-	0.35

Table 4: Elemental composition limits for the 300M steel used for this work

The composition of 300M is nearly identical to that of AISI 4340, the parent steel modified to create 300M. Silicon is the most notable alloying addition, as it has a number of effects on the phase structure and mechanical properties of steel, as discussed previously. The other significant difference is a lower impurity content than the base steel due to the vacuum-arc-remelting (VAR) process to which 300M is submitted in order to meet high standards of strength and toughness.

In order to meet such high standards, the bulk of the material used for this work was submitted to an exacting and highly controlled heat treatment process, as shown below in Table 5.

Treatment	Process Temperature (°C)	Process Time (Hours)
Austenitize	871	-
Quench	25	-
Snap Temper	140	1
Double Temper Step 1	302	2
Double Temper Step 2	302	2
Machining	-	-

Table 5: Industrial thermo-mechanical treatment for 300M steel

After tempering, the material was machined into the various sample geometries used for experimentation. Industrial samples of 300M are subjected to additional processing steps, including shot peening, plating, and baking. The majority of the material used for this work was processed up to the double tempering step, and not shot peened or subjected to plating and baking. It is also important to note that the samples remained at room temperature in bar form for a period of several years before machining. The notched samples were tempered slightly differently from the rest of the material, as they were received from a different industrial supplier. Each notched specimen was tempered at 190.5°C after machining in order to relieve induced stresses.

4.1.1 Chemical Analysis

The impurity levels in the as-received steel were investigated using glow discharge optical emission spectroscopy (GDOES). All GDOES analysis was performed by technical staff in the materials science and engineering department at McMaster University. Particular attention was paid to phosphorus and sulfur as both elements are well-known embrittling agents. The level of carbon was also measured, as it has a significant effect on the mechanical properties of steel. Chemical testing results are displayed in Table 6.

Measurement (wt%)	**Carbon**	**Sulphur**	**Phosphorus**
1	0.41	≤0.0005	≤0.005
2	0.38	≤0.0005	≤0.005
3	0.39	≤0.0005	≤0.005
Average	**0.39**	**≤0.0005**	**≤0.005**

Table 6: GDOES elemental impurity results for as-received 300M

Chemical analysis revealed no abnormalities in the impurity level of the as-received 300M, as the impurity content was well below acceptable limits. The amount of carbon was slightly low in some regions, but not significantly different than the specified composition. Oxygen and nitrogen analysis was also performed by Cambridge Materials Testing. The oxygen and nitrogen levels observed during the testing were normal, as seen below in Table 7.

Test #	**Oxygen Content (ppm)**	**Nitrogen Content (ppm)**
1	17	11
2	16	13

Table 7: Gaseous element testing results displayed in parts-per-million

4.1.2 Hardness Characterization Analysis

Mechanical characterization was also performed in order to determine the consistency of the microstructure and composition of the as-received material. A shot peened industrial sample was tested alongside untreated material with the additional goal of determining the effect of shot peening on the hardness distribution in the material. Hardness testing was performed on Matsuzawa micro-hardness testing equipment in conjunction with Clemex CMT HD analysis software. Due to the expected high hardness of the material, the applied load used for indentation was 1000gf. Hardness values were originally measured in Vickers hardness (HV) and converted to Rockwell C (HRC) in order to better compare with industrial data. Before testing, the equipment was calibrated in order to ensure consistent and accurate measurements. Calibration was conducted using a steel test block, and demonstrated a margin of error no larger than 5HV for a given measurement. The subsequently obtained hardness data is shown below in Figure 19.

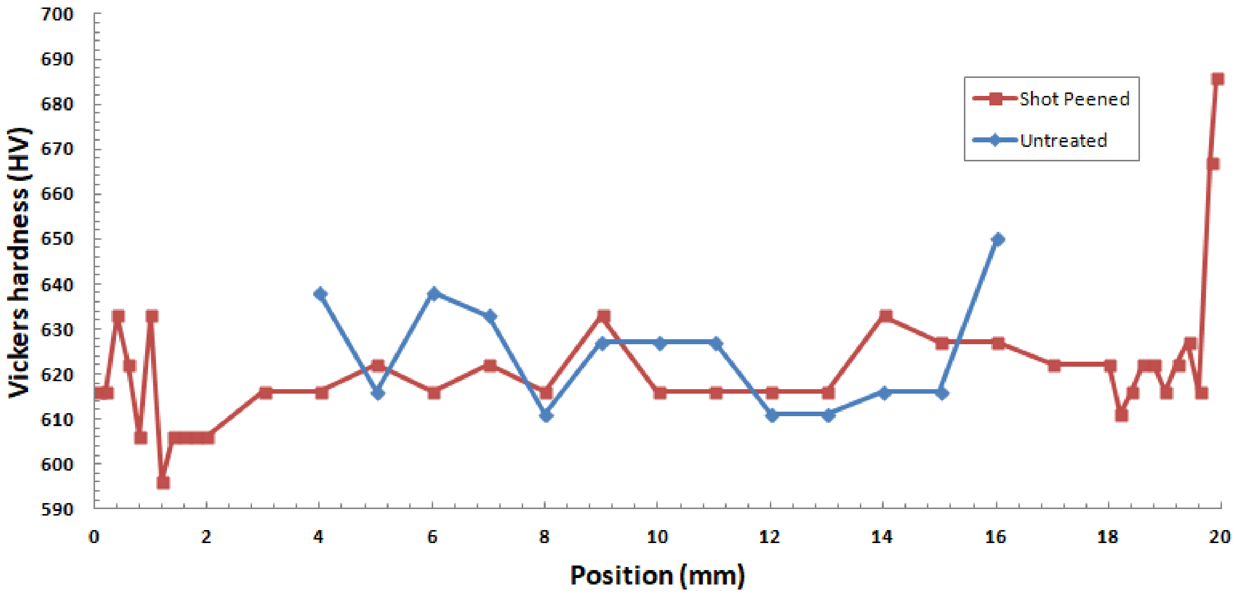

Figure 19: Vickers hardness profiles for shot peened and untreated industrial samples

Hardness testing revealed an average hardness of 625HV (56.6 HRC) in the untreated material. The hardness profiles contained some points with a greater hardness than the industrial average (53-56 HRC) but these were not dramatically larger. The significantly higher hardness values observed near the edges of the shot-peened sample are due to the compressive stress layer induced by the process which is standard for industrial components. This compressive stress field permeates to a depth of up to 200µm from the shot peened surface as shown above. While the bulk of the specimens used for tensile testing were not shot peened, one set of samples was shot peened to industrial standards and compared to untreated specimens to determine the effect of shot peening on the ageing and mechanical properties of 300M.

4.1.3 Microstructure and Characterization

Several different microscopy techniques were utilized to characterize and confirm the microstructure of the as-received material. Optical microscopy confirmed the general microstructure of tempered 300M, while transmission electron microscopy was used to examine the precipitate population and retained austenite content.

4.1.3.1 Optical

Optical microscopy was used to qualitatively examine the microstructure of 300M in the as-received condition. Samples were prepared from leftover material after machining, and were automatically polished to a finish of 1µm using diamond lubricant. After polishing, a 2% Nital solution was used to reveal the microstructure.

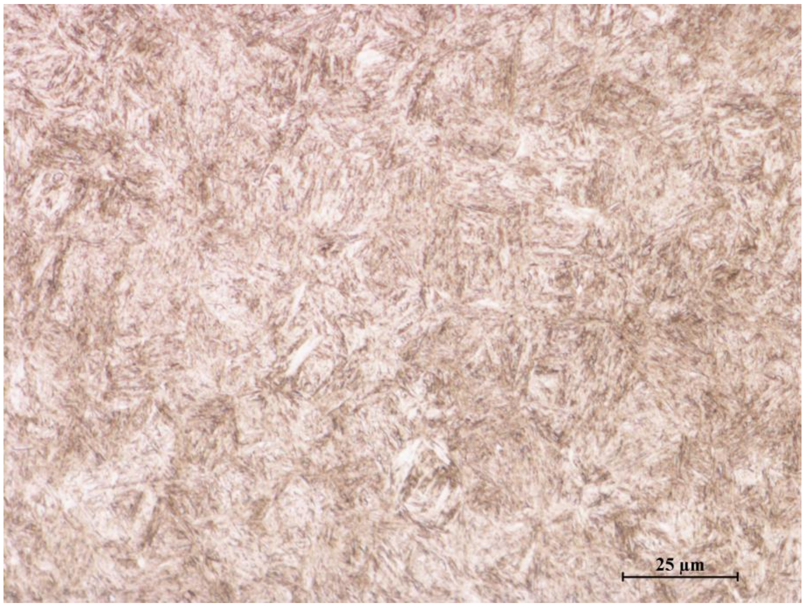

Figure 20: Image of the microstructure of 300M in the as-received condition, taken at 50x using an optical microscope

As shown in Figure 20, the microstructure of 300M after tempering at 302°C is comprised primarily of a homogenous fine lath structure. The prior austenite grain size of the material in the as-received state was examined using electron backscatter diffraction, as these grain boundaries were not revealed through etching. Results are shown in the following section (4.1.3.2).

4.1.3.2 Electron Back Scatter Diffraction (EBSD)

Electron backscatter diffraction was performed to identify and confirm the grain structure of the as-received 300M material. One site from the center of a large industrial specimen was examined in order to determine the grain size and structure of the material. As mentioned previously, HKL Channel 5 software was utilized to construct the inverse pole figure (Figure 21a) and prior austenite grain boundary maps (Figure 21b) shown below.

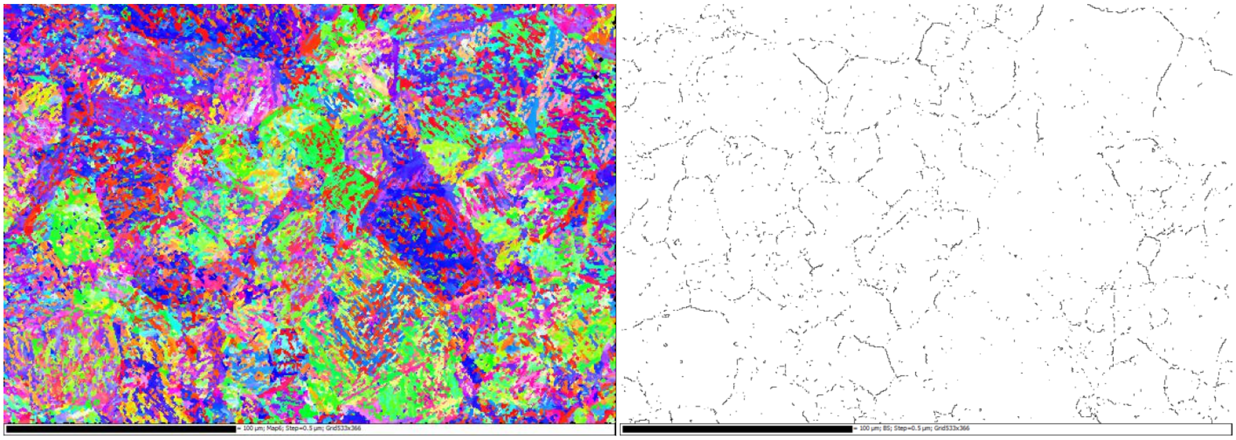

Figure 21: (a) Inverse pole figure (left), and (b) prior austenite grain boundary map (right) taken from the center of an industrial sample prepared for EBSD

EBSD yielded enough information to accurately reveal the grain boundaries of both specimens, which allowed for post analysis using ImageJ software. This analysis was done in order to determine an average grain size for each sample. The average grain size was calculated by measuring the maximum x and y diameters of randomly selected grains from each set of maps. The tabulated average and median measurements for the center of the material is available in Table 8. The measurements were obtained by examining a total of 20 grains from the center and edge regions. No retained austensite was detected in the region selected for EBSD, but the presence of interlath retained austenite was confirmed using TEM.

	Average X (±1µm)	**Average Y (±1µm)**	**Median X (±1µm)**	**Median Y (±1µm)**
Center	32	30	28	25

Table 8: Average and median grain size measurements taken from the center of an industrial 300M sample prepared for EBSD

Grain size measurements and a cursory visual examination suggest that the grain size at the center of the large industrial specimen is approximately 30µm, which is in perfect agreement with the expected grain size of 30µm. The grain size was also fairly uniform across the examined area. No definitive conclusions about grain size and overall distribution can truly be drawn from such a limited number of grain measurements, but the above analysis is sufficient for the purposes of general characterization.

4.1.3.3 Transmission Electron Microscopy

Transmission electron microscopy (TEM) was performed on quenched and tempered 300M samples to classify both the retained austenite distribution and carbide population after heat treating. The material was tempered at ~300°C for 4 hours, the same tempering treatment used for the as-received material described above.

Analysis revealed that the bulk of the retained austenite existed between laths, and was stable after tempering at temperatures up to 300°C, since no cementite was detected. The thickness of the retained austenite films varied from approximately 0.05-0.2µm, while the lath width ranged from about 0.08-0.5 µm. Images of the TEM conducted on 300M tempered at 300°C are available in Figure 22.

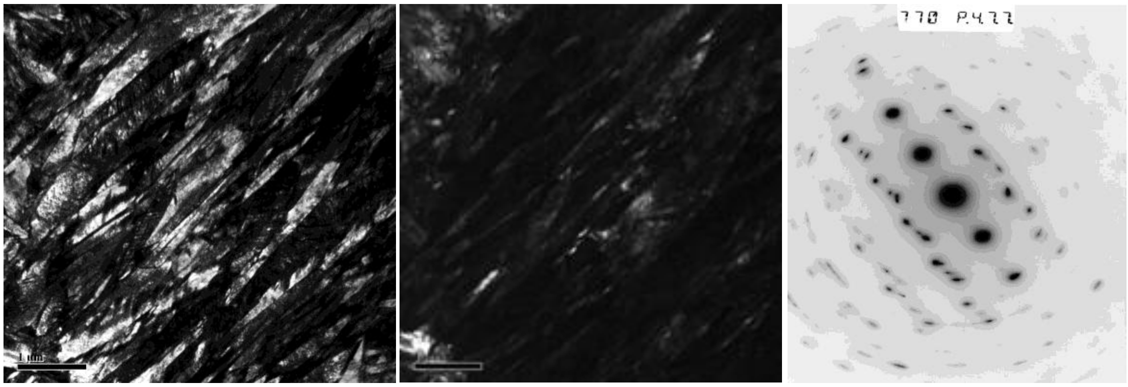

Figure 22: TEM images of interlath retained austenite films in 300M quenched and tempered at 300°C for one hour

TEM also revealed the presence of transition carbides which persist in 300M at higher tempering temperatures than in 4340. The precipitates coarsened to a maximum of 500nm in length and 25nm in width and were predominantly identified as ε-carbide using selected area diffraction (SAD). This result is in agreement with the work of Padmanabhan and Wood, who determined that the transition carbide present in 300M tempered at 280°C is ε-carbide [43].

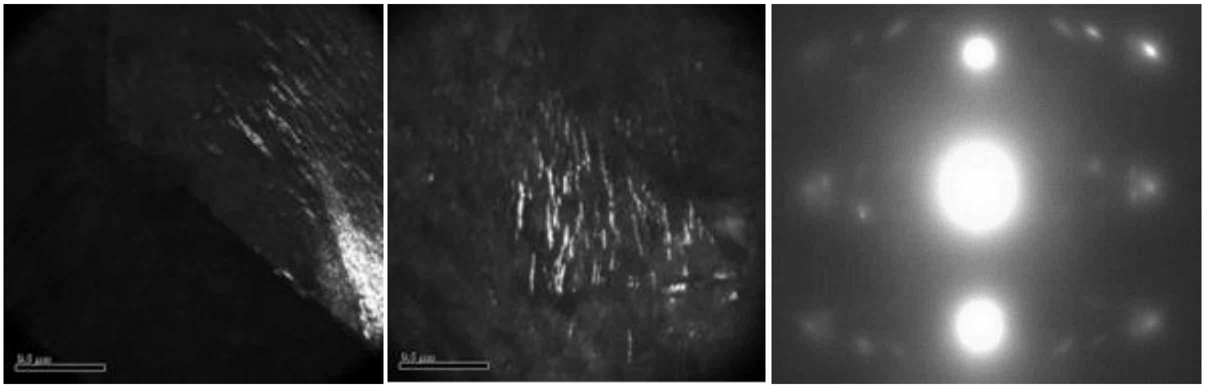

Figure 23: TEM images of transition carbides in 300M steel after quenching and tempering for 4 hours at 300°C

4.2 Mechanical Testing

4.2.1 Monotonic Tensile Testing

In this work, “monotonic” is used to describe all tests which did not include an ageing step, meaning they proceeded directly to failure at a fixed deformation rate. Monotonic tensile tests were initially used to provide a baseline for the deformation behaviour of 300M, and to determine the variance of properties between different batches. A comparison between selected monotonic stress-strain curves is shown below in Figure 24. Most monotonic testing was conducted using a crosshead speed of 1mm/min, which corresponds to a strain rate of 0.00133s^{-1}. Exceptions to this were the samples which were deliberately tested at different strain rates.

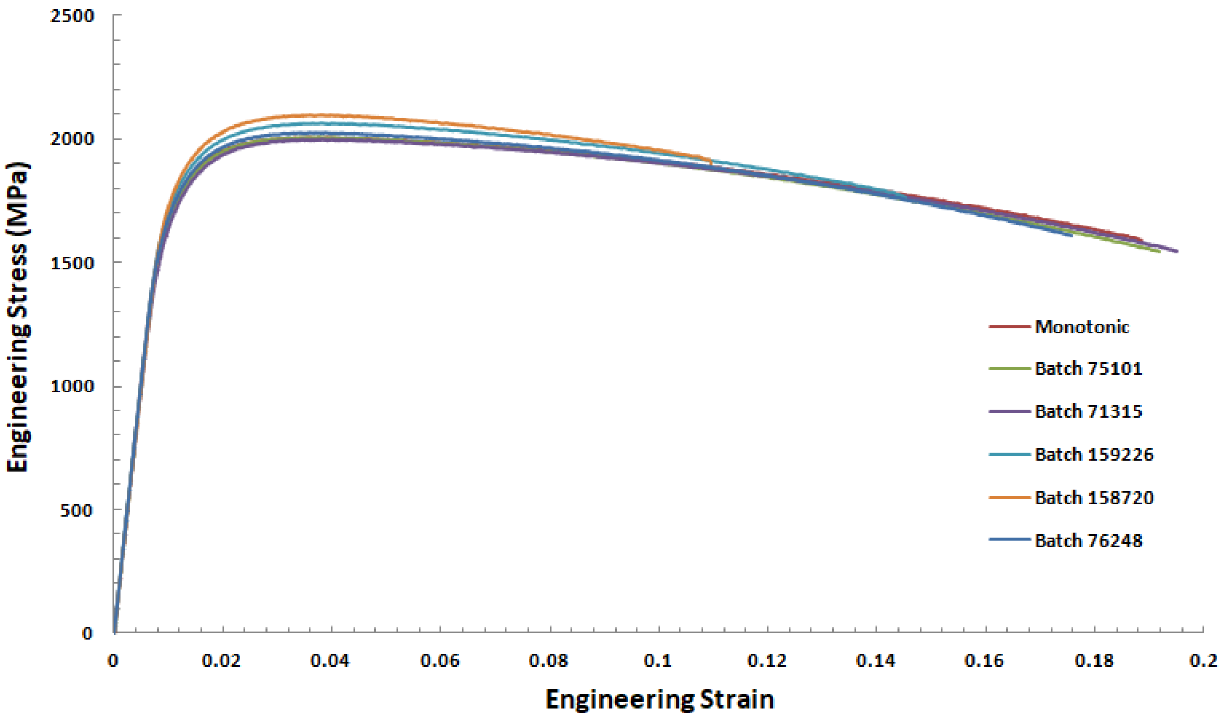

Figure 24: Stress-strain curves for a selection of monotonic tensile tests conducted at a crosshead speed of 1mm/min

The monotonic curves show relatively consistent behaviour, with the exceptions of the samples from batch 158720, and to a lesser extent, batch 159226, which failed at much earlier strains than expected due to deliberately increased inclusion populations. These batches of material were deliberately obtained in order to examine the effect of inclusion populations on mechanical behaviour, and as such these samples may be regarded as outliers. With this in mind, the average failure strain ranges from 0.17-0.195, and the average ultimate strength is just above 2000MPa. It is notable but perhaps not surprising that the samples which display the highest ultimate strength also fail at the earliest strains. All samples demonstrated a yield point of approximately 1550MPa regardless of subsequent deformation behaviour. Reduction in area measurements were performed on all specimens using full fracture images and the initial dimensions of the tensile specimens, and the average reduction in area for samples deformed monotonically was 40%.

Notched specimens were also tested in addition to round tensile samples. Monotonic testing was also performed for this specimen type in order to capture the differences in plasticity caused by sample geometry and state of stress. Stress-strain data for a monotonic test of a notched sample is shown below in Figure 25.

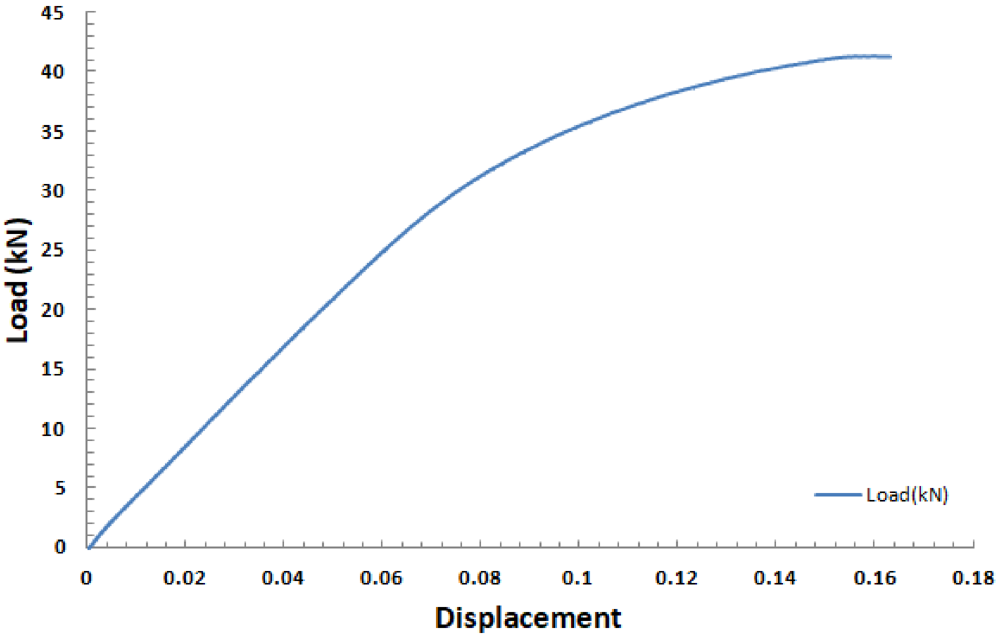

Figure 25: Continuous tensile test data for a notched specimen tested using a crosshead speed of 1mm/min

Upon examination of the notched test data, several differences become apparent when comparing the data to that obtained from the round samples. Firstly, the maximum load reached in the notched geometry is slightly higher than in the round samples, and the failure strain is also an order of magnitude lower. The decrease in failure strain is likely due to the increase in stress triaxiality at the notch.

4.2.1.1 Digital Image Correlation

Digital image correlation was also performed for samples loaded monotonically to failure. This was done primarily to provide baseline plastic behaviour, which could later be compared to aged specimens. Monotonic tensile testing was performed for a flat 300M sample at a rate of deformation of 1mm/min as shown below.

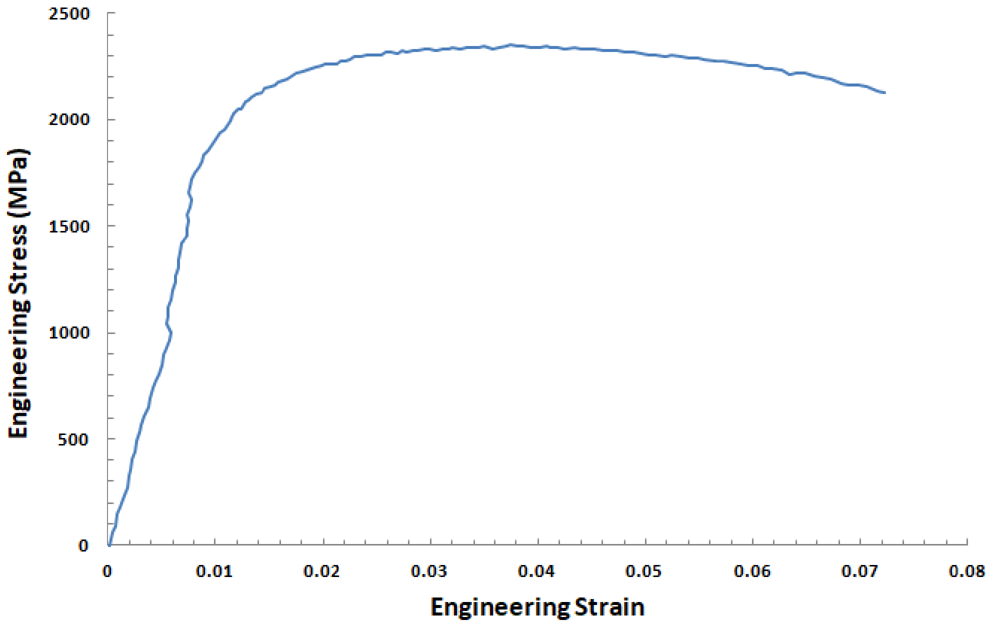

Figure 26: Stress-strain curve for flat sample tested at a speed of 1mm/min, using digital image correlation to track deformation

Monotonic testing performed in conjunction with DIC once again demonstrated significant differences in mechanical behaviour when compared to the round samples. The reduced strain to failure may be explained by the flat geometry used, but the significantly increased stress experienced by the sample is difficult to interpret. The rough appearance of the curve is due to the relatively low data acquisition rate possible with DIC when compared to data gathered via extensometer. The maximum memory capacity of the Aramis system used in this work limits the total number of images that can be captured per test, so for low strain rates a lower acquisition rate must be used.

Strain maps produced using Aramis software revealed significant localized plasticity in un-aged 300M, as demonstrated in Figure 27.

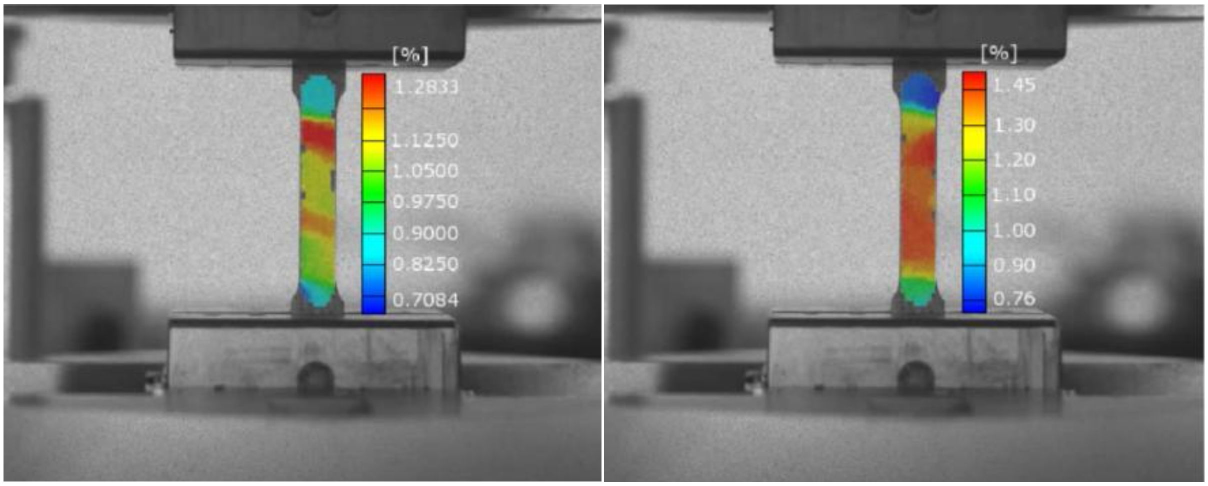

Figure 27: DIC strain maps corresponding to monotonic deformation of 300M at a speed of 1mm/min

As shown above, the localized plasticity presented itself as diagonal bands which formed on the surface of the specimen well before the beginning of necking, and propagated parallel to the loading direction. This behaviour is highly reminiscent of Luders bands, and promoted further investigation in this work. The propagation of the bands was identical in both flat and round samples.

Digital image correlation was also performed with very high capture rates (10 images per second) in order to better visualize the localized plasticity in 300M. One experiment was performed on a round sample due to material limitations. Although the round nature of the specimen was not ideal for 2D DIC, the strain maps of the test present clear evidence of band propagation as shown below. The propagation of these bands can be observed by creating a section plot of the strain in the pulling direction of a tensile specimen, and carefully plotting the resulting strain profiles. In order to properly visualize the propagation of bands, the strain from every 50th frame up to frame number 400 was plotted, as shown in Figure 28.

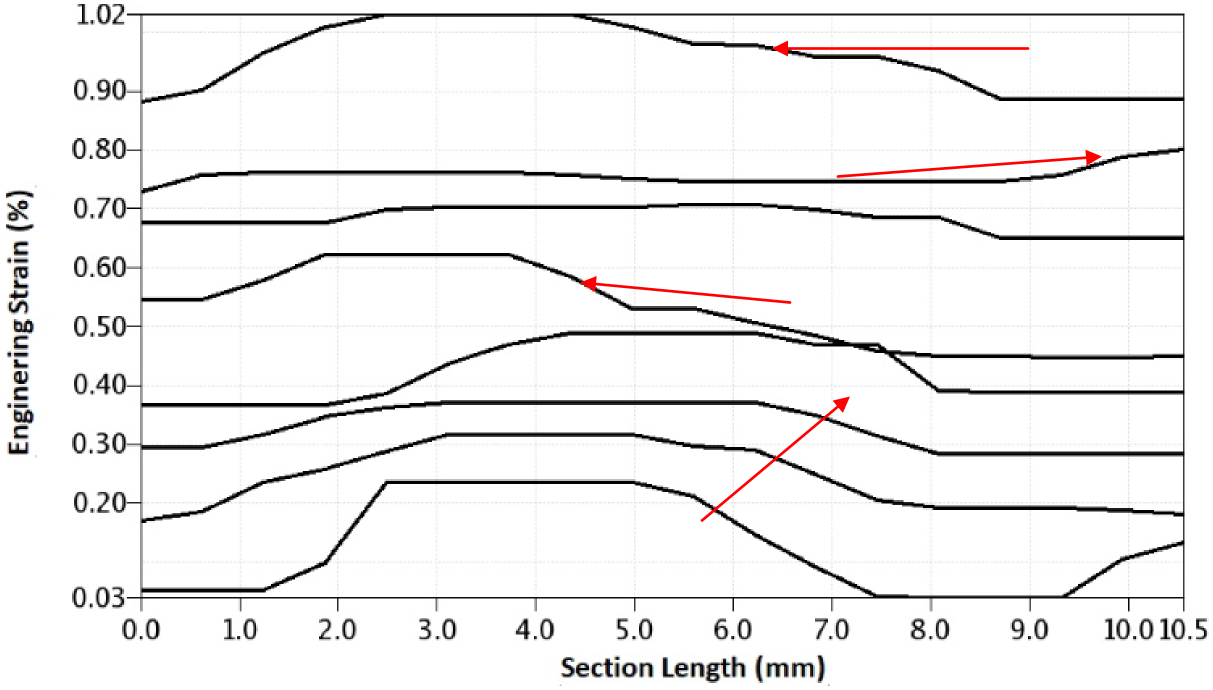

Figure 28: Section line strain plot for a round tensile specimen deformed monotonically to failure using a crosshead speed of 1mm/min ($0.00133s^{-1}$)

As shown above, the wave-like propagation of bands of localized plasticity in 300M can clearly be observed after careful analysis. The propagation of the deformation bands was observed much more clearly when a high capture rate was used.

4.2.1.2 Effect of Strain Rate

In order to determine the effect of strain rate on the deformation behaviour of 300M, data was also gathered with an acquisition rate 10x greater than used previously, allowing for extremely fine detail to be captured in a tensile test. The results of the high acquisition rate testing can be seen below in Figure 29.

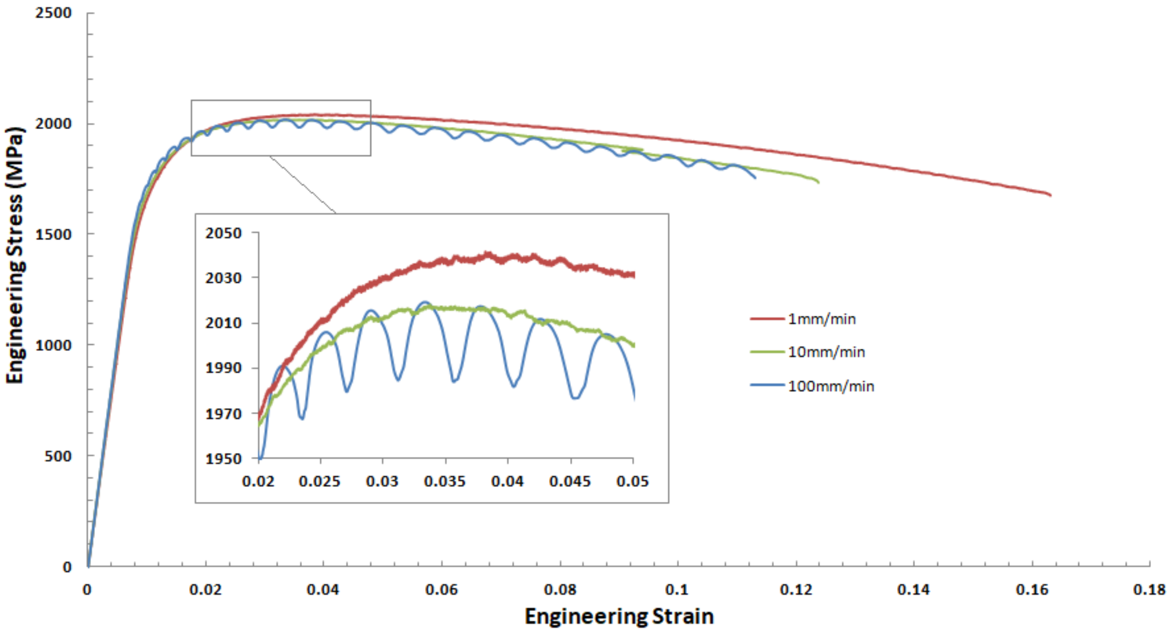

Figure 29: Stress-strain curves for round samples resulting from continuous tensile testing with a tenfold increase in data acquisition speed

As shown above, 300M appears to exhibit distinct serrations. Serrations are typically indicative of dynamic strain ageing, and should disappear as the strain rate is further increased [56]. The material also appears to exhibit slight negative strain rate sensitivity, as the strength of the material decreases with increasing strain rate.

The strong serrations observed at high deformation rates were further investigated by testing at even larger rates. A duplicate test was performed at a rate of 100mm/min, and this data was compared with results obtained by performing experiments at 200 and 300mm/min. Such high rates of deformation required further increases in data acquisition speed to accurately capture the deformation of the tensile specimens. At rates of 200-300mm/min data was acquired at a rate of 3333 points per second. The results of these tests can be seen below in Figure 30.

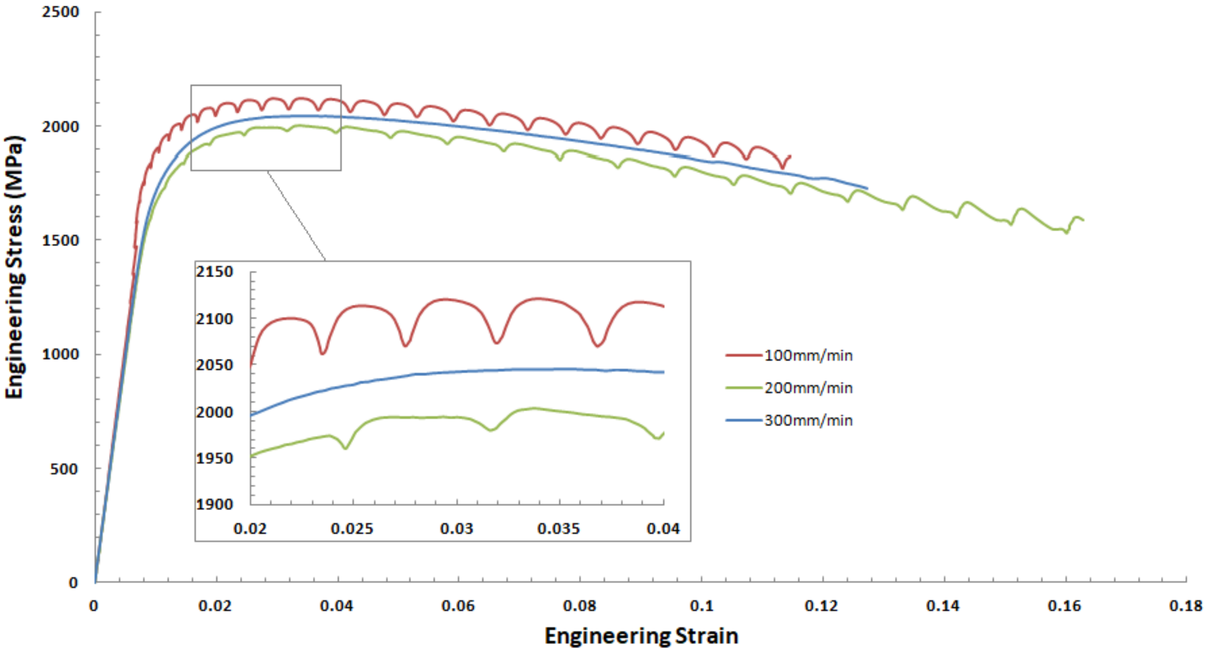

Figure 30: Stress-strain curves resulting from continuous tensile testing with greatly increased deformation and data acquisition rates

As shown above, serrated flow persists for strain rates of up to 0.266s^{-1}, equivalent to a crosshead speed of 200mm/min. At rates above 0.399s^{-1} (300mm/min), no serrated flow was observed. The specimen deformed at a speed of 100mm/min likely experienced slippage during the test, which is implied by the extremely unusual behaviour which begins before the yield point of the material is reached. The fact that the samples deformed more rapidly yielded in a nearly identical manner, and the extreme slope of the 100mm/min curve near the yield point strongly imply that the 100mm/min specimen slipped during a portion of the testing.

4.2.1.4 SEM Fracture Analysis

Fracture analysis was conducted using SEM to determine the failure mechanism of tempered 300M after continuous deformation. All sample geometries were examined in order to provide baseline behaviour for each type.

The first geometry examined using SEM was the round sample type used for the bulk of the experiments in this work. An example of a fracture surface observed after continuous deformation to failure can be observed in Figure 31.

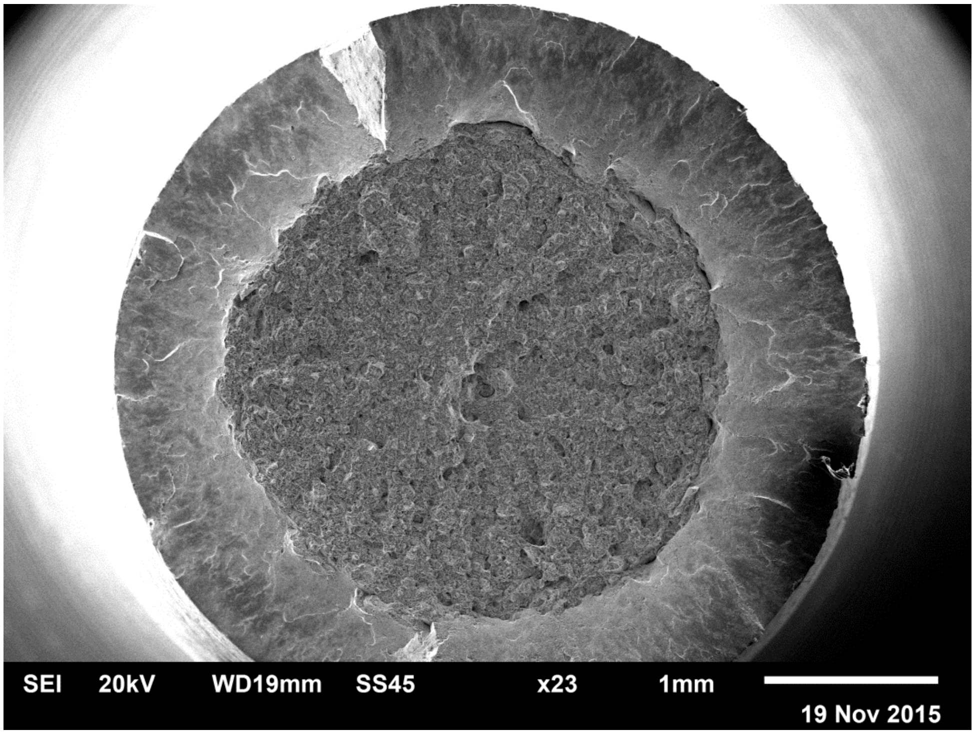

Figure 31: SEM fracture image for a sample deformed continuously to failure at room temperature at a speed of 1mm/min

As shown above, the samples which were deformed monotonically displayed a “cup and cone” fracture surface which is traditional of ductile metals. Dimples are evident, which are due to the nucleation and growth of voids occurring in the material prior to failure. At higher magnification, it can be observed that the failure surface exhibits significant topography, a feature displayed in Figure 32.

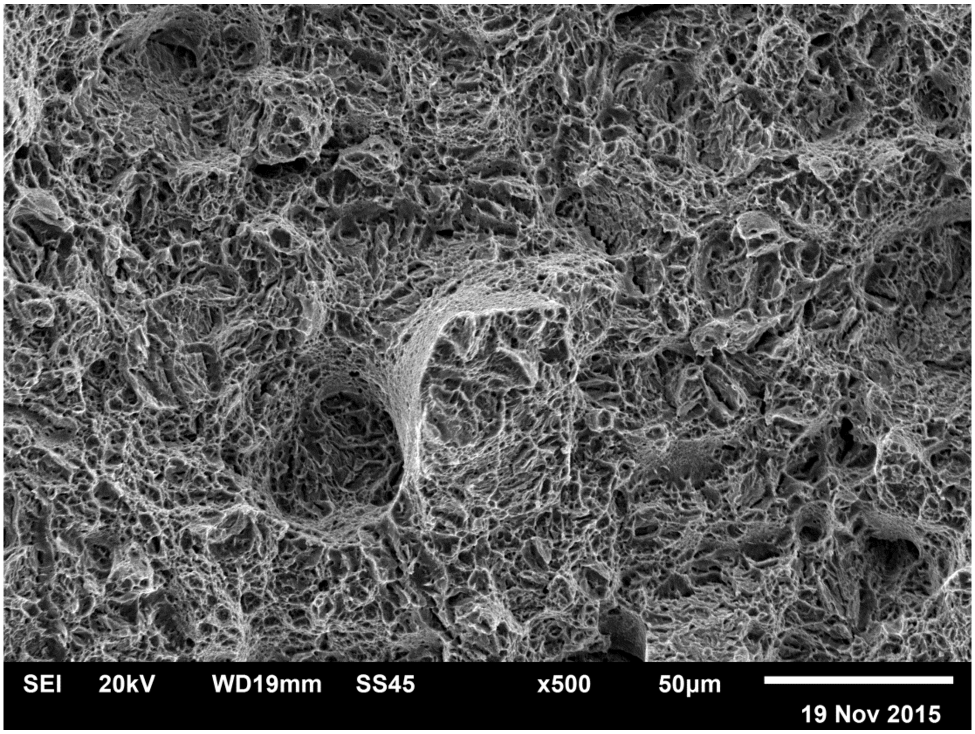

Figure 32: SEM failure image taken at 500x magnification for a sample deformed continuously to failure at room temperature at a speed of 1mm/min

Indeed, cylindrical features tens of microns in diameter resembling terraces or pits are evident throughout the center of all failure surfaces. These “terraces” are not due to the formation of large voids, as fine dimples can be observed along the edges of each such feature. The size of such features may be significant, as the relative size of such features is comparable with the 30µm grain size measured earlier. Clear evidence of void linkage may also be observed as linked lines of dimples on the failure surface.

Flat and notched specimens were also examined using SEM after monotonic deformation. Flat specimens displayed a reduction in dimples along some flat faceted regions, which may be the result of an increase in mixed-mode fracture in this sample geometry. Notched specimens displayed significant evidence of facets, which indicates a clear mixed fracture mode. While void formation is still evident, it is clear that cracks have propagated across the surface and been arrested by structural features, resulting in the presence of facets. This failure mode is reminiscent of quasi-cleavage, since no clear evidence of intergranular or ductile-intergranular failure can be seen. Images from both sample types are available below in Figure 33.

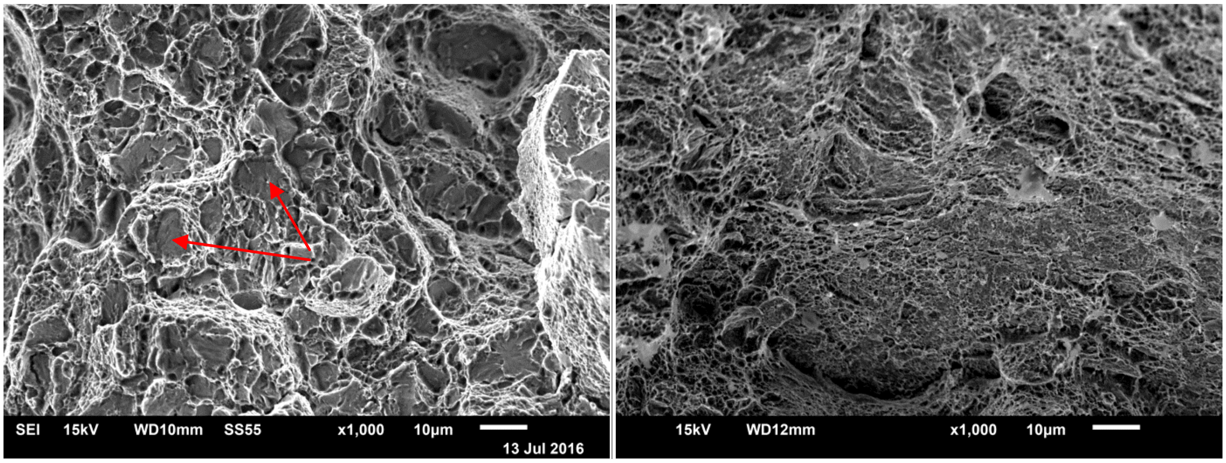

Figure 33: SEM fracture images taken at 1000x times magnification for notched (left) and flat (right) samples monotonically deformed to failure

4.2.2 Interrupted Tensile Testing

Interrupted tensile tests were conducted in order to investigate the effects of ageing on plasticity in 300M. In each case, 300M samples were deformed to a given initial strain and aged at a fixed temperature for a set time. The strengthening observed upon re-loading aged samples was measured by comparing the 0.2% offset stress of the re-loading curve with a monotonic test at the same level of strain.

The effect of room temperature ageing over a short time period was investigated by deforming samples to ~2.5%, unloading, and holding at room temperature for time periods ranging from 1 minute to 1 hour. Stress strain curves for the short time ageing are displayed in Figure 34.

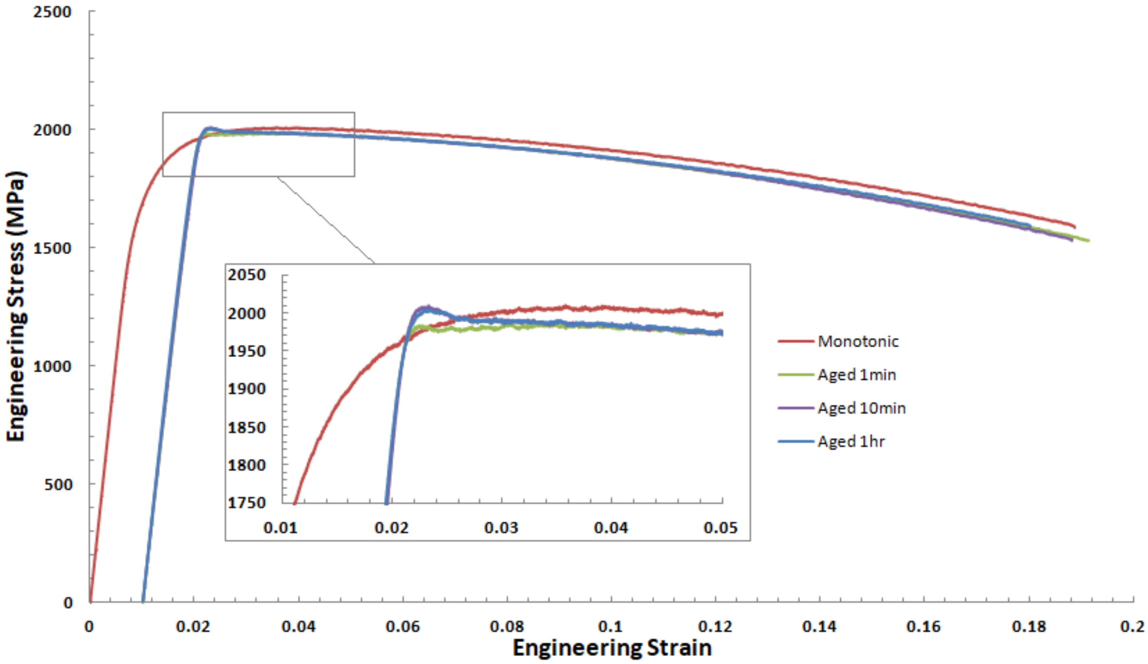

Figure 34: Stress-strain curves resulting from short time ageing at room temperature after an initial deformation of 2.5% at a speed of 1mm/min

Ageing for 1 minute at room temperature produced an increase in stress of approximately 5MPa, while ageing for up to one hour resulted in a strengthening of 30MPa. Notably, ageing for times between 10 minutes and 1 hour did not yield appreciably different results.

Ageing experiments were also conducted for intermediate times ranging from 4 to 72 hours. Two experiments were conducted for this time period, one on standard machined round specimens, and one on samples which were shot peened to industrial standards. This had the dual purpose of examining both the effects of ageing time and shot peening on the mechanical behaviour of 300M. Both types of specimens were deformed to approximately 2.5% and aged at room temperature for varying times. The samples which were not shot-peened showed no significant increase in stress compared to 1 hour of ageing, with increases of approximately 25-30MPa observed upon re-loading. Shot peened samples aged for periods between 4-72 hours on the other hand showed a significant increase in stress, with a maximum observed Δσ of over 65MPa with no corresponding reduction in ductility observed. Stress-strain curves corresponding to the shot-peened samples aged for intermediate times are available in Figure 35.

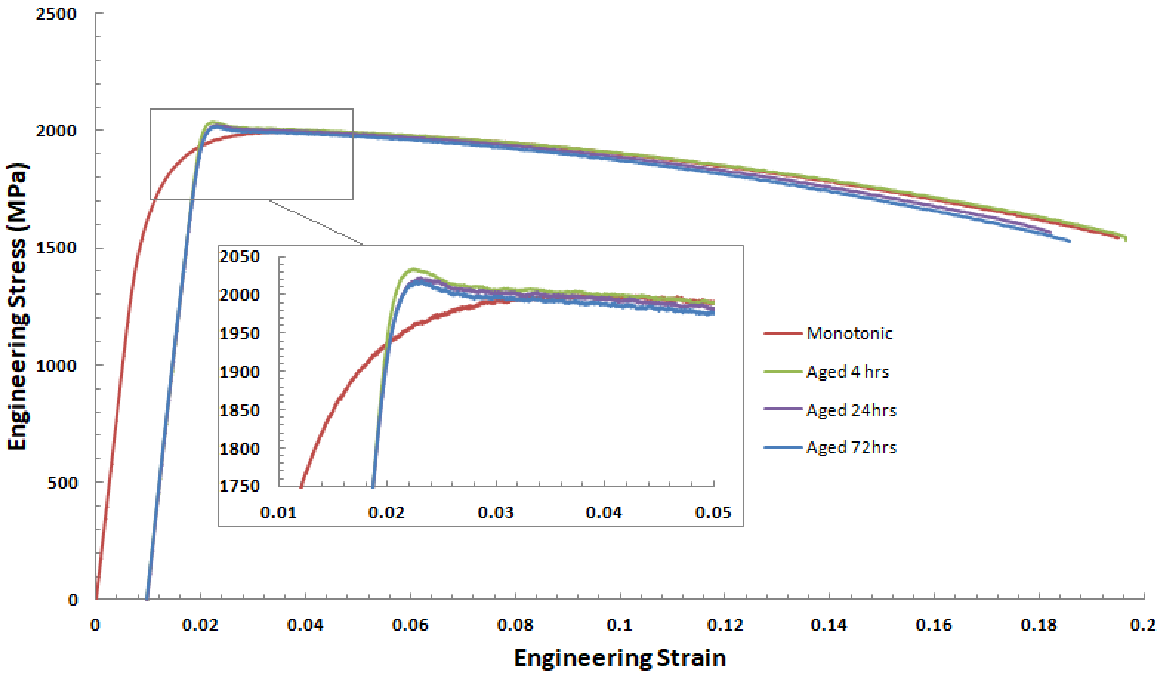

Figure 35: Stress-strain curves for shot-peened samples resulting from ageing at room temperature for periods between 4 and 72 hours, after an initial deformation of 2.5% at a speed of 1mm/min

In addition to investigating the effect of ageing time, the influence of the initial deformation or "pre-strain" was examined. Round tensile specimens were deformed to various low strains ranging from 1-2.5% and aged for one hour at room temperature. The resulting stress strain curves demonstrated that increasing the initial deformation increased the magnitude of the transient increase in strength observed upon re-loading, at least up to 2.5% initial deformation. This trend can be observed below in Figure 36.

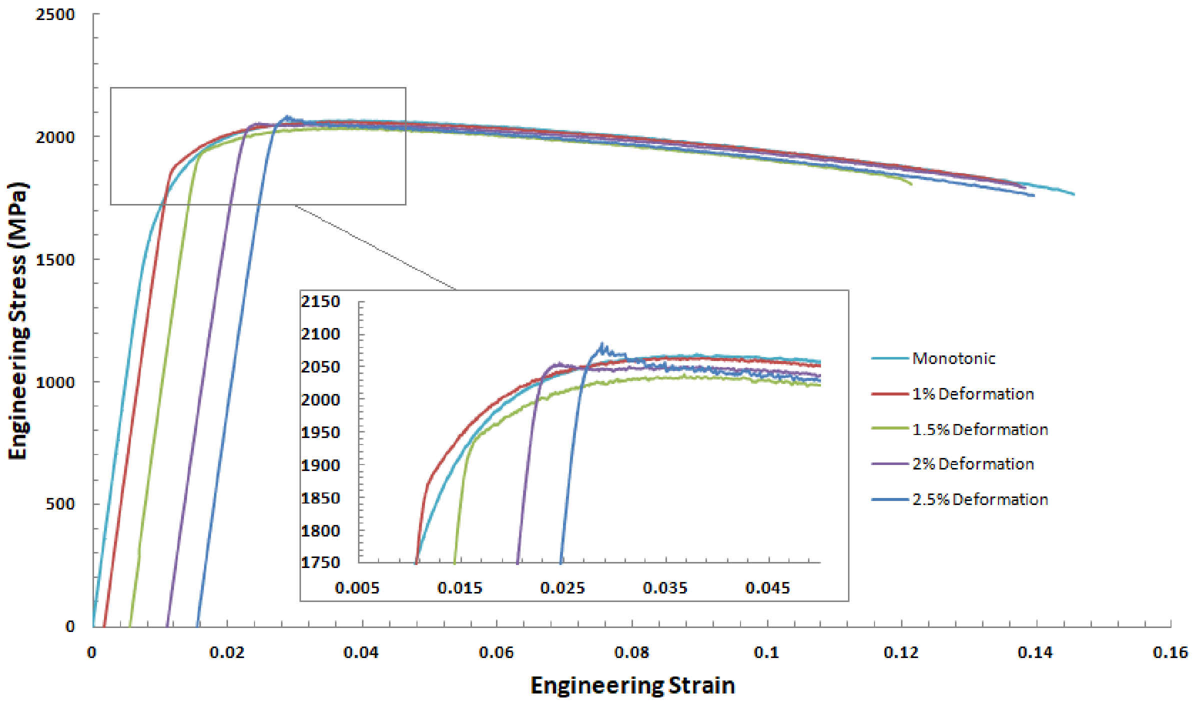

Figure 36: Stress-strain curves for specimens loaded to failure after ageing for 1 hour at room temperature. Initial deformation was conducted at a speed of 1mm/min

All samples displayed measurable strengthening given the relatively short ageing time, with the exception of the sample initially deformed to 1.5%. A clear positive correlation can be observed between the initial amount of pre-strain and the amount of strengthening which occurs upon re-loading.

The same experiment was repeated with significantly longer ageing times to determine the effect of very long ageing times on strength and plastic behaviour. The experimental results for tensile tests using low initial strains and an ageing time of ~650 hours are displayed in Figure 37.

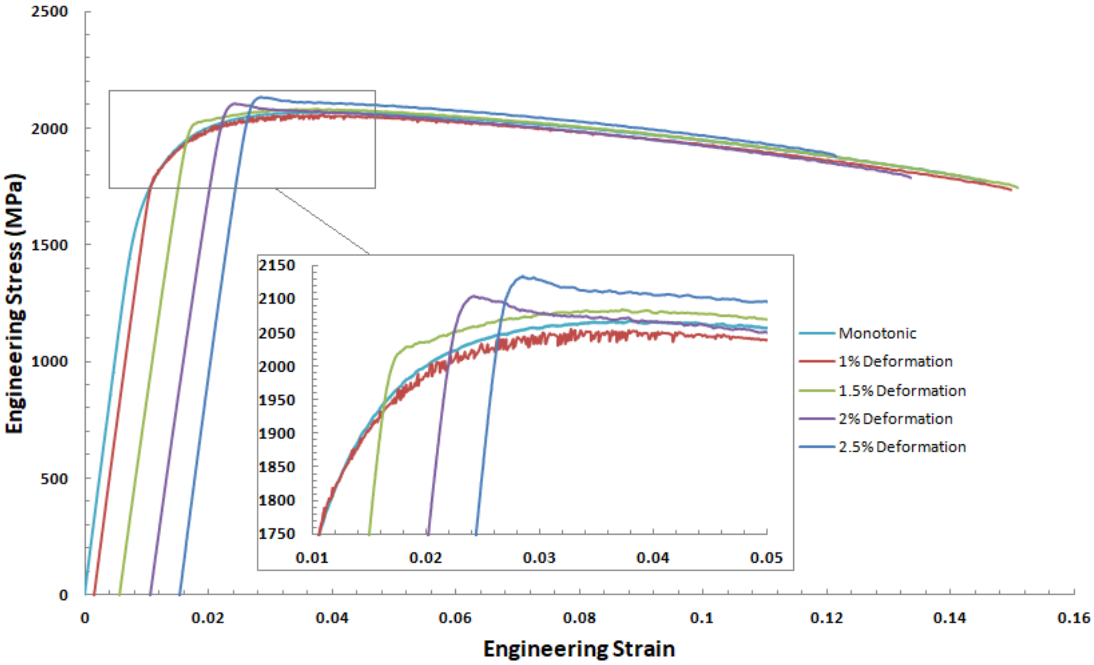

Figure 37: Stress-strain curves for specimens loaded to failure after ageing for 650 hours at room temperature. Initial deformation was conducted at a speed of 1mm/min

A notable feature of the samples aged for long times is that the flow stress does not decrease below the monotonic level, which is usually observed. The significant increase in flow stress and less prominent transient imply that a mechanism other than dislocation locking is active.

The influences of pre-strain and ageing time on the plastic behaviour of 300M were further investigated through tensile tests which used higher levels of initial strain and variable ageing times. One set of samples was deformed to an initial strain of 5% and aged for times ranging from 15 minutes to 4 hours. The stress-strain results from this testing procedure are shown in Figure 38.

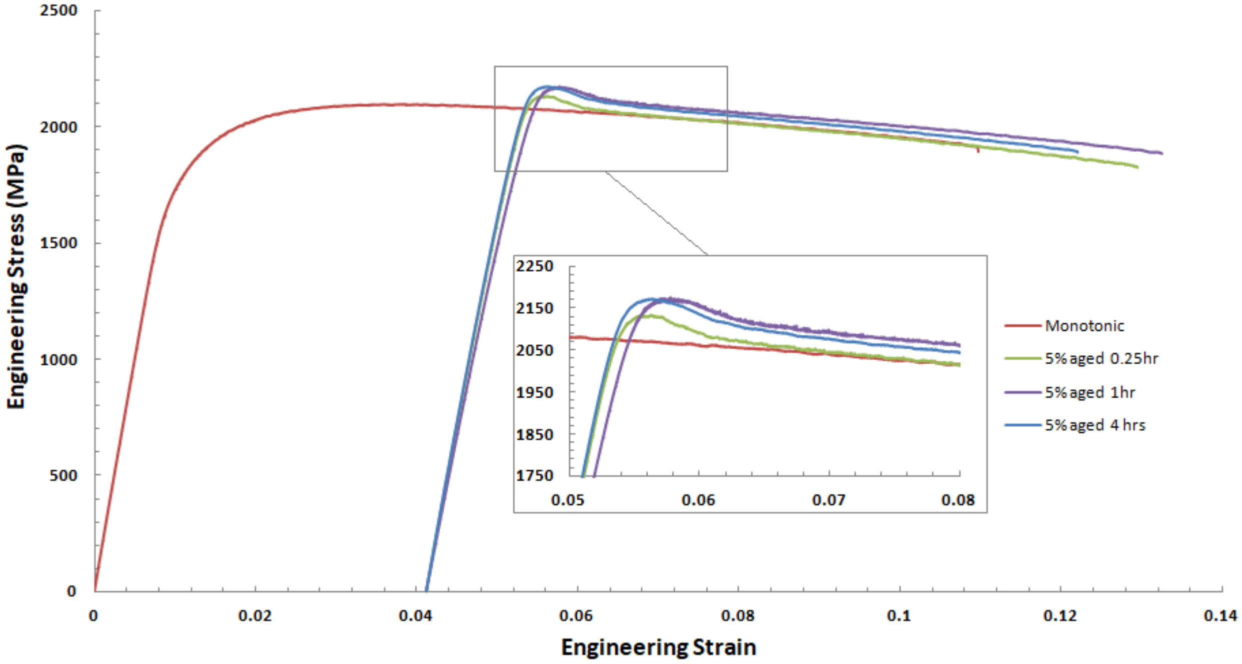

Figure 38: Stress-strain curves for round tensile samples pre-strained to 5% and then aged for various times as shown

The results for the larger pre-strain of 5% show good agreement with ageing treatments performed at lower strains discussed earlier, in that the measured increase in strength due to ageing is a strong function of time for times up to 1 hour. The stresses reached in the samples deformed to 5% were larger, however, due to the additional work hardening produced by further deformation.

Further experiments were conducted with larger pre-strains, up to 8%. The ageing time for this set of specimens was 4 hours at room temperature. The compiled stress-strain curves resulting from this testing are shown below in Figure 39.

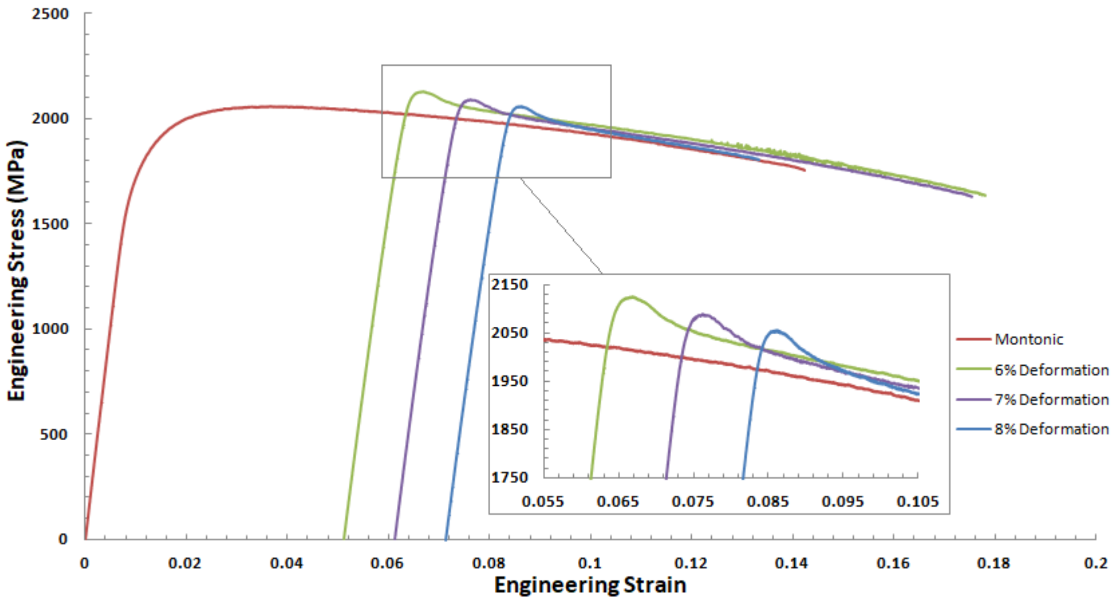

Figure 39: Stress strain curves for samples deformed to large initial strains and aged 4 hours at room temperature

Increasing the level of pre-strain beyond 5% resulted in a small increase in stress for the sample initially deformed to 6%. Subsequent decreases in strengthening were seemingly observed, however, as the material was deformed beyond 6%. It is somewhat difficult to compare samples deformed past necking directly, but the benefits of strain ageing are clearly diminished beyond an initial deformation of 6%. This is in good agreement with the results of Stephenson and Cohen, as well as other authors who found that there are practical limits to the strengthening which can be achieved in 4340 and 300M by strain ageing in tension [110].

In order to summarize the effects of ageing time and pre-strain on the strengthening of 300M, 0.2% offset stress measurements were compiled and plotted as shown in Figure 40 and Figure 41.

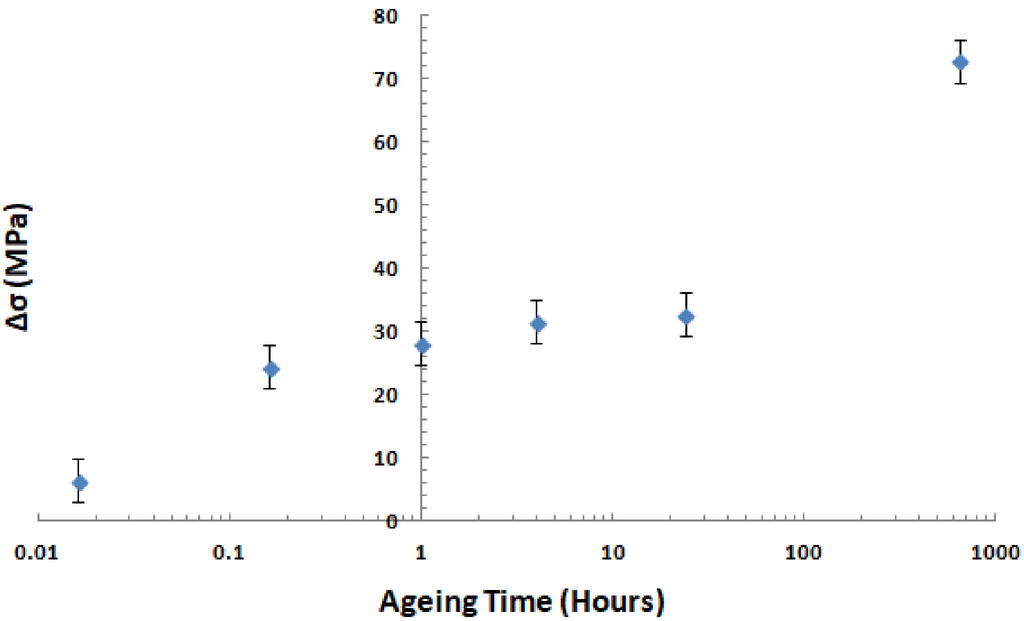

Figure 40: Plot of strengthening due to strain ageing versus ageing time for samples deformed to 2% and aged at room temperature for various times

Compiled strengthening data for samples deformed to 2% strain and aged at room temperature demonstrates a local maximum strength which can be achieved by strain ageing 300M in tension for short and intermediate ageing times. Long ageing times of over 600 hours result in a further increase in stress which must be unrelated to the strengthening provided by the Cottrell mechanism at shorter times. This significant additional strengthening is likely due to significant carbon segregation which can occur over long time periods, and potentially the dissolution of fine carbides made possible by the very long time-scale involved.

This effect can also be seen in Figure 41, as samples aged for longer times experience larger strengthening than samples aged for shorter times at the same level of strain, barring one abnormal result for a sample deformed to 1%.

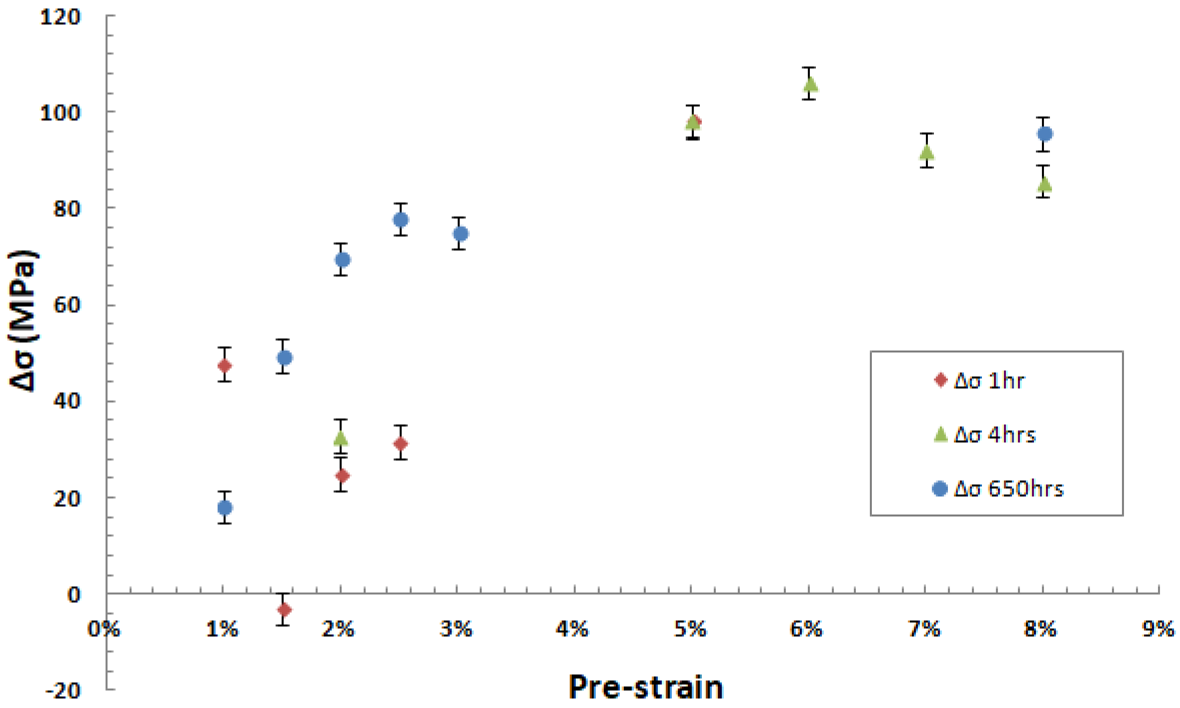

Figure 41: Summary plot of the strengthening of tensile rounds versus pre-strain for various ageing times

As shown above, while strain ageing in the absence of an applied load can induce significant strengthening, there are limits to this increase. The maximum strengthening of just over 100MPa was obtained after pre-straining a specimen to 6% and ageing for 4 hours after unloading. Presumably this could be increased by a further 20-30MPa by ageing at room temperature for over 600 hours, as an additional strengthening mechanism is active after ageing for long times. Shot-peening also produced an increase in strength compared to non shot-peened samples, but this contribution would likely not be additive for samples deformed to large strains, since the reason for strengthening in both cases is the generation and subsequent locking of new dislocations. Shot-peening in conjunction with long-time ageing in samples deformed to relatively low pre-strains could provide additional strengthening, however.

4.2.2.1 Effect of Strain Rate

Strain rate tests were also performed after ageing to determine if the ageing process affected the plastic behaviour upon re-loading to failure. The effects of strain rate on plasticity were initially investigated by deforming round tensile samples to ~2.5% in tension using a cross-speed of 1mm/min, relaxing the load, and then re-loading the specimens to failure at different speeds. The effect of strain rate and ageing on plasticity can be seen below in Figure 42.

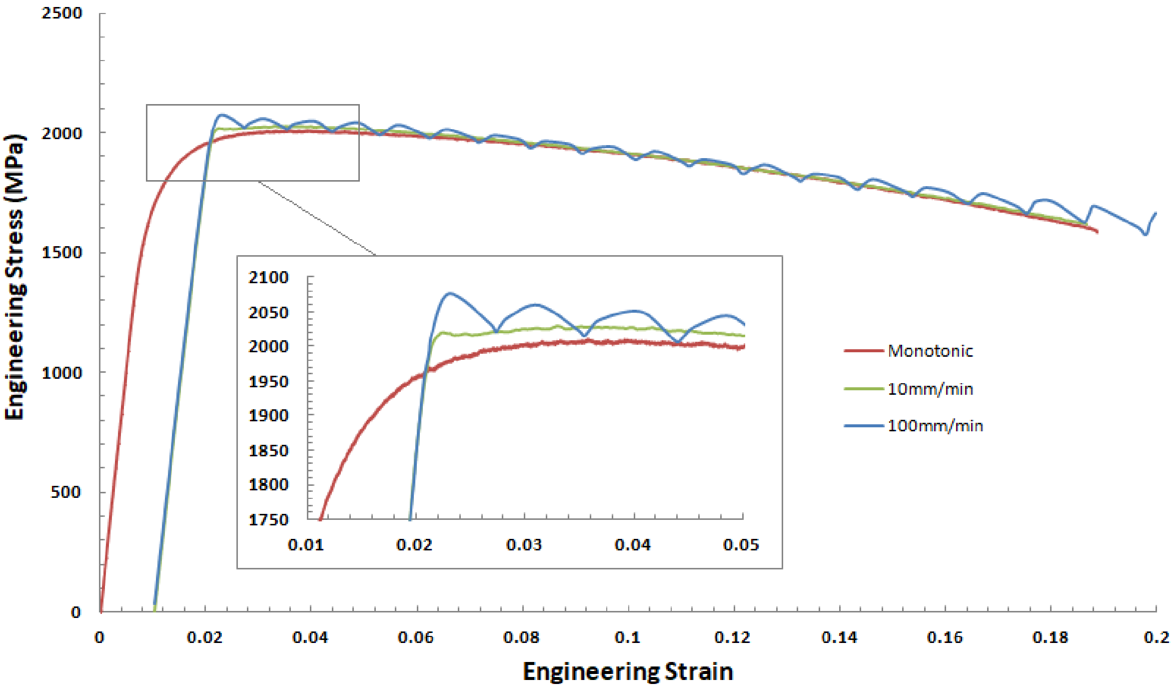

Figure 42: Stress-strain curves for samples deformed to approximately 2.5% at 1mm/min, and rapidly re-loaded to failure at higher rates

Upon examining the data, it is immediately apparent that ageing 300M at room temperature for even brief times appears to have a notable impact on the observed strain rate sensitivity in the material. As shown above, the strain rate sensitivity appears to be positive, in sharp contrast to the results reported after continuous deformation. It should be noted that the samples were aged for a period of several minutes, as releasing the clamps on the equipment and increasing the rate of deformation could not be done instantaneously.

Due to the extremely rapid test times (~2s) for samples deformed at 100mm/min, a relatively low number of data points were collected during the test. In order to correct for the higher rate of deformation, a similar test was performed and the data acquisition rate was increased proportionally to the deformation rate. Additionally, the ageing time was increased to 1 hour for the second test. These results can be seen below in Figure 43.

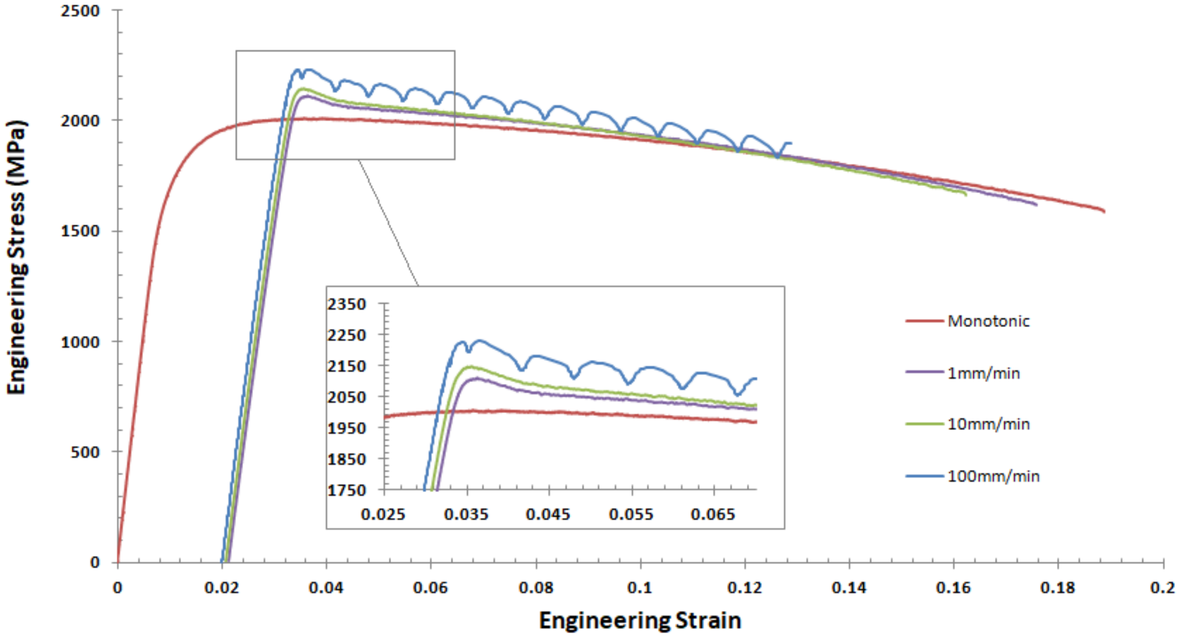

Figure 43: Stress-strain curves for samples deformed to 3% at 1mm/min, aged for 1hr, and re-loaded to failure at varying deformation rates. The re-loading curves are displayed for all tests, and the results are shown alongside a continuous deformation curve at 1mm/min for comparison

It is clear that the positive strain rate sensitivity is once again evident upon re-loading. The effect of ageing time is also notable, as the increase in stress obtained upon re-loading is greater when compared to the short ageing times above.

4.2.2.2 Multiple Deformation and Ageing

Multiple deformation and ageing experiments were also conducted in an effort to better understand the effects of ageing on the plastic behaviour of 300M. These tests involved deforming a tensile specimen to a given initial strain and ageing for 2 hours, before deforming by a further 1% and ageing once more. This process was repeated 3 times for each sample before finally deforming to failure. The results of a sample initially deformed to 5% and then aged as described are available in Figure 44.

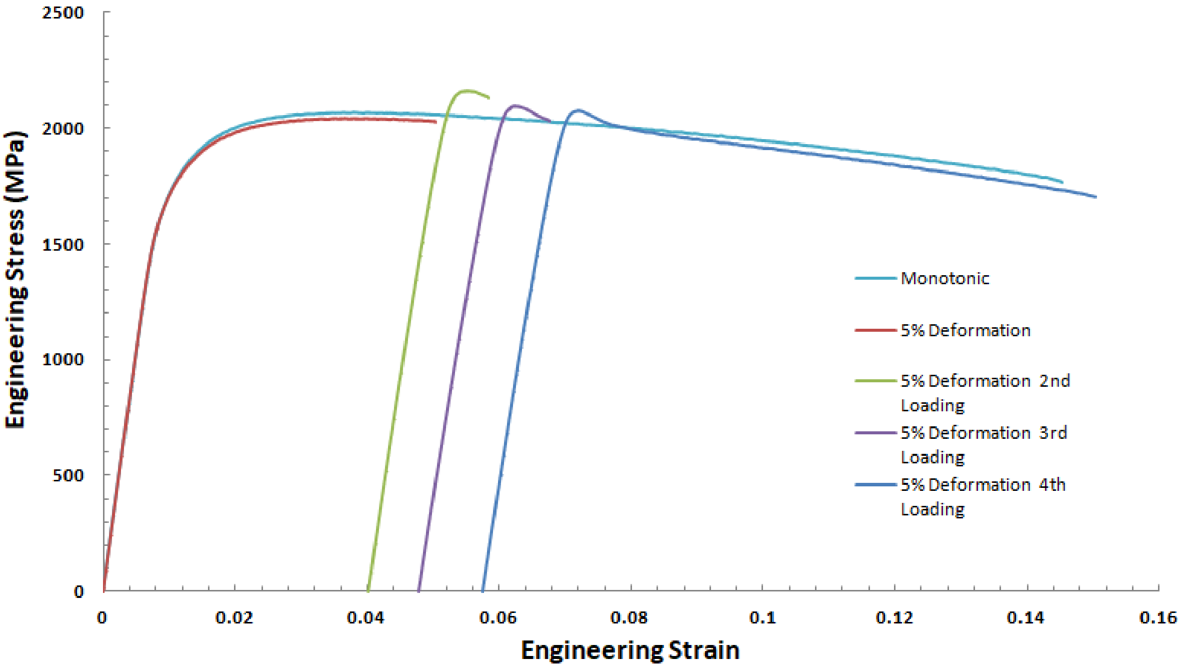

Figure 44: Stress-strain curves resulting from multiple ageing treatments following an initial deformation of 5%. The ageing time for each step was 2 hours and the deformation for the intermediate treatments was 1%

After an initial deformation of 5%, the increase in stress upon re-loading is quite substantial, and diminishes as the ageing treatment is repeated. Another multiple ageing experiment was conducted with a higher initial strain to determine if the initial deformation was responsible for the behaviour observed upon reloading. The stress-strain curves for the sample deformed to an initial strain of 9% are available below in Figure 45.

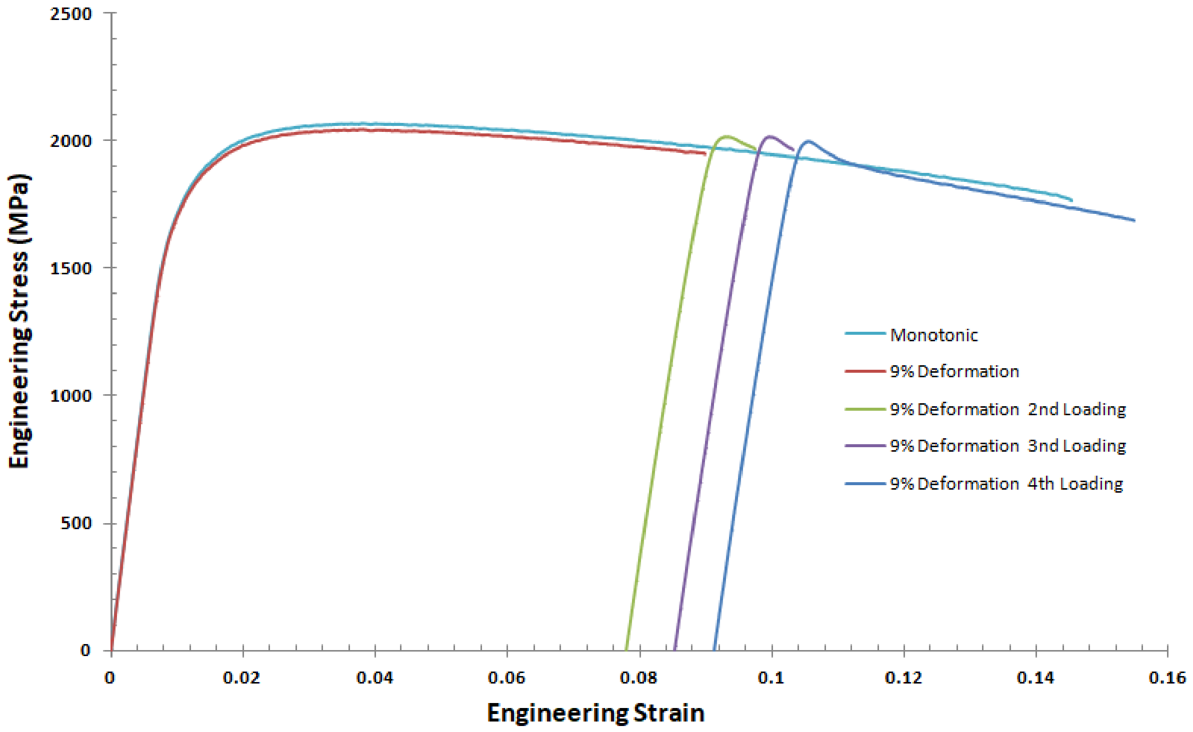

Figure 45: Stress-strain curves resulting from multiple ageing treatments following an initial deformation of 5%. The ageing time for each step was 2 hours and the deformation for the intermediate treatments was 1%

After an initial deformation of 9%, the initial increase in stress upon reloading was significantly lower. Moreover, each increase in stress following the initial deformation was more uniform. A direct comparison of the increases in stress relative to the monotonic behaviour is available for both sets of multiple ageing treatments, and is shown in Figure 46.

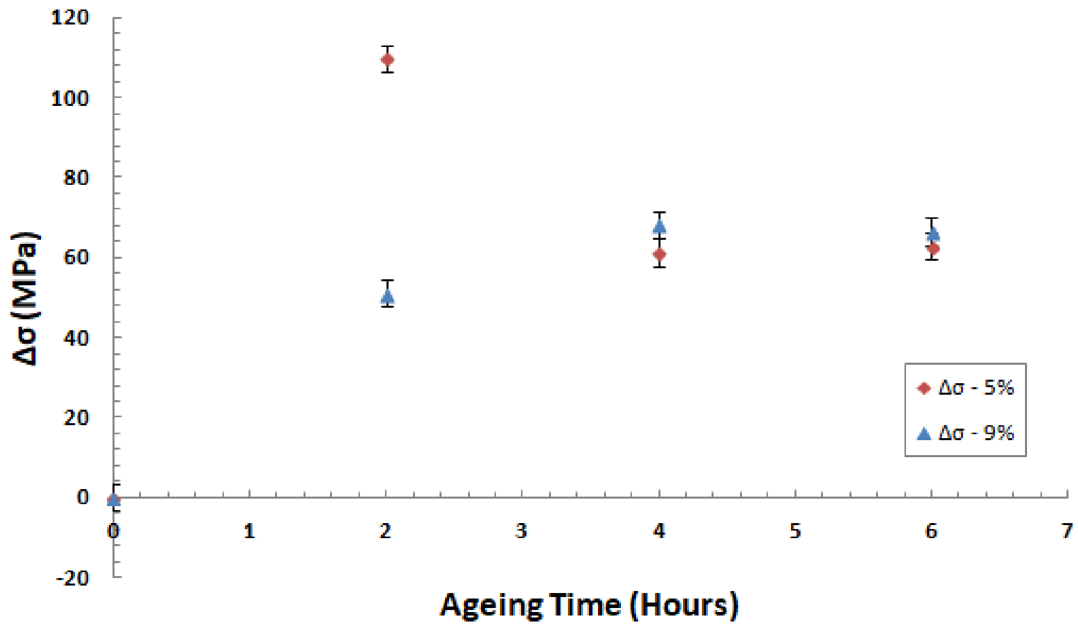

Figure 46: Strengthening behaviour of the multiple deformation and ageing specimens, measured at 0.2% offset compared to the monotonic behaviour at a rate of 1mm/min

Upon examining the results of both samples, the initial strengthening of the sample deformed to 5% appears incongruous with the rest of the experimental data. On the basis of Cottrell dislocation locking, the strength of the material should increase with successive ageing treatments, not increase sharply only to fall with successive ageing. It is notable that the second and third ageing treatments produce similar increases in stress for both samples, as this is in agreement with the idea that there is a maximum value of strengthening which can be achieved through strain ageing, and that this value is significantly influenced by Cottrell locking.

4.2.2.3 Digital Image Correlation

Digital image correlation was performed on selected samples in order to visualize the effects of ageing on plasticity. Each specimen was deformed to an initial strain of 2% at a rate of 1mm/min, unloaded, and subsequently aged for 1 hour at room temperature. Since the strain is not tracked directly during a digital image correlation experiment, samples were instead loaded to approximately 18kN, a load which was expected to produce a strain of 2% after examination of the monotonic digital image correlation experiment performed earlier.

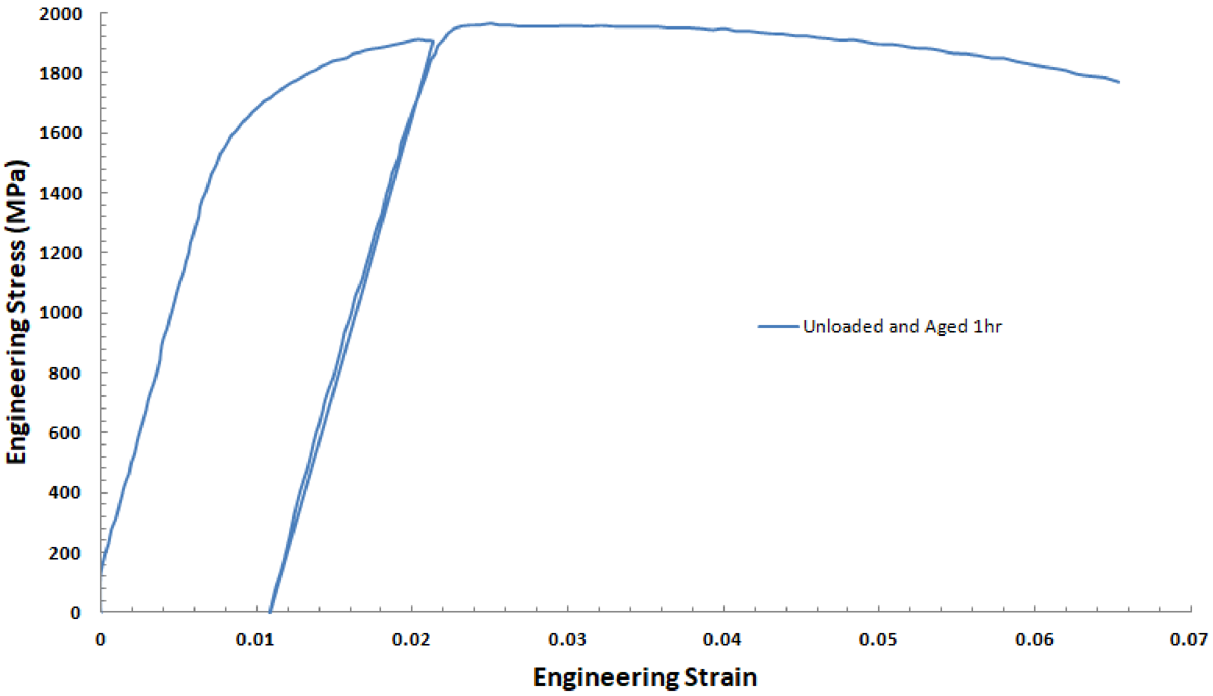

Figure 47: Selected stress-strain curve for a flat sample loaded to 2% strain, unloaded, and aged at room temperature for 1 hr before loading to failure

The increase in stress observed after ageing (~55MPa) was significantly larger in the flat specimens used for DIC than in a round sample aged earlier under similar conditions, which experienced an increase of approximately 30MPa. This difference is almost certainly due to the differences in sample geometry and state of stress between round and flat samples.

Strain maps for unloaded samples revealed the same localized plastic behaviour observed during monotonic testing. The appearance and propagation of deformation bands in aged samples can be observed below in Figure 48.

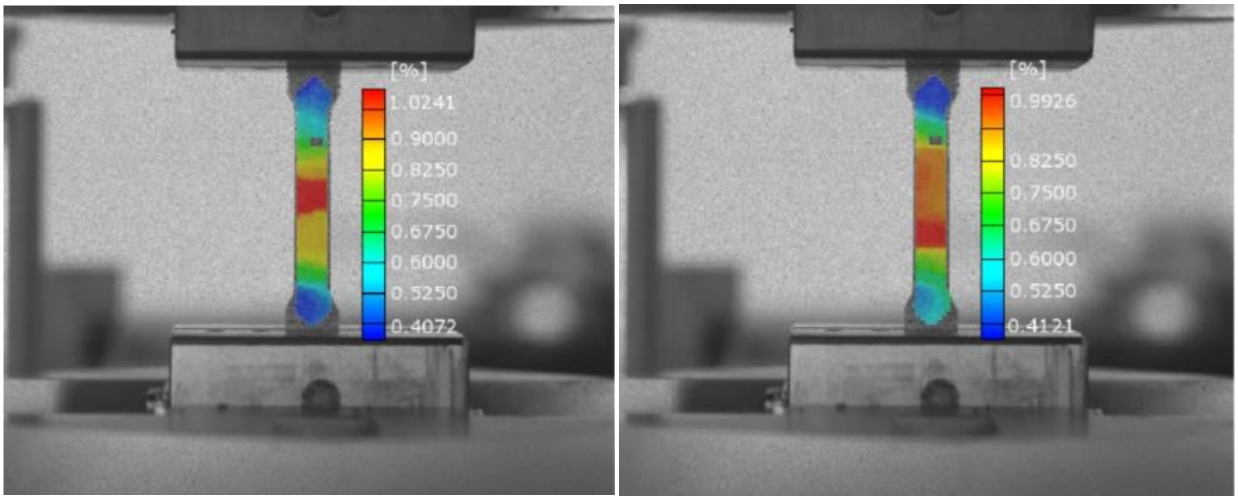

Figure 48: DIC strain maps for a sample deformed to ~2% strain at 1mm/min, unloaded, and aged for 1 hour at room temperature before loading to failure

Analysis of the strengthening occurring after unloading and ageing produced relatively inconsistent results. One unloaded specimen displayed an increase on the order of 57MPa, while the other produced a much larger increase of 96MPa. A third sample was also tested but did not produce usable results. Taken in isolation, unloaded ageing would appear to induce widely varied strengthening. These results are compared with the samples aged under load later in this work for additional context.

4.2.2.4 Ageing and Re-tempering

A number of studies have been conducted on the ageing and tempering of AISI 4340, but fewer studies of the same type exist for 300M [110]. The effect of ageing of 300M at elevated temperature was examined in this work by deforming tensile specimens to 3% strain and tempering them at various temperatures above 200°C. Stress-strain curves resulting from the pre-straining and re-tempering processes are shown in Figure 49.

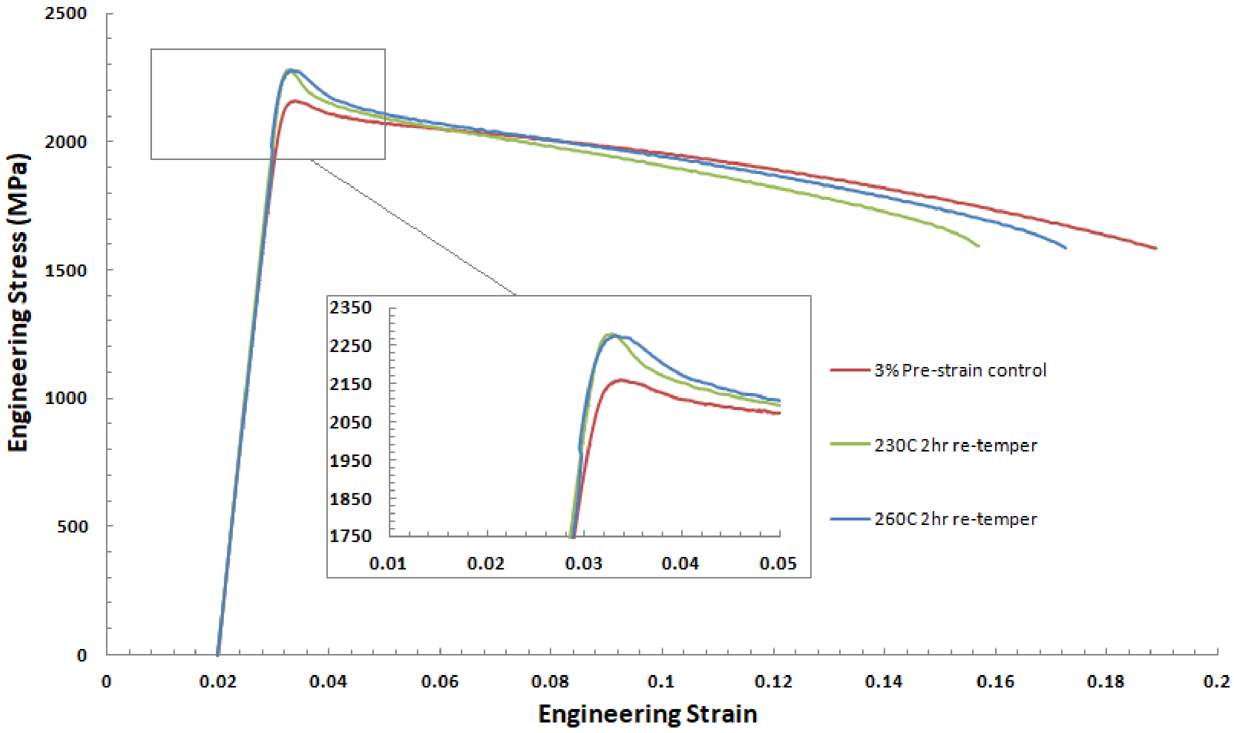

Figure 49: Stress-strain curves for samples deformed to 3%, tempered, and deformed to failure. Results are compared with a sample deformed to 3% at a rate of 1mm/min as a control

As seen above, tempering after deformation significantly increases the strength observed upon reloading, and causes a simultaneous decrease in failure strain. It can also be observed that lower tempering temperatures result in higher strength and lower failure strain. These results are in good agreement with the work of Stephenson and Cohen [110], who studied the effects of pre-straining and re-tempering on AISI 4340. Stephenson and Cohen observed that the carbides in the tempered martensite were dissolved during deformation and re-precipitated by re-tempering, and attested that at least a portion of the observed strengthening was due to this carbon redistribution [110].

4.2.2.4 SEM Fracture Analysis

As before, fracture analysis was conducted using electron microscopy to examine the nature of fracture after strain ageing. All sample geometries were analyzed, including round, flat and modified flat specimens. The effects of ageing time and initial strain were also investigated, and fracture surfaces of aged samples were compared to specimens which were deformed monotonically to failure.

Fracture analysis of the samples aged for short times showed negligible differences when compared to monotonic specimens. All short-time aged samples were also highly ductile and displayed dimples and features on the same length scales. Two such fracture images are shown below in Figure 50.

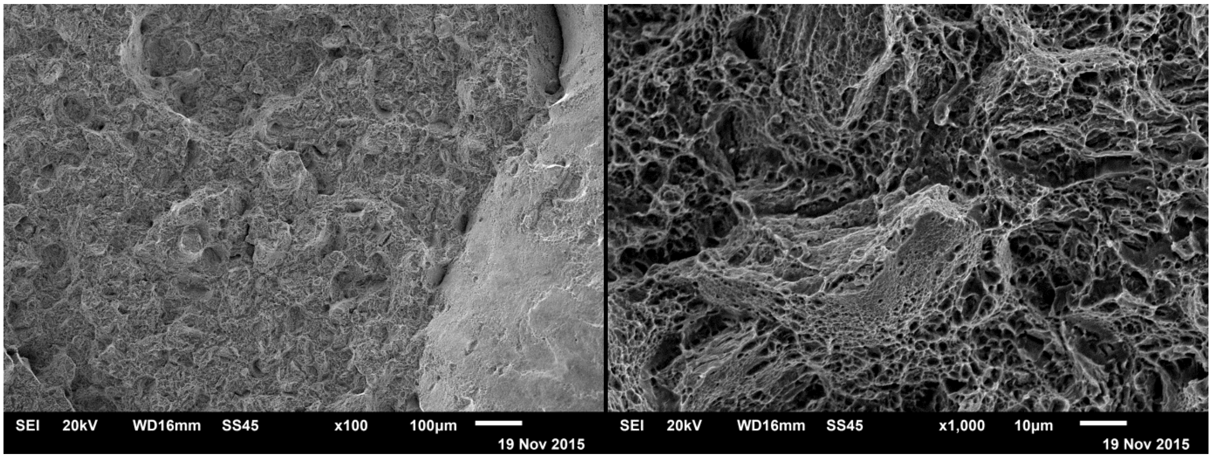

Figure 50: SEM fracture images taken at 100x (left) and 1000x magnification (right) for a sample aged for 1 minute at room temperature

Specimens aged for intermediate times (4-72hours) also displayed fracture surfaces which were nearly identical to samples aged for short times or deformed monotonically. Images of fracture surfaces for samples aged for 4 hours at room temperature are displayed in Figure 51.

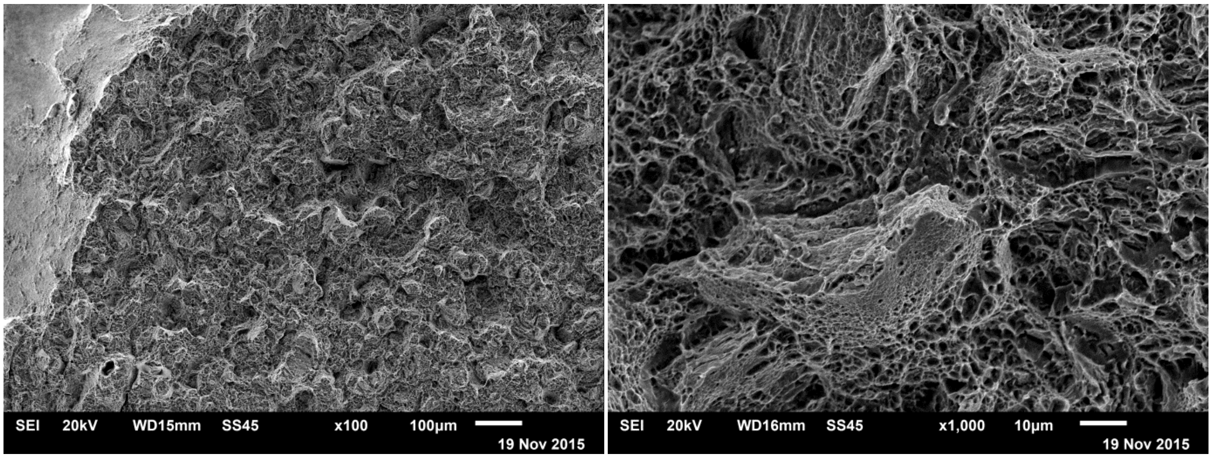

Figure 51: SEM fracture images taken at 100x (left) and 1000x magnification (right) for a sample aged for 4 hours at room temperature

The effect of strain ageing for long times (~650 hours) at room temperature on the fracture behaviour of 300M was also investigated as shown below in Figure 52.

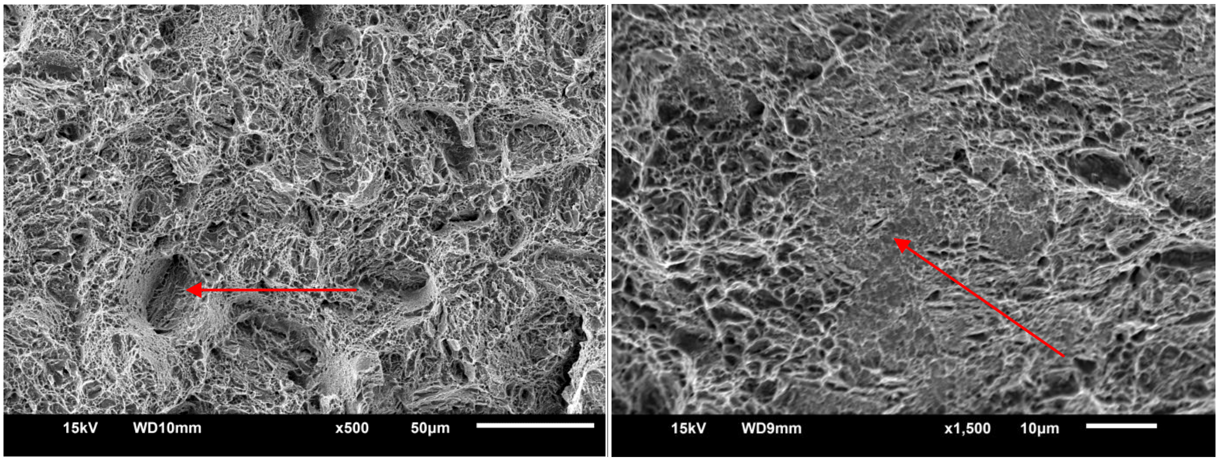

Figure 52: SEM fracture images aged at room temperature for approximately 650 hours before final deformation. The leftmost image was taken from a sample pre-strained to 1.5%, while the rightmost was from a sample initially strained to 1%

At first glance, the fracture surfaces of samples aged for long times appear almost identical to those resulting from previous ageing treatments. A more detailed examination at larger magnifications, however, reveals some features which may be representative of slight changes occurring as a result of ageing. While features similar to the “terraces” or pits observed in monotonic and sample aged for short times were observed, they were slightly different in that their tops or bottoms were not completely perpendicular to the fracture surface. As such, these features bear a more striking resemblance to grain boundaries or perhaps parallel sets of packets. Notably, some evidence of a mixed fracture mode was also detected in samples aged for over 600 hours at room temperature, as evidenced by flat regions on the fracture surface.

Samples which were pre-strained and re-tempered at temperatures exceeding 200°C exhibited similar fracture behaviour to specimens aged at room temperature for long times. Fracture images for re-tempered samples are shown in Figure 53.

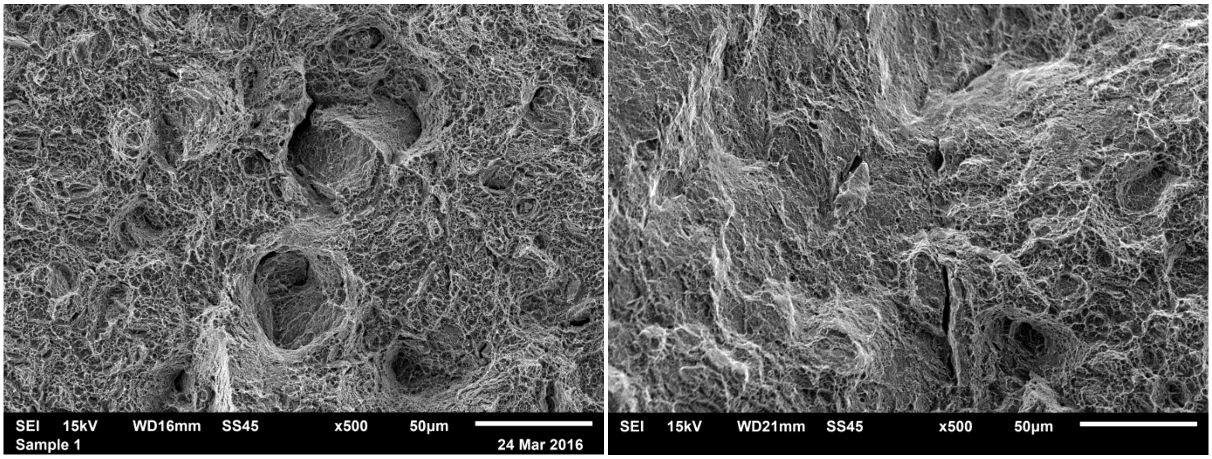

Figure 53: SEM fracture images taken at 500x magnification for samples pre-strained 3%, and re-tempered at 260°C (left) and 204 °C (right)

Like the tensile specimens aged for long times, re-tempered samples also displayed signs of mixed fracture and “terraces” which were oriented at an angle to the fracture surface. The similarities in appearance are likely due to the increased segregation of carbon which occurs at long times or elevated temperatures.

Tensile specimens subjected to large initial strains were also tested and examined using SEM. Fracture images for samples pre-strained to values larger than 6% are available in Figure 54.

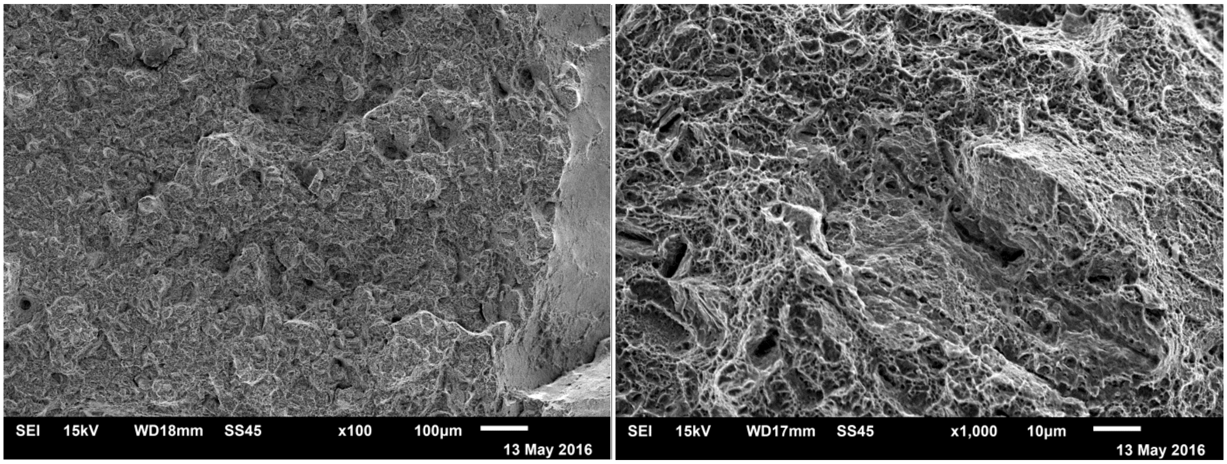

Figure 54: SEM fracture images taken at 100 and 1000x magnification for samples pre-strained 6% (left) and 7% (right) subsequently aged at room temperature for 4 hours

As shown above, the influence of initial deformation on the fracture behaviour of 300M appears to be relatively small, as no significant differences were observed in terms of ductility when comparing the fracture surfaces of samples which experienced differences in pre-strain.

The fracture surfaces of flat samples were also investigated using SEM. Examples of images taken for a flat sample aged under load for 1 hour at room temperature are available in Figure 55.

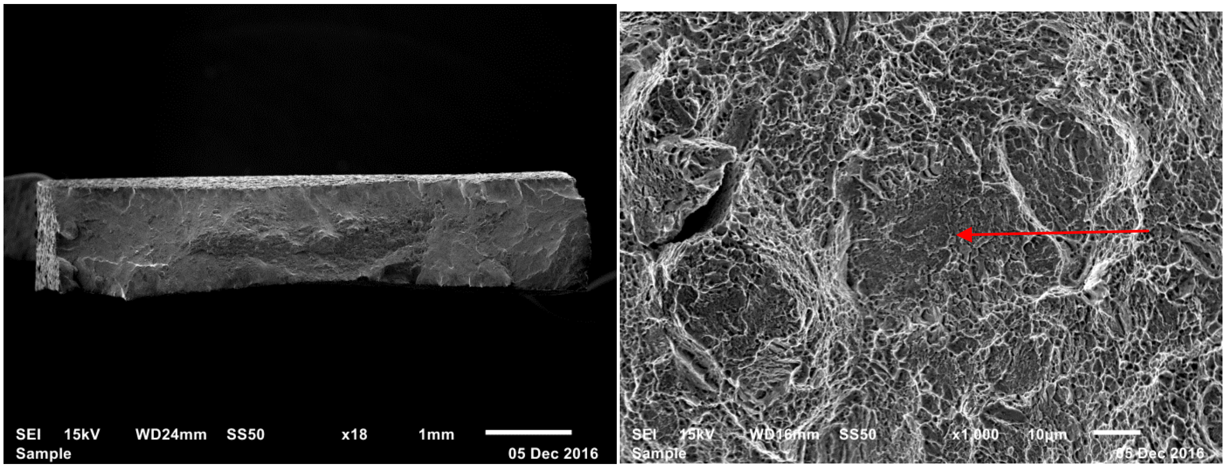

Figure 55: SEM fracture images of a flat sample aged under load for 1 hour following an initial deformation to approximately 2%

At low magnifications, the fracture of these specimens was identical to the bulk of the tensile rounds examined earlier, in that the fracture appeared to be completely ductile. At higher magnifications, however, small flat regions indicated that a mixed fracture mode was in effect, at least on the micro scale. This change in behaviour may be due to the different sample geometry, as this change was observed in all specimens, including those deformed monotonically without ageing.

Regardless of sample geometry or ageing treatment, a large number of specimens displayed prominent evidence of significant void linkage on the failure surfaces. These regions consisted of lines of dimples which could be identified at high magnification. One such example of void linkage is shown below in Figure 56.

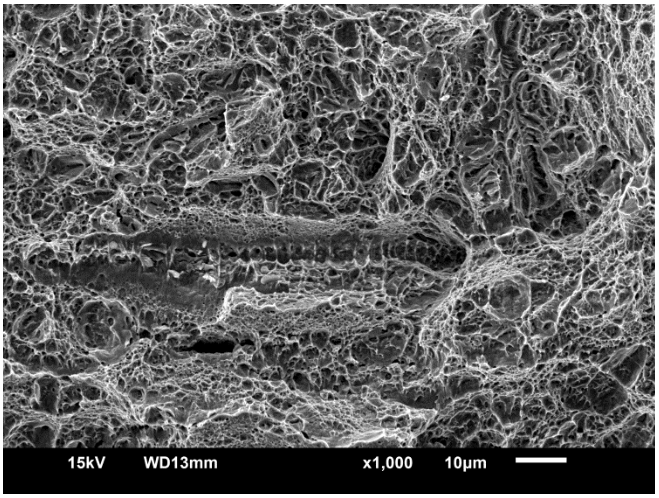

Figure 56: SEM fracture image showing prominent void linkage, taken from a sample deformed to 2% strain and aged for 650 hours at room temperature

4.2.2.5 INCA Feature Inclusion Analysis

In order to examine the effect of inclusion size and density on the fracture of 300M, a sample with an abnormally large inclusion population was deliberately obtained and examined. Inclusion analysis was performed on this specimen using SEM and INCA feature software. These results were compared to a section from a tensile specimen that exhibited typical behaviour, and a bulk industrial sample. A summary of the total detected inclusion populations for each sample is shown below in Table 9.

Inclusion Type	Abnormal Material Count	Tensile Section Count	Industrial Bulk Count
MnS	11	10	0
Alumina	67	8	2
Ca	4	2	3
Ti	38	16	8
Mn + Si	507	41	66
TOTAL	**627**	**77**	**79**

Table 9: Summary of features classified as inclusions for the 3 samples examined using INCA Feature

It is immediately apparent that the inclusion population in the abnormal material was almost an order of magnitude larger than in the "normal" material. Additionally, inclusions with diameters above 10µm and inclusion clusters were detected more frequently in the abnormal sample. The large difference in detected inclusion populations is likely responsible for the significant reduction in ductility observed in the brittle specimen, as the spacing between inclusions was approximately 3 times smaller than in the regular material. This lower spacing represents a greatly increased percentage of potential crack initiation sites, and also affects the growth and propagation of voids. It is also possible that the inclusion population in the abnormal material is larger than what was observed, as the reliable detection of inclusions smaller than ~2µm is difficult. Regardless, it is clear that larger inclusion populations and a larger inclusion size result in a transition towards mixed-mode and brittle fracture in 300M. An SEM image of the brittle behaviour in the abnormal specimen is shown in Figure 57.

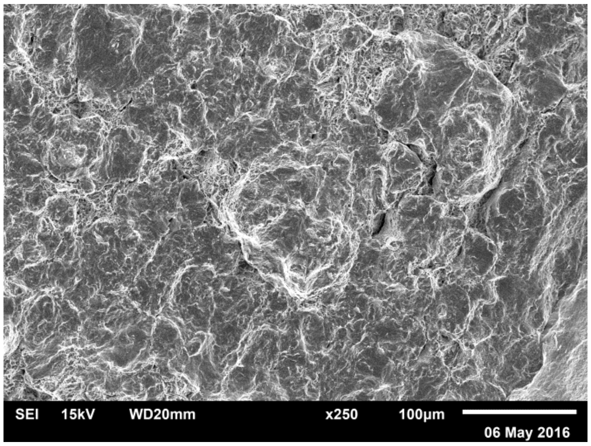

Figure 57: SEM fracture image at 250x magnification of the material with an abnormally high inclusion population

4.2.3 Ageing under Load

Tensile testing was also performed for samples held under load during the ageing process to determine if applied stress affected the ageing behaviour of 300M.

4.2.3.1 Digital Image Correlation

The digital image correlation tests for samples which were aged under load were performed under the same conditions as the unloaded tests, except the applied load was not released during ageing. As such, samples held under load experienced significant stress relaxation during the time they were aged. A selected stress-strain curve for a sample aged under load is shown below in Figure 58. The load applied during ageing was recorded by the tensile frame.

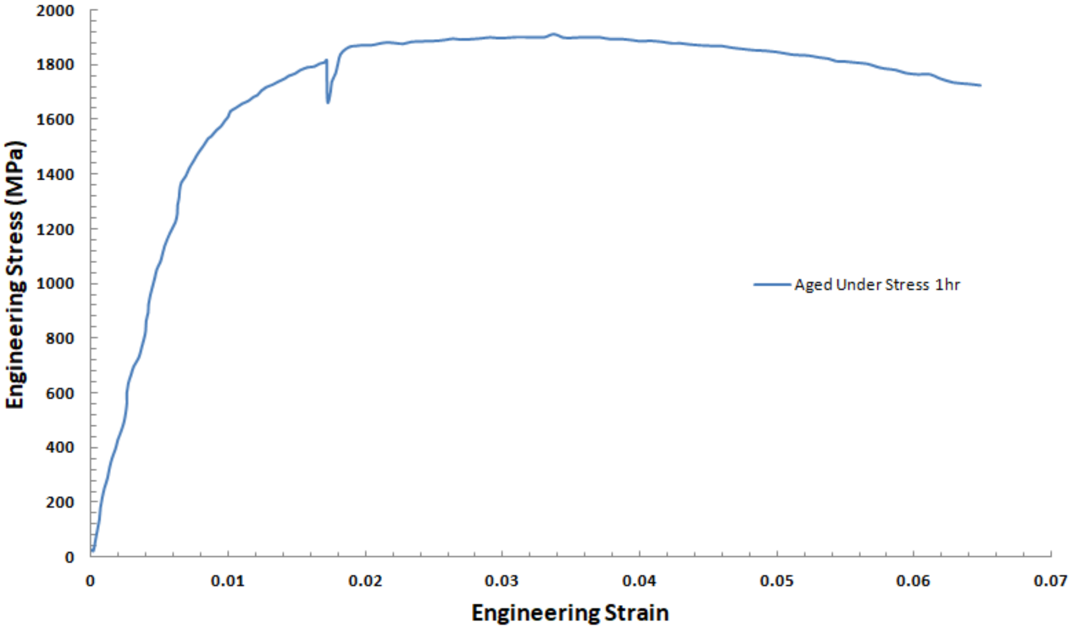

Figure 58: Selected stress-strain curve for a flat sample loaded to 2% and aged under load at room temperature for 1 hr before loading to failure

Samples aged under load behaved similarly to samples unloaded during ageing, save for the stress relaxation which took place. Both types of ageing treatment resulted in similar increases in stress upon re-loading, with a magnitude of approximately 60MPa. A summary of the strengthening experienced by flat samples of both thick and thin geometries is available in Table 10.

Geometry	Pre-strain	Ageing Conditions	Ageing Time	Δσ (MPa)
Flat	~2%	Unloaded	1 hour	58
Flat	~2%	Unloaded	1 hour	96
Flat	~2%	Under Stress	1 hour	58
Flat	~2%	Under Stress	1 hour	62
Flat	~2%	Under Stress	1 hour	56
Thick Flat	~2%	Under Stress	1 hour	64

Table 10: Strengthening summary table for all flat specimens tested using DIC

Strain maps were also produced for samples aged under load, and once again revealed propagation of bands of localized plasticity as shown in Figure 59.

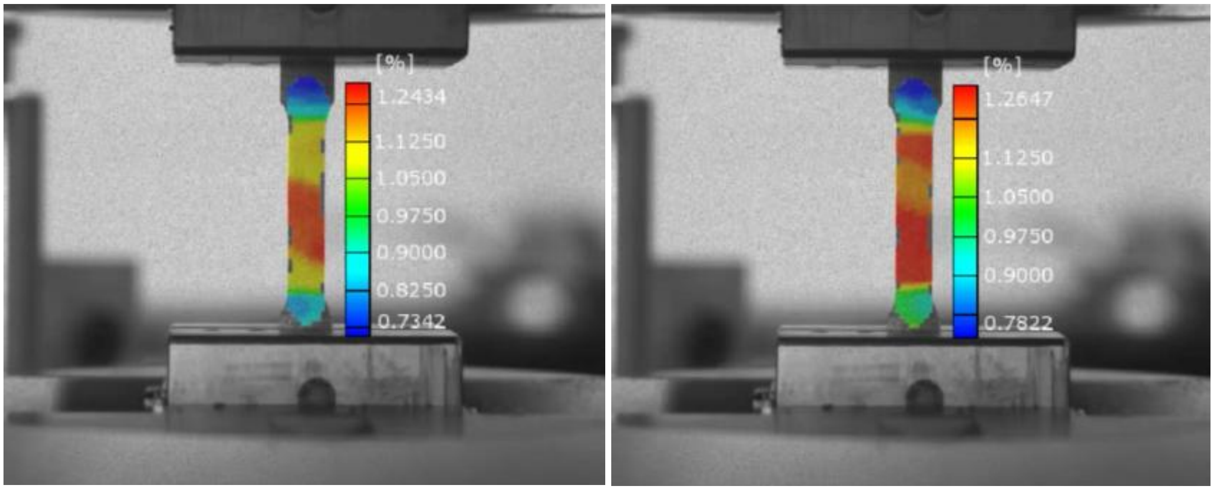

Figure 59: DIC strain maps for a sample deformed to ~2% strain at 1mm/min and aged under load for 1 hour at room temperature before loading to failure

As seen above, the propagation of bands of localized plastic deformation occurs with the same regularity in samples aged under load as specimens that were deformed monotonically or aged without an applied load. Based on the low number of samples tested however, no definite conclusions can be drawn about the behaviour of the deformation bands.

Samples with a larger thickness were also prepared to further investigate the localized plasticity present in 300M. These specimens were examined sideways to attempt to image the bands in the thickness direction. One sample with a larger thickness was loaded monotonically to failure as shown in Figure 60.

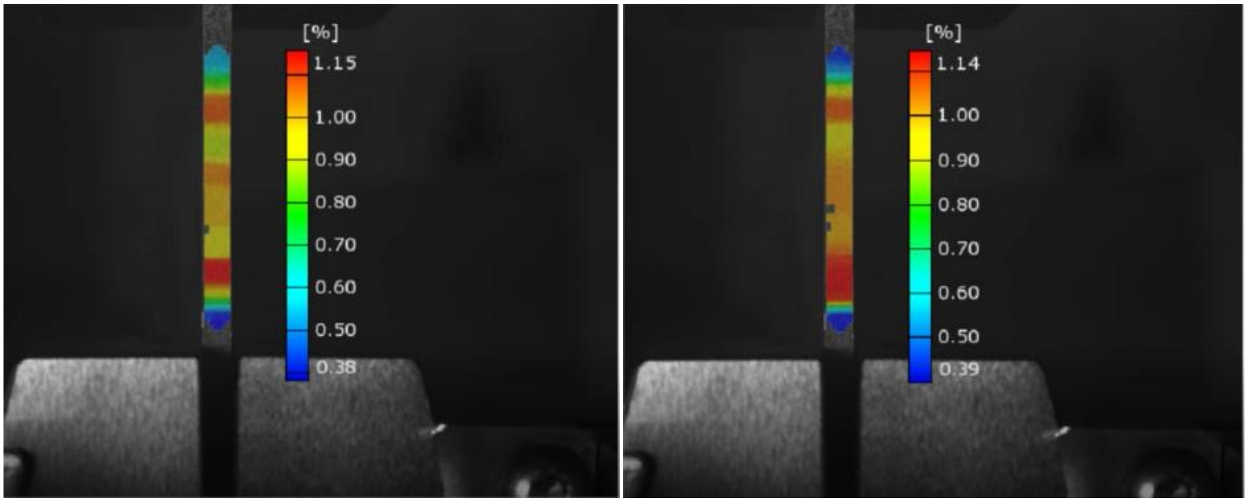

Figure 60: DIC strain maps for a thick flat sample deformed monotonically to failure at 1mm/min

The formation and propagation of bands of localized plasticity were once again observed. No differences in behaviour were identified between flat samples examined from the front and the specimen examined from the side. In both cases, the bands propagated in a direction paralell to the pulling direction, with no changes in band size or angle.

The effect of ageing on the localized plastic behaviour was investigated by deforming a thick flat sample to approximately 2% strain and ageing under load for one hour at room temperature. Once again, the strain was approximated using the monotonic loading curve for the thicker flat geometry as shown above. The strain maps for the aged sample are shown below in Figure 61.

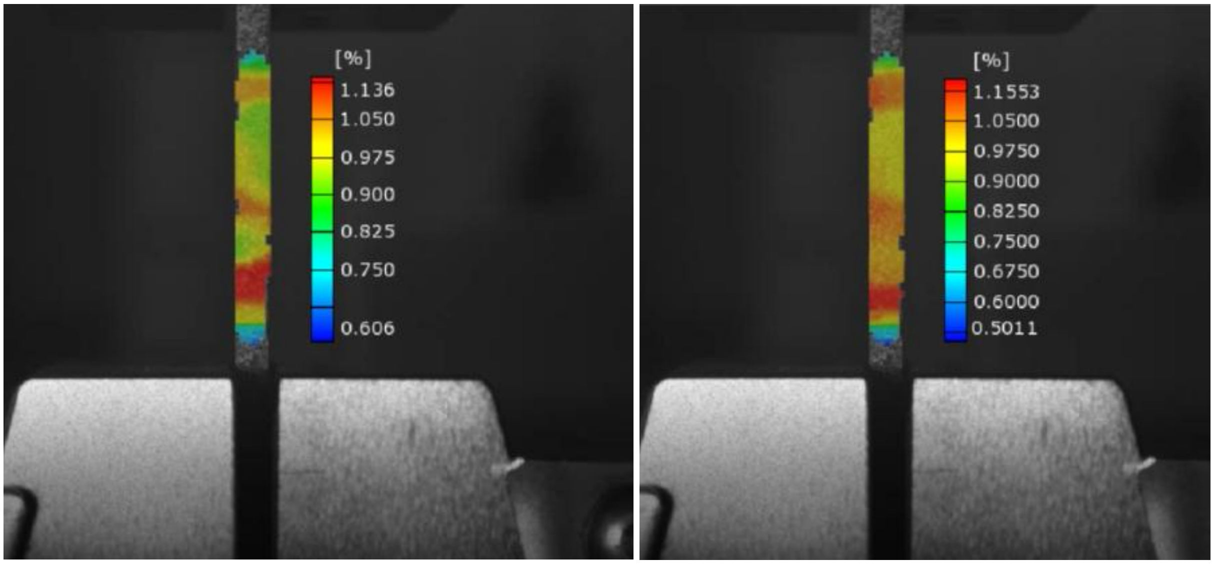

Figure 61: DIC strain maps for a thick flat sample loaded to 36kN (~2% strain), and aged under load for one hour at room temperature

Once again, the presence of deformation bands which form and propagate parallel to the pulling direction is evident. No significant differences were detected between samples which were aged under load and specimens which were unloaded during ageing. The low number of samples tested with the thicker flat geometry makes drawing a conclusion about the effect of ageing on localized plasticity difficult without additional context however.

Chapter 5 – Discussion

This chapter describes the results obtained experimentally and endeavors to describe the observed properties in terms of the fundamental behaviour of solute atoms and dislocations. The first section outlines the behaviour of 300M when deformed monotonically, and the following section describes the dynamic ageing effects which occur in the material at room temperature for a given strain rate range. The third segment outlines the mechanism responsible for static ageing, and the fourth section summarizes and models the strengthening effect using fundamental dislocation evolution equations. The final portion is concerned with the failure of 300M, and provides a potential explanation for the observed fracture behaviour.

5.1 Monotonic Deformation

The monotonic deformation behaviour of 300M at room temperature has been extensively studied at a variety of strain rates. This section summarizes the salient features of the mechanical response of the studied material when deformed monotonically to failure.

All studied material exhibited consistent yielding at a stress of ~1550MPa, with a Young's modulus of 201GPa. Comparison of the ultimate strengths of material from different heats revealed a variation of approximately 75MPa, although the work hardening behaviour was consistent. The rounded nature of the yielding and serrations on the stress-strain curves shown experimentally exemplifies a strong initial work hardening rate and a lengthy elasto-plastic transition which was explained in terms of microstructural heterogeneity by Allain *et al* [86]. This theory could also explain the highly rounded peaks of the stress-strain curves which exhibit dynamic ageing. If the microstructure of the material yields at different stress levels, then the breakaway of dislocations from solute atoms that dominates dynamic ageing behaviour would not occur simultaneously, resulting in the characteristic rounded shape. Internal stresses could also explain the extended elasto-plastic transition observed in this work, but Snyder observed that the internal stresses present after quenching were largely relaxed after tempering for 1 hour [84].

In addition to high strength, all 300M samples tested in this work displayed significant elongation to failure, with most specimens exhibiting a failure strain of 15-20%. SEM analysis of failed tensile specimens confirmed significant dimpling characteristic of ductile failure. Reduction in area measurements were also conducted for all samples, and identified an average value of 40% reduction in area at failure.

5.1.1 Strain Rate Sensitivity

Monotonic tensile testing conducted at strain rates ranging from 0.00133-0.133s^{-1} identified apparent negative strain rate sensitivity in 300M at room temperature. This result is somewhat at odds with the work of other authors, as Leslie and Sober observed a transition to positive strain rate sensitivity for 43xx steels containing 0.1-0.3wt% C at room temperature for strain rates greater 0.01s^{-1} [30]. In this work, this transition was not observed, as negative sensitivity persisted to strain rates of at least $0.1s^{-1}$. It is important to note that in the case of the 0.4 wt% C steel the authors reported a null sensitivity at room temperature, but noted that the scatter in the data was much greater [30]. It is then possible that the 0.4% steel could have displayed negative strain rate sensitivity at room temperature, but the effect was masked.

Dynamic ageing effects were also observed during testing at room temperature, particularly in samples deformed at strain rates of $0.133s^{-1}$ and above. Significant dynamic ageing persisted to a rate of at least $0.266s^{-1}$, but disappeared at rates higher than ~$0.4s^{-1}$. Dynamic ageing effects were also observed at much lower strain rates ($0.00133\text{-}0.0133s^{-1}$) using digital image correlation with an image capture rate of 10 frames per second. The presence of dynamic strain ageing at room temperature is notable, as serrated flow is not often observed at room temperature in martensite [51]. Authors such as Leslie and Sober attribute this absence to carbon redistribution occurring during tempering and the presence of internal stresses in the case of as-quenched martensite [30]. Krauss has suggested however that the high carbon content (0.4 wt %) in 4340 steels could produce dynamic strain ageing at room temperature [46].

5.2 Dynamic Strain Ageing

Also known as the Portevin-Le Chatelier effect, dynamic strain ageing is governed by solute-dislocation interactions. In essence, dynamic ageing is due to mobile dislocations being “locked” by solute atoms, and can be explained fairly generally. For any given strain rate, dislocations must either be waiting at an obstacle or moving toward a new obstacle, where the waiting time depends on dislocation density and strain rate, and the diffusion time is a function of temperature and dislocation density [113]. This explanation can be used to explain negative strain rate sensitivity, since longer waiting times result in a larger number of solute atoms segregating to a dislocation, and a higher stress required to move a dislocation at a given velocity [113]. This idea is valid if both characteristic times are of the same order. If one characteristic time is significantly different than the other, the result is positive strain rate sensitivity.

In this work, dynamic ageing was observed physically as the propagation of localized bands of plastic deformation in the strain maps of samples deformed monotonically and those aged at room temperature using digital image correlation. The wave-like propagation of bands was also observed using section line strain plots of tensile specimens in the pulling direction.

While the propagation of the bands has been clearly identified, the type(s) of bands present in 300M are still not entirely clear. The determination of the exact nature of the types of bands present in 300M is an involved process, and is not performed in this work. It is well-known for example that multiple types of bands may exist simultaneously and/or interact with one another in complex ways. This problem is exacerbated by the highly complex microstructure of martensite, which is strongly heterogeneous. Examination of a magnified stress strain curve (Figure 62) from a sample tested at a strain rate of 0.00133s^{-1} reveals the complex flow stress present in 300M acquired using a data acquisition rate of 100 points per second.

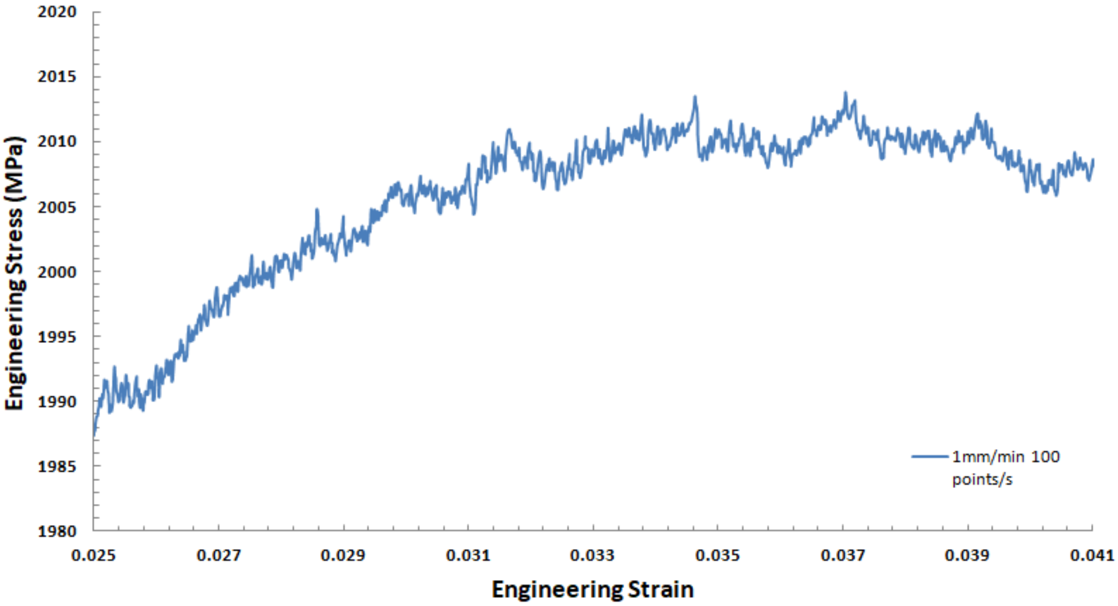

Figure 62: Magnified stress-strain curve for a sample deformed monotonically using a crosshead speed of 1mm/min and a data acquisition rate of 100 points per second

In summary, analysis of dynamic effects in 300M has confirmed the existence of the Portevin-Le Chatelier effect for strain rates ranging from 0.00133-0.266s^{-1}. The effect almost certainly exists at strain rates higher than $0.266s^{-1}$ as well, but no strain rates between 0.266-$0.399s^{-1}$ were tested in this work. It is significant that no dynamic ageing was observed at $0.399s^{-1}$, as DSA is known to be present within a given range of strain rate and temperature. As such, its absence at high strain rates reinforces the fact that it is indeed present at lower rates. Additional tests at intermediate rates could identify the exact range in which dynamic ageing occurs at room temperature in 300M, and could also shed light on the strain rate sensitivity at the same temperature.

5.2.1 Effect of Prior Deformation on Dynamic Ageing

Investigation into the effect of static ageing on DSA or the Portevin-Le Chatelier effect was conducted using flat and round samples by deforming them to approximately 2.5% and ageing at room temperature for one hour before observing them. While differences in dynamic behaviour would be expected due to the changes in mobile dislocation densities caused by ageing, no significant differences were observed in the propagation of bands at strain rates on the order of $0.00133s^{-1}$. Bands of localized deformation propagated in a similar manner both before and after ageing, with no discernible differences in band width, propagation speed, or the timing or frequency of their appearance. While no quantifiable differences were observed for low strain rates, any effects of static ageing would likely be more easily identifiable for strain rates between 0.133-$0.266s^{-1}$, where the effects of dynamic ageing were most pronounced. Material limitations and machining time precluded this investigation in this work, but forthcoming studies will address this topic.

5.3 Static Strain Ageing

During deformation, dynamic effects play a large role in defining the mechanical behaviour of interstitial alloys as shown above. Static ageing also has a significant influence on the mechanical properties of a material, regardless of the presence of dynamic effects during deformation. Static ageing effects such as those seen in this work are also a result of solute-dislocation interactions, and were first described by Cottrell [55]. This section duplicates the calculations performed by Cottrell and Bilby [70], and uses them in conjunction with Cottrell-

Louat [114] [115] ageing kinetics to generally describe the strain-ageing behaviour observed in this work.

5.3.1 Cottrell Locking Calculations

Cottrell and Bilby [70] were the first to develop an expression for the locking of dislocations by mobile solute atoms. Their expression, shown below in Equation 3, describes the probability of atmosphere formation for ageing times that are not excessively short.

$$N(t)/_{N_s} = n_0\lambda 3\left(\frac{\pi}{2}\right)^{\frac{1}{3}}(\frac{ADt}{kT})^{2/3} \qquad [3]$$

In the above expression, N(t) represents the number of solute atoms which arrive to form an atmosphere in a given time t, N_s is the number of carbon atoms per unit length of a given dislocation required to form an atmosphere consisting of one carbon atom on each atomic plane, and A is an interaction parameter describing stress. The average concentration of solute expressed as atoms per unit volume is represented by n_0, the planar spacing is given by λ, diffusion coefficient by D, temperature by T, and the Boltzmann constant by k.

In order to utilize the Cottrell locking expression to determine an approximate locking time for 300M, the original calculations performed by Cottrell and Bilby for an ambient temperature of 293K were duplicated to ensure the accuracy of subsequent calculations. A comparison between the calculated results and those generated by Cottrell and Bilby for α-Fe are shown in Figure 63.

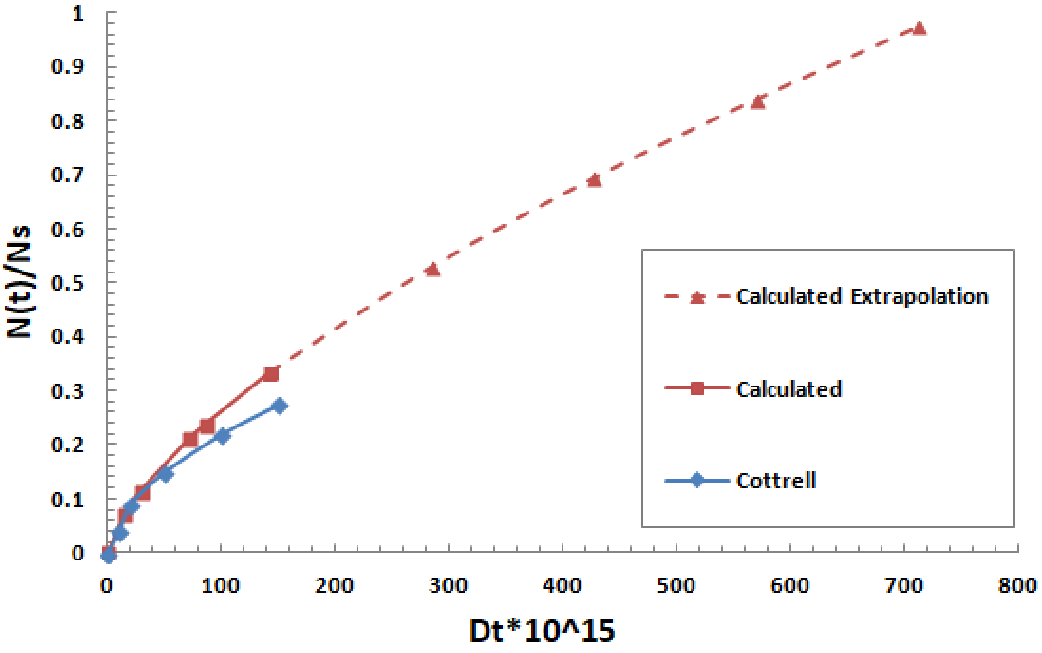

Figure 63: Comparison of dislocation locking probability data for a positive edge dislocation in α-iron

As shown above, the repeated calculations show relatively good agreement with the original results of Cottrell and Bilby, although the duplicated model predicts a marginally higher fraction of locking in the later stages. While these calculations cannot identify an exact time required for complete locking, a reasonable estimation can be made by extrapolation of the data. It should be noted that the range of the calculations performed by Cottrell and Bilby was deliberately limited, since outside of the given range Cottrell and Bilby determined that their model would prematurely predict locking. Extrapolating the data to predict complete locking then results in a wide range of potential characteristic locking times.

Due to the promising results of the original calculations, the expression for locking was applied to 300M. As such, all parameters were re-calculated using the original method of derivation in the work of Cottrell and Bilby. It is important to note that these calculations are based on a dilute solution, and a value of 0.045at% C was used to simulate 300M based on atom probe measurements made by Badinier on 300M [22]. Other conditions for accurate results were described by Cottrell and Bilby, who stated that the validity of their method depended on the value of Dt being greater than 10^{-15}cm^2. With these important considerations in mind, the estimated time required to lock a dislocation via atmosphere formation in 300M was calculated to be approximately 500 seconds, as shown in Figure 64.

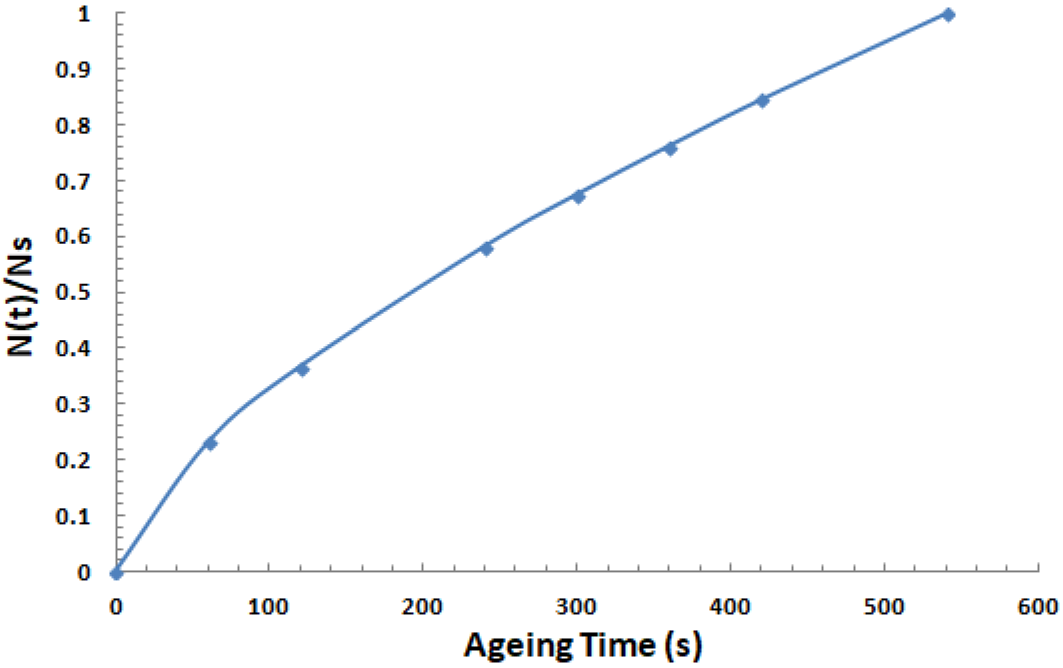

Figure 64: Estimated locking time for a positive edge dislocation in 300M, calculated using the Cottrell-Bilby method **[70]**

An estimated locking time on the order of 500-600 seconds agrees well with experimental ageing results, which demonstrated that a maximum increase in stress upon re-loading was achieved in 1 hour or less, with the exception of very long ageing times (650 hours). This is in spite of the fact that such a calculated time should prematurely predict dislocation locking as discussed above. It should be mentioned that the calculations for dislocation locking described by Cottrell are strongly dependent on the available solute concentration and diffusion coefficient of carbon, neither of which are known with certainty for the case of martensitic 300M. However, the aim of the above calculations was not to determine an exact time required for locking, but rather to demonstrate that locking occurs in a reasonable timeframe which corresponds roughly to the ageing behaviour observed experimentally.

5.3.2 Cottrell-Louat Segregation Kinetics

A number of authors have examined and modified the Cottrell model in order to better represent dislocation locking. Lai *et al* [114] utilized an expression for expressing the increase in stress observed upon re-loading in terms of the ageing time t, the characteristic locking time t^*, and the observed maximum increase in stress $\Delta\sigma_{max}$ based on segregation kinetics proposed by Louat [115]. The expression for locking is shown in Equation 4.

$$\Delta\sigma = \Delta\sigma_{max}(1 - \exp\left[-\left(\frac{t}{t^*}\right)^{\frac{2}{3}}\right]) \qquad [4]$$

The above equation was used to fit experimental ageing data for samples which were deformed, unloaded, and aged at room temperature as shown in Figure 65. A characteristic locking time of 600s was used based on the Cottrell-Bilby calculations above, and that the fact that the model was stated to over-predict locking.

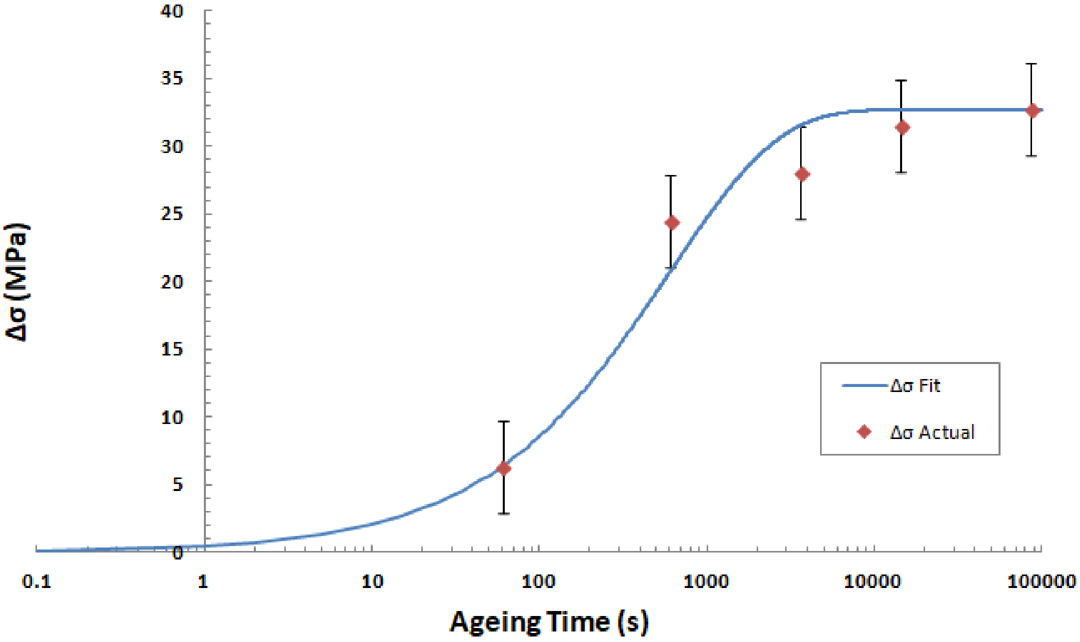

Figure 65: Modified Cottrell-Louat segregation kinetics proposed by Lai *et* al plotted alongside experimental strain-ageing data

As shown above, both the Cottrell model and the modified Cottrell-Louat model used by Lai *et al* strongly suggest that the dominant mechanism for strengthening following strain ageing is the formation of Cottrell atmospheres at previously mobile dislocations. While dislocation locking is likely not the only mechanism responsible for the strengthening of 300M at short and intermediate times, it certainly has the greatest effect.

5.3.3 Additional/Alternative Contributions to Strengthening

Haasen and Kelly [105], among others, have demonstrated that small yield point elongations and transient stress increases occur in pure materials and at low temperatures where dislocation locking is impossible. Haasen and Kelly explain that this behaviour is due to the rearrangement of dislocations which occurs upon unloading the material. While this effect may be present in 300M, it cannot adequately explain or completely predict the strain ageing behaviour observed in this work.

The most obvious reason that the Haasen-Kelly effect cannot be responsible for the ageing behaviour of 300M is that the maximum stress increase observed during their work was approximately 3MPa, compared to increases of over 30MPa observed above. Haasen and Kelly also noted that there was no dependence of the increase in stress on time for times ranging from 1 minute to several hours. The results in this work however have clearly illustrated that a dependence of stress on time exists, and can be explained using Cottrell-Louat segregation kinetics. Finally, Haasen and Kelly noted that the effect observed in their work was only present if samples were aged under a reduced load, while unloaded ageing shown above demonstrate that an applied load is not required to generate an increase in stress upon re-loading.

Other mechanisms may also be partially responsible for some of the strengthening observed after ageing. Snoek ordering for example is likely responsible for the small initial increase in strength observed after ageing for very short times such as one minute, as this effect has been noted to take place in seconds at room temperature [100]. The mechanism for the strengthening observed after long time ageing is not examined in detail in this work, but the strain tempering explanation discussed by Cohen provides a reasonable explanation [96]. Citing the work of MacDonald [116], Cohen describes the dissolution of transition carbides in deformed martensite after re-tempering at 200°C. Cohen found that all of the transition carbides present in a 0.45 wt% C steel were dissolved by this process, and explained that this was due to the introduction of low energy interstitial sites introduced by prior deformation [96]. Kalish and Cohen investigated strain tempering over a wider range of conditions, and found that the large increase in stress after strain tempering was due to the segregation of carbon atoms to the newly formed mobile dislocations [8]. They also noted a contribution due to stress induced ordering. The process of carbide dissolution via strain tempering described by Kalish and Cohen is shown in Figure 66.

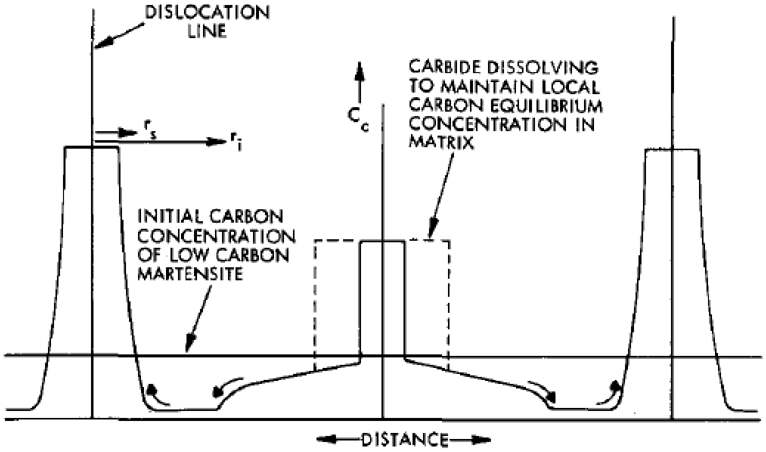

Figure 66: Diagram illustrating the dissolution of transition carbides due to carbon gradients induced by strain tempering taken from Kalish and Cohen

The strain tempering process described by these authors is analogous to the experimental procedure in this work, where the re-tempering is replaced by ageing for long times at room temperature. This process should produce similar results so long as the ageing time is sufficient.

5.4 Transient Effects

As shown experimentally, the strain ageing of 300M steel at room temperature results in a significant increase in 0.2% strength upon re-loading. This strengthening manifests itself as a sharp "transient" increase in yield strength ranging from 30-100MPa depending on the amount of deformation and the ageing time. This increase in strength is said to be a transient as the rise in flow stress is temporary, and is followed by a gradual decrease to the stress level observed in an un-aged sample deformed monotonically to failure.

The maximum strengthening of 300M which was achieved in this work was just over 100MPa, measured via 0.2% offset stress after an initial deformation of 6%. Deformation beyond 6% in tension still likely resulted in strengthening in a diminished capacity, but this is difficult to determine due to necking. Long time-ageing also resulted in higher strength than the local maximum which was achieved after ageing for short and intermediate times, and a mechanism other than dislocation locking is presumed to be responsible. Since the maximum stress observed in this work occurred in a sample aged for relatively short times, the maximum strengthening could presumably be further increased by ageing for long times (600+ hours) at room temperature.

The transient strengthening effect demonstrated in this work can be described using the evolution of mobile and forest (immobile) dislocation densities via a dislocation model proposed by Kubin and Estrin [117]. The model computes the evolution of the mobile and forest densities as a function of strain based on the initial and saturation values of the dislocation densities. The coupled differential equations used to compute the evolving densities are shown in Equation 5 and Equation 6, where ρ_m and ρ_f represent the mobile dislocation densities respectively.

$$d\rho_m/d\epsilon = \frac{C_1}{b^2} - C_2\rho_m - \left(\frac{C_3}{b}\right)\rho_f{}^{1/2} \qquad [5]$$

$$d\rho_f/d\epsilon = C_2\rho_m + \left(\frac{C_3}{b}\right)\rho_f{}^{1/2} - C_4\rho_f \qquad [6]$$

The parameters in the above equations represent the multiplication of mobile dislocations (C_1), the trapping and annihilation of dislocations (C_2), immobilization due to interactions with forest dislocations (C_3), and dynamic recovery (C_4) [117]. These constants are calculated based on the initial and saturation densities, as well as their relative weight at saturation and the relaxation strain associated with the forest dislocation density [117]. The resulting deformation-induced dislocation density versus strain plots then resemble those shown in Figure 67.

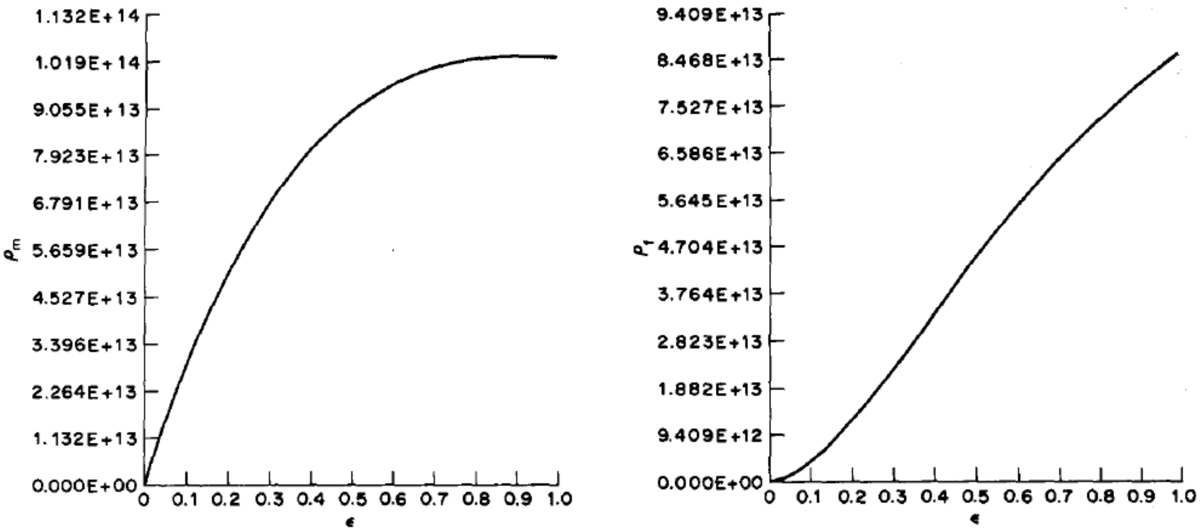

Figure 67 a,b: Evolution of the mobile (left) and forest (right) dislocation densities with strain as described by Kubin and Estrin **[117]**

These differential equations can be applied qualitatively to describe the strengthening observed in strain-aged samples in this work by recognizing that after ageing, the large number of mobile dislocations produced during deformation will become locked via solute atoms and become forest dislocations, thus increasing the forest dislocation density beyond the saturation value. The important parameter which then describes the transient increase in strength followed by recovery is the C_4 term which represents dynamic recovery in the forest dislocation evolution equation. If the forest dislocation density is suddenly increased beyond its saturation value through deformation and ageing, the system will reduce the number of forest dislocations via annihilation, reducing the stress required to move mobile dislocations through the material as it deforms.

The model described above was applied to this work in an effort to describe the transient strain ageing behaviour observed experimentally. The evolution of the mobile and forest dislocation densities was calculated using Equations 5 and 6 and a set of fixed initial and saturation conditions described by Kubin and Estrin [117].

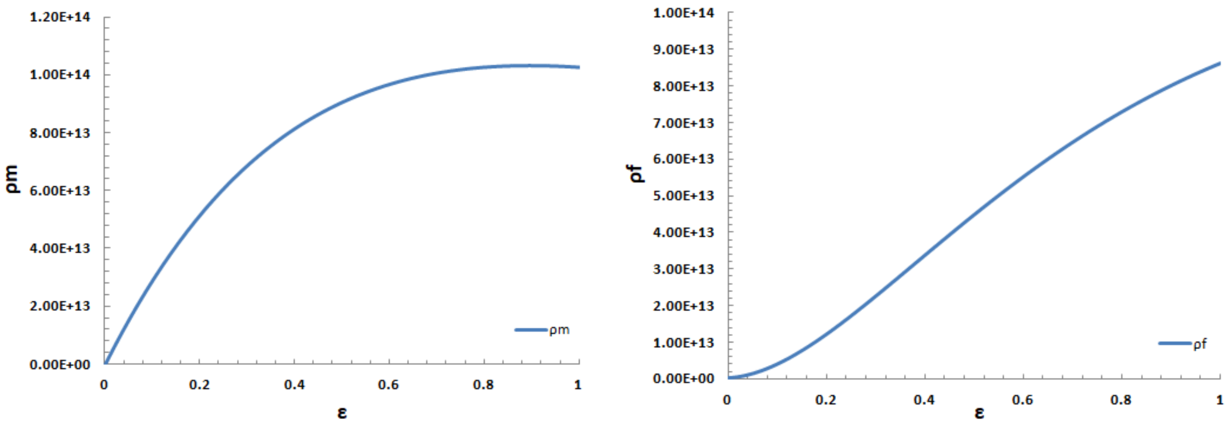

Figure 68 a,b: Duplicate calculations for the evolution of the mobile (left) and forest (right) dislocation densities in a given system as described by Kubin and Estrin

As shown above, the duplicate model created in this work was successfully able to model the evolution of the dislocation densities in a system described by fixed initial conditions. The next step in modeling the transient strengthening in this work was to simulate strain-ageing by artificially inducing "locking" in the system. This was done by decreasing the mobile dislocation density and increasing the forest density simultaneously at a given strain. The results of this simulation are shown below in Figure 69 a and b.

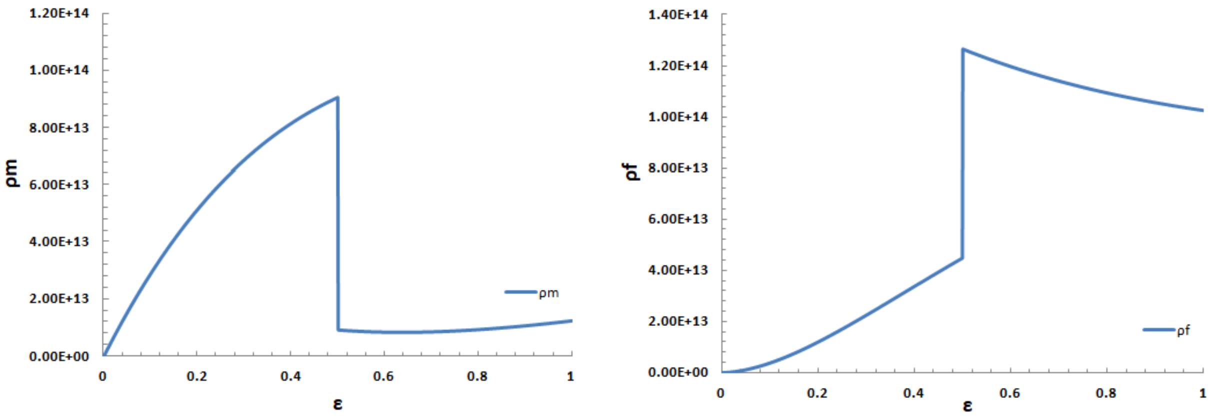

Figure 69a,b: Evolution of the mobile (left) and forest (right) dislocation densities before and after simulating 90% dislocation locking

As predicted, locking substantially increases the forest dislocation density which must attempt to restore itself to the saturation value via dislocation annihilation, and the mobile density continues to increase with strain as deformation resumes. After validating the effect of locking on the dislocation densities, the model was coupled with stress using an equation from work by Estrin [118] as shown below in Equation 7.

$$\sigma = \sigma_0 (\frac{\acute{\varepsilon}_p Y^{m/_2}}{\varphi X})^{1/_m} \qquad [7]$$

The expression developed by Estrin describes the evolution of stress as a function of the plastic strain rate $\acute{\varepsilon}_p$, fitting parameters m and φ, ratios of the dislocation densities X and Y, and σ_0, which is a product of the shear modulus (G), burgers vector (b), Taylor factor M, a constant α (typically about 0.15), and the initial forest density (ρ_{f0}) as shown in Equation 8. The parameter X is defined as the ratio of the current mobile density over the initial density, and Y represents the same ratio for the forest dislocations.

$$\sigma_0 = M\alpha Gb\sqrt{\rho_{f0}} \qquad [8]$$

.

Coupling the dislocation evolution equations with stress and adjusting the initial and saturation dislocation densities accordingly then allows for the modeling of the transient stress increase observed in 300M after ageing. A simulation of the increase in stress resulting from induced dislocation locking is available in Figure 70.

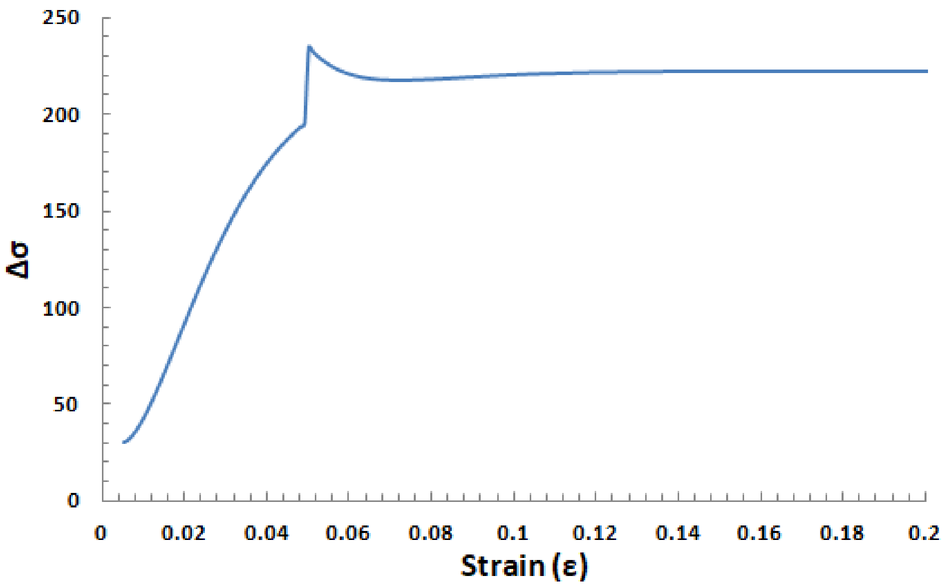

Figure 70: Modeling of the transient stress behaviour in an aged sample as a result of evolving dislocation densities

While the model is adequate in terms of re-producing the increase in stress produced by strain ageing, further work must be done in order to match the fraction of locked dislocations with magnitude of the increase. Currently, the model predicts significant increases in stress with only 5% locking of mobile dislocations. In order to accurately reproduce dislocation locking, the fitting parameters must be adjusted such that large increases in stress are produced by higher fractions of locked dislocations. Additionally, this simplified model does not consider the heterogeneous structure mentioned earlier, which would result in staggered dislocation "breakaway" from solute atmospheres due to variable yield stresses present in the material.

5.4.1 Effect of Ageing on Ductility

In an effort to quantify the effects of strain ageing on ductility, the reduction in area was calculated for each round specimen using low magnification SEM fracture images and ImageJ software. Most ageing treatments did not display a clear trend, and displayed an average of 40% reduction in area regardless of pre-strain or ageing time for samples aged up to 72 hours at room temperature. Tensile round samples tempered at temperatures exceeding 200°C however showed a slight decrease in reduction area with decreasing tempering temperature, which shows good agreement with experimental stress-strain results and the observations of other authors [110].

Samples aged at room temperature for very long times (650 hours) demonstrated the largest decrease in reduction of area of all samples tested in this work, and the reduction in area measurements for these samples are shown in Table 11. This is in good agreement with authors who have stated that strain-ageing results in decreased ductility.

Batch ID	Pre-strain	Ageing Time	Ageing Temperature	Reduction in Area
159340	1%	650 hours	25°C	27%
159340	1.5%	650 hours	25°C	27%
159340	2%	650 hours	25°C	26%
159340	2.5%	650 hours	25°C	17%

Table 11: Reduction in area measurements from selected round tensile specimens aged for long times

As shown above, this work demonstrates that strain-ageing reduces the ductility of 300M, but only in cases where samples were aged for very long times or re-tempered. The discrepancy between this work and others could be explained by the significant tempering process used for the 300M in this work, or variation in the reduction in area measurements. The fact that only tempered specimens or those aged for long times experienced any significant reduction in ductility could indicate that carbon segregation is at least partly responsible for the decrease in ductility. As such, additional work could clarify any potential segregation to microstructural features such as boundaries, or the dissolution and re-precipitation of carbides hinted at by Stephenson and Cohen [110] and described in detail by Kalish and Cohen [8].

5.4.2 Effects of Ageing on Strain Rate Sensitivity

One of the most interesting experimental observations noted in the course of this work was the apparent transition in strain rate sensitivity observed in samples after strain ageing at room temperature. While monotonic testing yielded negative strain rate sensitivity when tested at room temperature, samples that were strain aged at room temperature exhibited what appears to be clear positive strain rate sensitivity upon re-loading. Leslie and Sober noted a transition in lower carbon steels than the one used in this work, where the strain rate sensitivity of the material shifted from negative to positive after a critical strain rate, which they determined to be on the order of $0.01s^{-1}$. This transition did not occur in any tests performed in this work, and the mechanism responsible therefore cannot be responsible for the shift to apparent positive strain rate sensitivity.

The most surprising aspect of the apparent positive sensitivity observed in this work is that dynamic ageing effects persist during tests which seemingly show positive strain rate sensitivity. This is notable since negative strain rate sensitivity is generally held to be a manifestation of dynamic ageing [63] [115] [59]. It is possible that the strain rate sensitivity is indeed positive at low strain rates ($0.00133\text{-}0.0133s^{-1}$) after ageing, and reverts to negative sensitivity at rates approaching $0.133s^{-1}$. This transition would be difficult to observe using only the existing test data, since the negative sensitivity above $0.133s^{-1}$ could only be observed by testing at higher rates to determine if a drop in flow stress occurred. It is more likely, however, that the increases in stress and changes in the material induced by deformation and ageing are masking what is in fact still negative strain rate sensitivity after re-loading.

5.4.3 Effects of Applied Stress during Ageing

Throughout this work, samples were aged in the presence and the absence of applied loads. No significant differences were observed between the two loading conditions, as both experiments resulted in a strengthening of approximately 60MPa after ageing at room temperature for one hour. The similarity in strengthening after ageing was somewhat surprising, as the work of Wilson and Russell demonstrated that low carbon steel aged at room temperature developed a larger increase in yield stress when stressed during the ageing process [100]. The steel tested by Wilson and Russell was untempered however, so significant auto-tempering and segregation after deformation may explain the discrepancies between their results and this work. If the presence of an applied load increased the magnitude of strengthening it is possible that a more significant difference between loaded and unloaded ageing would be observed for 300M if the samples were aged for longer times, which would allow for greater solute segregation. This possibility is reinforced by the fact that Wilson and Russell observed a maximum in stress after ageing for over 160 hours [100], and the maximum increase in strength observed in this work also occurred after ageing for long times. It is also possible that an applied stress alters the short time kinetics of ageing as the results of Imanaka and Fujimoto suggest, in which case the ageing time of 1 hour used in this work would not have revealed an effect [104]. In this case, the effects of applied stress would be more apparent after shorter ageing times.

5.5 Failure Mechanisms and Fracture

5.5.1 Failure Analysis

Throughout this work, the fracture surfaces of tensile specimens of all sample geometries were catalogued and examined. All samples displayed significant evidence of ductility, including finely dimpled fracture surfaces and the average 40% reduction in area for round tensile specimens. All fracture surfaces were also characterized by significant topography that manifested as flat surfaces either above or recessed below the general fracture surface. These features also displayed fine dimples however, and do not represent evidence of brittle failure. Ageing for short to intermediate times of up to 72 hours did not result in any change in the ductility of the material, but ageing for long times (650 hours) and tempering resulted in the appearance of some apparently brittle facets, implying that strain-ageing reduces ductility.

Sample geometry also had an effect on the failure of 300M. Flat specimens exhibited a lower failure strain and slightly increased tendency to display mixed-mode facets when compared to rounds, both before and after ageing. Of all sample types, the notched specimens displayed the most evidence of a mixed fracture mode. The presence of facets in conjunction with dimples provides evidence that the state of stress induced in notched samples promotes a transition towards a brittle or quasi-brittle fracture. The nature of the induced brittle fracture appears to favor a transgranular mechanism over an intergranular fracture mode, based on the angle of the facets. Some facets and terraces appear at an angle to the fracture surface, however, and these could be due to cracks propagating along parallel packets or a portion of a prior austensite grain boundary.

Zok studied the deformation and fracture of ductile and brittle materials, and determined that the mechanism which governed ductile fracture in tempered 4340 was the nucleation of voids at carbide particles [90]. He also noted that this was significant because the failure of 4340 cannot be modeled in terms of the growth and coalescence of voids. The structure and composition of tempered 4340 is extremely similar to the 300M used in this work, and the failure mechanism described by Zok may explain the nature of the fracture observed in this work. If the transition carbides present in 300M are preferentially located at lath, grain and packet boundaries as TEM indicated earlier, void nucleation on these particles could explain the nature of the ductile fracture observed. This would be consistent with the fact that the size of the observed features is on the order of parallel packets, blocks, or a section of a prior austensite grain boundary in the microstructure (30-50µm). Evidence of void linkage appears to be prominent around the circumference of the terrace-like features as well as shown in Figure 71, which supports the failure mechanism of void nucleation at second phase particles.

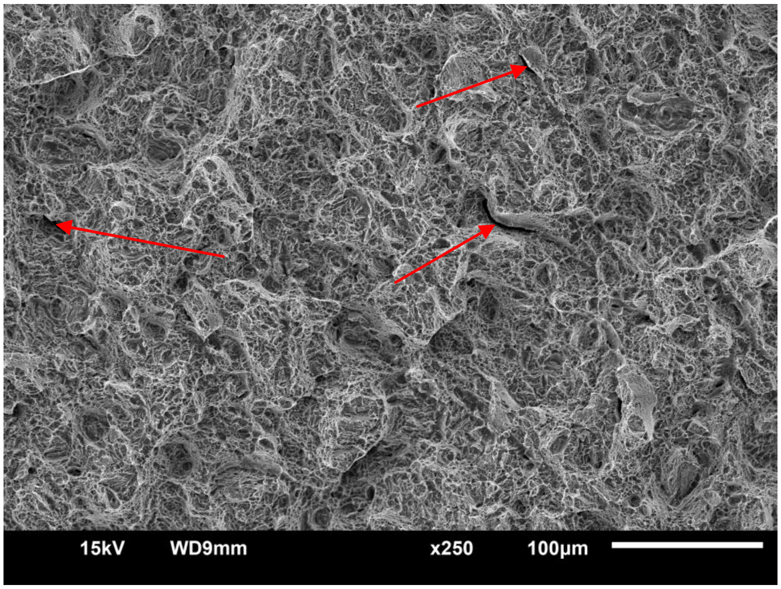

Figure 71: SEM fracture image for a sample deformed to 1% and aged at room temperature for 650 hours

Zok also observed delamination in certain samples, which he attributed to de-cohesion of prior austenite boundaries or fracture along inclusion stringers [90]. No delamination was observed for 300M, but this may be explained by a lack of cementite particles at grain boundaries and a much lower inclusion population as a result of the vacuum arc re-melting (VAR) treatment.

5.5.1 Inclusion Analysis

Brown and Embury demonstrated that large diameter inclusions and clusters caused a greater reduction in failure strain than small particles since the voids nucleated on a particle were more than twice as large as the particle itself [119]. Their work also postulated that failure strain depended strongly on the volume fraction of inclusions so long as the total volume fraction was less than 5% [119]. An expression for failure strain was developed as shown in Equation 9, where f is the volume fraction of inclusions, ε_n is the necking strain and ε_T is the failure strain.

$$\varepsilon_T = \ln\left(\sqrt{\frac{\pi}{2f}} - \sqrt{\frac{2}{3}} + \varepsilon_n\right)$$

Equation 1: Failure strain dependence on the volume fraction of inclusions as described by Brown and Embury

Another conclusion from the work by Brown and Embury was that the fracture toughness of a material was directly proportional to the failure strain, and thus the volume fraction and radius of inclusions [119]. Their work provides a convincing explanation for the reduced fracture strain and brittle behaviour observed in the tensile specimen that contained a vastly larger number of inclusions, as the larger number of particles allowed for greater nucleation and linkage of voids which caused failure earlier than expected. Work on nucleation of voids around inclusions and second phase particles has since continued and been improved by authors such as Thomason, but the simplified conclusions drawn by Brown and Embury remain valid [120].

Chapter 6 – Conclusions

6.1 Summary and Key Results

This work has furthered the understanding of the effect of strain-ageing on the mechanical properties and fracture of high strength steels. While the body of literature on such steels is extensive, this work has provided a broad perspective using modern tools to provide a general understanding of the deformation of martensite and how it can be modeled.

The existence of dynamic strain ageing in 300M at room temperature has been confirmed for a range of strain rates between 0.00133-0.266s^{-1} using digital image correlation techniques. The presence of negative strain rate sensitivity at room temperature was also observed, in good agreement with the presence of dynamic ageing.

The mechanical response of 300M to strain ageing has been comprehensively studied and summarized. The maximum increase in strength measured by 0.2% offset stress was over 100MPa, and occurred after 6% deformation in tension and ageing for several hours. It is estimated that this value could be increased further by ageing for very long times at room temperature. The mechanism of dislocation locking responsible for strengthening after ageing was examined, and the dependence of the increase in strength on time was explained using Cottrell-Louat segregation kinetics. The transient flow stress behaviour occurring upon re-loading after strain ageing has also been successfully modeled using the evolution of mobile and forest dislocation densities.

The effect of strain ageing on fracture in 300M was also examined, and the mechanism responsible for failure was hypothesized to be the nucleation of voids on second phase particles concentrated on lath, packet, and prior austenite grain boundaries. The influence of second phase particles and inclusions on fracture was also examined, and the brittle behaviour observed in certain material was found to be a result of a much larger density of inclusions.

6.2 Future Work

This work has revealed a number of topics that merit further investigation, which are outlined below:

1) The presence of dynamic ageing should be further investigated to determine the exact strain rate range in which dynamic effects can occur in 300M at room temperature. While the existence of dynamic ageing was confirmed in this work, the exact regions of temperature and strain rate where it is present should be identified.
2) The effect of deformation on dynamic ageing should also be investigated further, in order to determine if deformation affects the strain rate sensitivity of 300M or simply masks the negative rate sensitivity observed in this work.
3) While the segregation of carbon is strongly inferred in this work, investigation using atom probe tomography could provide insight into the mechanism responsible for the strengthening observed after long time ageing. The possibility of carbide dissolution as a result of deformation and ageing should also be examined and quantified.
4) The dislocation evolution model for the flow stress behaviour following deformation and ageing should be further refined so that the deformation of 300M can be simulated with relative accuracy.

Bibliography

[1] D. A. Porter, K. E. Easterling and Y. M. Sherif, Phase Transformations in Metals and Alloys, CRC Press, 2009.

[2] H. K. D. H. Bhadeshia, Worked Examples in the Geometry of Crystals, London: Institute of Metals, 1987.

[3] S. Morito, X. Huang, T. Furuhara, T. Maki and N. Hansen, "The morphology and crystallography of lath martensite in alloy steels," *Acta Materialia,* vol. 54, pp. 5323-5331, 2006.

[4] X. Huang, S. Morito, N. Hansen and T. Maki, "Ultrafine Structure and High Strength in Cold-Rolled Martensite," *Metallurgical and Materials Transactions A,* vol. 43A, pp. 3517-3531, 2012.

[5] L. Du, S. Yao, J. Hu, H. Lan, H. Xie and G. Wang, “Fabrication and Microstructural Control of Nano-structured Bulk Steels,” *Acta Metallurgica Sinica,* vol. 27, no. 3, pp. 508-520, 2014.

[6] G. Krauss and A. R. Marder, “Morphology of Martensite in Iron Alloys,” *Metallurgical Transactions,* vol. 2, p. 2357, 1971.

[7] H. S. Rawdon and S. Epstein, “Structure of Martensitic Carbon Steels and Changes in the Microstructure Which Occur Upon Tempering,” *Scientific Papers of The Bureau of Standards,* vol. 18, 1922.

[8] D. Kalish and M. Cohen, “Structural Changes and Strengthening in the Strain Tempering of Martensite,” *Materials Science and Engineering (ASM),* vol. 6, pp. 156-166, 1970.

[9] G. R. Speich and W. C. Leslie, “Tempering of Steel,” *Metallurgical Transactions,* vol. 3, pp. 1043-1054, 1972.

[10] C. C. Tasan, D. Ponge, D. Raabe and L. Morsdorf, “3D structural and atomic-scale analysis of lath martensite: Effect of the transformation sequence,” *Acta Materialia,* vol. 95, pp. 366-377, 2015.

[11] G. R. Speich, “Tempering of Low Carbon Martensite,” *Transactions of the Metallurgical Society of the AIME,* vol. 245, pp. 2553-2564, 1969.

[12] E. M. Roberts and D. Kalish, “On the Distribution of Carbon in Martensite,” *Metallurgical Transactions,* vol. 2, 1971.

[13] L. Chiang, G. D. W. Smith and S. J. Barnard, “The Segregation of Carbon Atoms to Dislocations in Low-carbon Martensites: Studies by Field Ion Microscopy and Atom Probe Microanalysis,” in *Speich Symposium Proceedings*, 1992.

[14] S. Allain, F. Danoix, M. Goune, K. Hoummada and D. Mandelinck, “Static and dynamical ageing processes at room temperature in a Fe25Ni0.4C virgin martensite: effect of C redistribution at the nanoscale,” *Philosophical Magazine Letters,* vol. 93, no. 2, 2013.

[15] B. Hutchinson, J. Hagstrom, O. Karlsson, D. Lindell, M. Tornberg, F. Lindberg and M. Thuvander, “Microstructures and hardness of as-quenched martensites (0.1-0.5%C),” *Acta Materialil,* vol. 59, pp. 5845-5858, 2011.

[16] B. P. J. Sandvik and C. M. Wayman, “Characteristics of Lath Martensite: Part I. Crystallographic and Substructural Features,” *Metallurgical Transactions A,* vol. 14A, pp. 809-822, 1983.

[17] K. Wakasa and C. M. Wayman, “The Morphology and Crystallography of Ferrous Lath Martensite. Studies of Fe 20% Ni 5%Mn II Transmission Electron Microscopy,” *Acta Metallurgica,* vol. 29, pp. 991-1011, 1981.

[18] R. L. Patterson and C. M. Wayman, “Crystallography and Growth of Partially-Twinned Martensite Plates in Fe-Ni Alloys,” *Acta Metallurgica,* vol. 14, pp. 347-369, 1966.

[19] S. Morito, J. Nishikawa and T. Maki, “Dislocation Density within Lath Martensite in Fe-C and Fe-Ni Alloys,” *ISIJ International ,* vol. 43, no. 9, pp. 1475-1477, 2003.

[20] T. Berecz, P. Jenei, A. Csore, J. Labar, J. Gubicza and P. J. Szabo, “Determination of dislocation density by electron backscatter diffraction and X-ray line profile analysis in ferrous lath martensite,” *Materials Characterization,* vol. 113, pp. 117-124, 2016.

[21] P. G. Winchell and M. Cohen, “The Strength of Martensite,” *Transactions of the American Society for Metals,* vol. 55, pp. 347-361, 1962.

[22] G. Badinier, "Effect of Carbon Segregation and Carbide Precipitation on the Mechanical Response of Martensite," University of British Columbia, 2012.

[23] S. Nagakura, Y. Hirotsu, M. Kusunoki, T. Suzuki and Y. Nakamura, “Crystallographic Study of the Tempering of Martensitic Carbon Steel by Electron Microscopy and Diffraction,” *Metallurgical Transactions A,* vol. 14A, pp. 1025-1031, 1983.

[24] M. J. Van Genderen, M. Isac, A. Bottger and E. J. Mittemeijer, “Aging and Tempering Behaviour of Iron-Nickel-Carbon and Iron-Carbon Martensite,” *Metallurgical and Materials Transactions A,* vol. 28A, pp. 545-561, 1997.

[25] O. N. C. Uwakweh, J. P. Bauer and J. M. R. Genin, “Mossbauer Study of the Distribution of Carbon interstitials in Iron Alloys and the Isochronal Kinetics of the Aging of Martensite: The Clustering-Ordering Synergy,” *Metallurgical Transactions A,* vol. 21A, pp. 589-602, 1990.

[26] F. Danoix, D. Julien, X. Sauvage and J. Copreaux, "Direct evidence of cementite dissolution in drawn pearlitic steels observed by tomographic atom probe," *Materials Science and Engineering: A,* vol. 250, pp. 8-13, 1998.

[27] K. H. Jack, "The iron-nitrogen system: the precipitation and the crystal structures of nitrogen austenite and nitrogen-martensite," *Proceedings of the Royal Society of London. Series A Mathematical and Physical Sciences,* vol. 208, pp. 210-215, 1951.

[28] Y. Hirotsu and S. Nagakura, "Crystal structure and morphology of the carbide precipitated from martensitic high carbon steel during the first stage of tempering," *Acta Metallurgica ,* vol. 20, pp. 6-45-655, 1972.

[29] C. Zhu, A. Cerezo and G. D. W. Smith, "Carbide characterization in low-temperature tempered steels," *Ultramicroscopy,* vol. 109, pp. 545-552, 2009.

[30] W. Leslie and R. Sober, "Strength of ferrite and of martensite as functions of composition, temperature, and strain rate," *Trans ASM,* vol. 60, no. 3, pp. 459-484, 1967.

[31] M. Sarikaya, A. K. Jhingan and G. Thomas, "Retained Austenite and Tempered Martensite Embrittlement in Medium Carbon Steels," *Metallurgical Transactions A,* vol. 14A, pp. 1121-1133, 1983.

[32] T. K. Ha, C. H. Lee and K. S. Kim, "Spheroidization Behaviour of Cementite in a High Carbon Steel," *Materials Science Forum,* Vols. 654-656, pp. 150-153, 2010.

[33] G. Y. Lai, W. E. Wood, R. A. Clark, V. F. Zackay and E. R. Parker, "The Effect of Austenitizing Temperature on the Microstructure and Mechancial Properties of As-Quenched 4340 Steel," *Metallurgical Transactions,* vol. 5, pp. 1663-1670, 1974.

[34] K. P. Datta, "Sharp Crack and Blunt Notch Toughness Behaviour of Quenched AISI 4340 Steel," *Materials Science and Engineering,* vol. 51, pp. 241-252, 1981.

[35] Y. Ohmori and I. Tamura, "Epsilon Carbide Precipitation during Tempering of Plain Carbon Martensite," *Metallurgical Transactions A,* vol. 23A, pp. 2737-2751, 1992.

[36] G. Krauss and J. P. Materkowski, "Tempered Martensite Embrittlement in SAE 4340 Steel," *Metallurgical Transactions A,* vol. 10A, pp. 1643-1651, 1979.

[37] G. Balestrino and M. Cavallini, "Mossbauer Spectroscopy Study of Retained Austenite Tempering in 4340 Steels," *Scripta Metallurgica,* vol. 17, pp. 1407-1412, 1983.

[38] J. Vajda, J. J. Hauser and C. Wells, "Effect of Silicon on Transverse Properties and on Retained Austensite Content of High Strength Steels," *Transactions of the ASM,* vol. 49, pp. 518-549, 1956.

[39] C. H. Shih, B. L. Averbach and M. Cohen, “Some Effects of Silicon on the Mechanical Properties of High Strength Steels,” *Transactions of the ASM,* vol. 48, pp. 87-118, 1956.

[40] R. M. Horn and R. O. Ritchie, “Mechanisms of Tempered Martensite Embrittlement in Low Alloy Steels,” *Metallurgical Transactions A,* vol. 9A, 1978.

[41] J. L. Youngblood and M. Raghavan, “Microstructure and Mechanical Properties of Quenched and Tempered 300M Steel,” NASA (Technical Paper 1288), Springfield, 1978.

[42] F. Liu, X. Lin, M. Song, H. Yang, K. Song, P. Guo and W. Huang, “Effect of tempering temperature on microstructure and mechanical properties of laser solid formed 300M steel,” *Journal of Alloys and Compounds,* vol. 689, pp. 225-232, 2016.

[43] R. Padmanabhan and W. E. Wood, “Microstructural Analysis of a Multistage Heat-treated Ultrahigh Strength Low Alloy Steel,” *Materials Science and Engineering ,* vol. 66, pp. 125-143, 1984.

[44] G. Krauss, *ISIJ International,* vol. 35, p. 349, 1995.

[45] N. Bandyopadhyay and C. J. McMahon Jr, “The Micro-Mechanisms of Tempered Martensite Embrittlement in 4340-Type Steels,” *Metallurgical Transactions A,* vol. 14A, pp. 1313-1325, 1983.

[46] G. Krauss, "Martensite in steel: strength and structure," *Materials Science and Engineering,* Vols. A273-275, pp. 40-57, 1999.

[47] J. Christian, “The strength of martensite,” *Strengthening Methods in Crystals,* pp. 261-330, 1971.

[48] R. F. Vynhal and S. V. Radcliffe, “Effects of Pressure on the Structure of Iron-Carbon Martensites,” *Acta Metallurgica ,* vol. 15, pp. 1475-1488, 1968.

[49] J.-Y. Kang, S. C. Kim, J.-O. Oh, H. N. Han, K. H. Oh and H.-C. Lee, “Martensite in interstitial-free steel obtained by ultra-high pressure,” *Acta Materialia,* vol. 66, pp. 45-48, 2012.

[50] G. Speich and H. Warlimont, “Yield strength and transformation substructure of low-carbon martensite,” *Iron and Steel Insititute of Japan,* vol. 206 (Part 4), pp. 385-392, 1968.

[51] G. Badinier, C. W. Sinclair, S. Allain, F. Danoix and M. Goune, “Microstructure and Mechanical Behaviour of Ferrous Martensite,” Elsevier, Vancouver, 2016.

[52] J. M. Chilton and P. M. Kelly, “The Strength of Ferrous Martensite,” *Acta Metallurgica,* vol. 16, pp. 637-656, 1968.

[53] A. Shibata, T. Nagoshi, M. Sone, S. Morito and Y. Higo, “Evaluation of the block boundary and sub-

block boundary strengths of ferrous lath martensite using a micro-bending test," *Materials Science and Engineering A,* vol. 527, pp. 7538-7544, 2010.

[54] K. Zhu, O. Bouaziz, C. Oberbillig and M. Huang, "An approach to define the effective lath size controlling yield strength of bainite," *Materials Science and Engineering A,* vol. 527, pp. 6614-6619, 2010.

[55] A. H. Cottrell, "Effect of Solute Atoms on the Behaviour of Dislocations," in *Report of the Conference on Strength of Solids*, Bristol, 1947.

[56] R. A. Mulford and U. F. Kocks, "New Observations on the Mechanisms of Dynamic Strain Aging and of Jerky Flow," *Acta Metallurgica,* vol. 27, pp. 1125-1134, 1979.

[57] P. Van Liempt and J. Sietsma, "A Revised Criterion for the Portevin-Le Chatelier Effect Based on the Strain-Rate Sensitivity of the Work-Hardening Rate," *Metallurgical and Materials Transactions A,* vol. 42A, pp. 4008-4014, 2011.

[58] K. Tanaka and J. W. Spretnak, "An Analysis of Plastic Instability in Pure Shear in High Strength AISI 4340 Steel," *Metallurgical Transactions,* vol. 4, pp. 443-454, 1973.

[59] A. Benallal, T. Borvik, A. Clausen and O. Hopperstad, "Dynamic Strain Aging, Negative Strain-Rate Sensitivity and Related Instabilities," *Technische Mechanik,* vol. 23, pp. 160-166, 2003.

[60] W. S. Owen and M. J. Roberts, "Dynamic Aging Effects in Ferrous Martensite," *Trans. JIM,* Vols. 9, Supplement, 1968.

[61] M. J. Roberts and W. S. Owen, "Unstable Flow in Martensite and Ferrite," *Metallurgical Transactions,* vol. 1, pp. 3203-3213, 1970.

[62] H. Mimura and K. Aoki, "Strain Rate Dependence of the Flow Stress in Martensite," *Trans. JIM ,* Vols. 9, Supplement, 1968.

[63] P. Rodriguez, "Serrated plastic flow," *Bulletin of Materials Science,* vol. 6, no. 4, pp. 653-663, 1984.

[64] W. D. Callister Jr and D. G. Rethwisch, Materials Science and Engineering: An Introduction, Hoboken: John Wiley and Sons, Inc, 2009.

[65] G. Speich and P. Swann, "Yield strength and transformation substructure of quenched iron-nickel alloys," *Iron and Steel Institute of Japan,* vol. 203 (Part 5), pp. 480-485, 1965.

[66] S. Radcliffe and M. Schatz, "Effects of high pressure on strength and structure of martensites," *Nature,* vol. 200, pp. 161-163, 1963.

[67] A. G. Vasil'eva and D. A. Prokoshkin, “Mechanism of Strain Aging of Martensite,” *Metallovedenie i Termicheskaya Obrabotka Metallov,* vol. 1, pp. 2-10, 1971.

[68] A. J. Ardell, “Precipitation Hardening,” *Metallurgical Transactions A,* vol. 16A, pp. 2132-2165, 1985.

[69] L. Malik and J. A. Lund, “A Study of Strengthening Mechanisms in Tempered Martensite From a Medium Carbon Steel,” *Metallurgical Transactions,* vol. 3, pp. 1403-1406, 1972.

[70] A. H. Cottrell and B. A. Bilby, "Dislocation theory of yielding and strain ageing of iron," *Proceedings of the Physical Society of London A,* vol. 62, pp. 49-62, 1949.

[71] A. W. Cochardt, G. Schoek and H. Wiedersich, “Interaction between dislocations and interstitial atoms in body-centered-cubic materials,” *Acta Metallurgica,* vol. 3, pp. 533-537, 1955.

[72] M. K. Miller, P. A. Beaven, S. S. Brenner and G. D. W. Smith, “An Atom Probe Study of the Aging of Iron-Nickel-Carbon Martensite,” *Metallurgical Transactions A,* vol. 14A, pp. 1021-1024, 1983.

[73] J. Wilde, A. Cerezo and G. D. Smith, “Three-Dimensional Atomic-Scale Mapping of a Cottrell Atmosphere Around a Dislocation in Iron,” *Scripta Materialia,* vol. 43, no. 1, pp. 39-48, 2000.

[74] G. B. Olson and M. Cohen, “Early Stages of Aging and Tempering of Ferrous Martensites,” *Metallurigical Transactions A,* vol. 14A, pp. 1057-1065, 1983.

[75] A. M. Sherman, G. T. Eldis and M. Cohen, “The Aging and Tempering of Iron-Nickel-Carbon Martensites,” *Metallurgical Transactions A,* vol. 14A, pp. 995-1005, 1983.

[76] L. Cheng, N. M. van der Pers, A. Bottger, T. H. de Keijser and E. J. Mittemeijer, “Lattice Changes of Iron-Carbon Martensite on Aging at Room Temperature,” *Metallurgical Transactions A,* vol. 22A, p. 1957, 1991-1967.

[77] C. L. Magee and R. G. Davies, “The Structure, Deformation and Strength of Ferrous Martensites,” *Acta Metallurgica,* vol. 19, pp. 345-354, 1971.

[78] B. Kim and a. et, “The influence of silicon in tempered martensite: Understanding the microstructure-properties relationship in 0.5-0.6 wt%C steels,” *Acta Materialia,* vol. 68, pp. 169-178, 2014.

[79] J. E. Wittig and G. Frommeyer, “Deformation and Fracture Behaviour of Rapidly Solidified and Annealed Iron-Silicon Alloys,” *Metallurgical and Materials Transactions A,* vol. 39A, pp. 252-265, 2008.

[80] T. Swarr and G. Krauss, “The Effect of Structure on the Deformation of As-Quenched and

Tempered Martensite in an Fe-0.2 Pct C Alloy," *Metallurgical Transactions A,* vol. 7A, pp. 41-48, 1976.

[81] H. Muir, B. Averbach and M. Cohen, "The Elastic Limit and Yield Behaviour of Hardened Steels," *Transactions of the ASM,* vol. 47, pp. 380-407, 1955.

[82] M. Zaccone and G. Krauss, "Elastic limits and microplastic response in ultrahigh strength carbon steels," *Metallurgical and Materials Transactions A,* vol. 20, no. 1, pp. 188-191, 1989.

[83] B. Hutchinson, D. Lindell and M. Barnett, "Yielding Behaviour of Martensite in Steel," *ISIJ International,* vol. 55, no. 5, pp. 1114-1122, 2015.

[84] H. Snyder, "Effect of quenching and tempering on residual stresses in manganese oil hardening tool steel," American Society for Metals, Cleveland, OH, United States, 1952.

[85] K. A. Taylor, G. B. Olson, M. Cohen and J. B. Vander Sande, "Carbide Precipitation during Stage I Tempering of Fe-Ni-C Martensites," *Metallurgical Transactions A,* vol. 20A, pp. 2749-2765, 1989.

[86] S. Allain, A. Arlazarov, O. Bouaziz, A. Hazzote and M. Goune, "Characterization and Modeling of Manganese Effect on Strength and Strain Hardening of Martensitic Carbon Steels," *ISIJ Intern.,* vol. 53, no. 6, pp. 1076-1080, 2013.

[87] M. Saeglitz and G. Krauss, "Deformation, Fracture, and Mechanical Properties of Low-Temperature-Tempered Martensite in SAE 43xx Steels," *Metallurgical and Materials Transactions A,* vol. 28A, pp. 377-387, 1997.

[88] Y. A. Roy and R. Narasimhan, "Constraint effects on ductile fracture processes near a notch tip under mixed-mode loading," *Engineering Fracture Mechanics,* vol. 62, pp. 511-534, 1999.

[89] B. Nyhus, M. L. Polanco and O. Orjasaether, "SENT Specimens and Alternatives to SENB Specimens for Fracture Mechanics Testing of Pipelines," in *22nd International Conference on Offshore Mechanics and Arctic Engineering*, 2003.

[90] F. Zok, "The Influence of Hydrostatic Pressure on Fracture," Hamilton, ON, 1988.

[91] J. R. Rice and D. M. Tracey, "On the ductile enlargement of voids in triaxial stress fields," *J. Mech. Phys. Solids,* vol. 17, pp. 201-217, 1969.

[92] Y. Bai and T. Wierzbicki, "A new model of metal plasticity and fracture with pressure and load dependence," *International Journal of Plasticity,* vol. 24, pp. 1071-1096, 2008.

[93] P. W. Bridgman, "Studies in Large Plastic Flow and Fracture: With Special Emphasis on the Effects of Hydrostatic Pressure," *Science,* vol. 115, p. 424, 1952.

[94] Y. Bao and T. Wierzbicki, “On fracture locus in the equivalent strain and stress triaxiality space,” *International Journal of Mechanical Sciences,* vol. 46, pp. 81-98, 2004.

[95] D. V. Wilson, “Effects of Plastic Deformation on Carbide Precipitation in Steel,” *Acta Metallurgica,* vol. 5, pp. 293-302, 1957.

[96] M. Cohen, “Strengthening Mechanisms in Steel,” *Trans. JIM,* vol. 9, p. Supplement, 1968.

[97] D. Kalish and M. Cohen, “Structural Changes and Strengthening in the Strain Tempering of Martensite,” *Materials Science and Engineering,* vol. 6, pp. 156-166, 1970.

[98] C. N. Sastry, K. H. Khan and W. E. Wood, “Mechanical Stability of Retained Austenite in Quenched and Tempered AISI 4340 Steel,” *Metallurgical Transactions A,* vol. 13A, pp. 676-680, 1982.

[99] H. W. Paxton and C. C. Busby, “Strain Aging of AISI 4340,” *Transactions of the AIME,* pp. 788-789, 1956.

[100] D. V. Wilson and B. Russell, “Stress Induced Ordering and Strain-Ageing in Low Carbon Steels,” *Acta Metallurgica,* vol. 7, pp. 628-631, 1959.

[101] K. F. Starodubov and A. N. Kasilov, “Increase in the Strength of Steel with Strain Aging of Martensite,” *Metallovedenie i Termicheskaya Orabotka Metalov,* vol. 1, pp. 58-60, 1974.

[102] K. Momma, H. Suto, N. Uehara and Y. Kubomura, “Strength and Structure of Ausformed and Cold Worked Low Carbon Alloy Martensitic Steels,” *Trans. JIM,* Vols. 9, supplement, 1968.

[103] Total Materia, "Strain Ageing of Steel: Part One," 2 2013. [Online]. Available: http://www.totalmateria.com/page.aspx?ID=CheckArticle&site=kts&NM=392. [Accessed 10 8 2017].

[104] T. Imanaka and K. Fujimoto, “The Mechanism of Strain Age-Hardening in Low Carbon Steels,” *Trans. JIM,* Vols. 9, supplement, 1968.

[105] P. Haasen and A. Kelly, "A Yield Phenomenon in Face-Centered Cubic Single Crystals," *Acta Metallurgica ,* vol. 5, pp. 192-199, 1957.

[106] R. A. Elliot, E. Orowan, T. Udoguchi and A. S. Argon, “Absence of yield points in iron on strain reversal after aging, and the Bauschinger overshoot,” *Mechanics of Materials ,* vol. 36, pp. 1143-1153, 2004.

[107] W. G. Johnston, “Yield Points and Delay Times in Single Crystals,” *Journal of Applied Physics,* vol. 33, no. 9, pp. 2716-2730, 1962.

[108] "Dislocation Velocities, Dislocation Densities, and Plastic Flow in Lithium Fluoride Crystals," *Journal of Applied Physics,* vol. 30, no. 2, 1959.

[109] G. Krauss, “Deformation and Fracture in Martensitic Carbon Steels Tempered at Low Temperatures,” *Metallurigcal and Materials Transactions B,* vol. 32B, pp. 205-221, 2001.

[110] R. T. Stephenson and M. Cohen, "The Effect of Prestraining and Retempering on AISI Type 4340," *Transactions of the ASM,* vol. 54, pp. 72-83, 1961.

[111] N. McCormick and J. Lord, "Digital Image Correlation," *Materials Today,* vol. 13, no. 12, pp. 52-54, 2010.

[112] S. Yoneyama and G. Murasawa, "Digital Image Correlation," Encyclopedia of Life Support Systems.

[113] Y. J. M. Brechet, "Microstructure evolution and interface migration," *Solid State Phenomena,* vol. 56, pp. 51-66.

[114] Q. Lai, C. W. Sinclair and W. J. Poole, "The Anisotropic Kinetics of Strain Aging in a Martensitic Steel," *CMQ in press.*

[115] N. Louat, "On the Theory of the Portevin-Le Chatelier Effect," *Scripta Metallurgica,* vol. 15, no. 11, pp. 1167-1170, 1981.

[116] B. A. MacDonald, "Strain-Tempering of Iron-Carbon Martensites, PhD Thesis," MIT, 1964.

[117] L. P. Kubin and Y. Estrin, "Evolution of Dislocation Densities and the Critical Conditions for the Portevin-Le Chatelier Effect," *Acta Metallurgica et Materialia,* vol. 38, no. 5, pp. 670-708, 1990.

[118] Y. Estrin, "Dislocation-Density-Related Constitutive Modelling," in *Unified Constitutive Laws of Plastic Deformation*, Academic Press, 1996, pp. 69-106.

[119] L. M. Brown and J. D. Embury, "The Initiation and Growth of Voids at Second Phase Particles," 1973.

[120] P. F. Thomason, "Ductile fracture and the stability of incompressibility in the presence of microvoids," *Acta Metallurgica,* vol. 29, pp. 763-777.